## Title

Self-Similar Imploding Solutions of the Compressible Euler Equations with a Far Field Cutoff



## ISBN

9798190926446

## Author

Luong, Jack Quoc-Viet

## Publication Date

2026-09-10

Peer reviewed|Thesis/dissertation

UNIVERSITY OF CALIFORNIA
Los Angeles

# Self-Similar Imploding Solutions of the Compressible Euler Equations with a Far Field Cutoff

A dissertation submitted in partial satisfaction
of the requirements for the degree
Doctor of Philosophy in Mathematics

by

Jack Quoc-Viet Luong

2026

ABSTRACT OF THE DISSERTATION

Self-Similar Imploding Solutions
of the Compressible Euler Equations
with a Far Field Cutoff

by

Jack Quoc-Viet Luong
Doctor of Philosophy in Mathematics
University of California, Los Angeles, 2026
Professor Andrea L. Bertozzi, Chair

We study the problem of finite time singularities in the isentropic compressible Euler equations in with radial symmetry. We focus on implosions, where a flow directed towards the origin experiences finite time blowup in density. Smooth and self-similar imploding solutions to the isentropic, compressible Euler equations with radial symmetry, inspired by the work of Guderley, have garnered recent mathematical interest. However, these smooth imploding solutions are shown to be numerically unstable and difficult to compute in practice. On the other hand, the imploding solution of Kidder has a closed form solution and is numerically computable. But, it is unbounded in the far field. We consider the Kidder implosion with a continuous constant density cutoff, referred to as the *cutoff implosion* solution, in this work.

From studying the characteristics, we predict an expanding wave to emerge from the cutoff position. The expanding wave has its boundary described by the characteristics, which depend on the local speed of sound. The behavior of the cutoff implosion solution dramatically changes from one dimension to higher dimensions. In one dimension, a non-centered rarefaction emerges from the cutoff and suppresses the implosion. In higher dimensions, the expanding wave is not a classical rarefaction. However, the expanding wave still swallows

up the inner Kidder solution and the implosion still occurs. This composite blowup has an asymptotic self-similar form that has an interpretation in terms of Guderley-type self-similarity structure. Consistent with prior rigorous results for these equations, the blowup does not involve mass concentration and exhibits a critical $L^p$ space for the concentration of the density, depending on the dimension of space.

The theoretical predictions made are supported by direct numerical simulations of the compressible Euler equations. The Lagrangian leapfrog numerical scheme is used to perform these computations. This scheme is chosen in particular to avoid numerical diffusion. In higher dimensions, adaptive mesh refinement is employed to resolve the implosion with high fidelity.

The dissertation of Jack Quoc-Viet Luong is approved.

Luminita Vesa

Marcus Roper

Chris Anderson

Andrea L. Bertozzi, Committee Chair

University of California, Los Angeles

2026

*To my late father*

# Table of Contents

# List of Figures

# List of Tables

# ACKNOWLEDGMENTS

I am extremely grateful to my mentor, Andrea Bertozzi, for her support and mentorship throughout my graduate studies at UCLA. Her expertise was vital in contributing to my growth as a researcher. Not only that, I developed my own taste in research problems as well as an overarching philosophy on how to conduct research in physical applied mathematics through her guidance. I have greatly enjoyed our conversations throughout the years and learned many things scientific, career-wise, and about life in general.

I thank the members of my committee, who have also shaped my educational journey during my graduate studies. I thank Chris Anderson for introducing me to numerical methods for scientific problems and how enriching they can be when coupled with an underlying understanding of the physical model to be simulated. I thank Marcus Roper for introducing me to the study of ordinary and partial differential equations and the rich insights they can offer when studying phenomenons, such as fluid mechanics, modeled by them. I thank Luminita Vese for introducing me to the framework of finite element and variational methods and her support beyond course material. I also am incredibly grateful for her willing to step onto the committee on short notice. Although no longer able to serve on the committee, I thank Stan Osher for his brilliant insights to numerical methods in hyperbolic partial differential equations, as well as his incredible sense of humor.

The bulk of this thesis work is done in collaboration with Los Alamos National Laboratory, where I have spent the final summers of my graduate study. I have enjoyed the intellectual and scientific culture immensely as a student researcher at Los Alamos, and the experiences I had there have greatly influenced my research perspective. I thank my mentors at Los Alamos. I thank Roy Baty for his mentorship and expertise in physical phenomena and guiding me on how to synthesize physical understanding with mathematical insight. I thank Scott Ramsey for his mentorship in how to conduct myself as a researcher, as well as fascinating conversations on the topics discussed in this thesis and their broader implications. I thank Richard Bowers for introducing me to the Lagrangian leapfrog numerical scheme heavily used in this thesis. Richard also pushed me to use physical intuition as a

tool to reason through problems, which made me a better scientist.

There are many people who I have met during my time at UCLA I would like to thank. I thank Sarah Burnett for her help and experimental knowledge in studying particle laden flow on an incline and Shiba Biswal for her help in studying control theory applied to partial differential equations. I thank Yim Neang, Sanim Rishan, Pedro Lizaro, Kealan Schuster, and Rigo Resendiz for their administrative support. Many of my fellow classmates made the graduate journey more bearable and enjoyable. Thank you to Hong Kiat Tan, Zerrin Vural, and Christina Tran for their camaraderie in studying for coursework and qualifying exams. Thank you to Evan Davis and Yifan Gu for enlightening and enjoyable discussions about applied mathematics.

I am incredibly grateful to the Mathematics department at California State University, Fresno. Their support and encouragement introduced me the world of deeper mathematics and the phenomenal experience I had studying mathematics at Fresno State ultimately encouraged me to pursue graduate studies in the field. There are far too many wonderful professors to list, but thank you to Tamás Forgács, Khang Tran, Carmen Caprau, Oscar Vega, Doreen De Leon, Katherine Kelm, Maria Nogin, Adnan Sabuwala, Marat Markin, Stefaan Delcroix, along many others.

Parts of this thesis are adapted, with permission, from [LRB27] in Chapters 2.5 and 3 and parts of Chapters 6. The work of [LRB27] was done with Scott Ramsey, Andrea Bertozzi, and Roy Baty. Chapters 4, 5 and parts of Chapters 2.5 and 6 are adapted from work in preparation done with Reed Spitzer, Andrea Bertozzi, Scott Ramsey, and Roy Baty. I thank Reed Spitzer for his work in forming the region of influence argument and his work in studying the dynamical system arising from self-similarity.

I am grateful to the US Department of Energy and Los Alamos National Laboratory for supporting this work through the US Department of Energy (Contract No. 89233218CN000001) and Los Alamos National Lab award CW93449 C5677. I also thank the Office of Naval Research for supporting this work through ONR grant N00014-23-1-2565.

I thank my family for their unconditional love and support: my mother for raising me

and encouraging me to succeed academically and my sister for her incredible wit and being a source of levity.

I thank select members of the Socal DDR community for their friendship and helping make Los Angeles my home for the past five years. I will cherish the memories shared together deep in my heart.

# VITA

| | |
|---|---|
| 2017 | B.S. in Pure Mathematics, B.S. in Mechanical Engineering, California State University, Fresno |
| 2023 | M.A. in Mathematics, University of California, Los Angeles |
| 2023 - 2026 | Graduate Student Researcher at Los Alamos National Laboratory |

# PUBLICATIONS

Jack Luong, Scott D. Ramsey, Andrea L. Bertozzi, Roy Baty. "Self-similar imploding solutions of the 1D compressible Euler equations with a far field cutoff." *Discrete and Continuous Dynamical Systems*, 2027, 58: 197-221. doi: 10.3934/dcds.2026141

Jack Luong, Reed Spitzer, Scott D. Ramsey, Andrea L. Bertozzi, Roy Baty. "Finite time implosions of the compressible Euler equations with a finite far-field cutoff" *In Preparation*

# CHAPTER 1

# Introduction

Hyperbolic conservation laws are well known for *finite time blowup* - the phenomenon where the solutions of hyperbolic conservation laws lose regularity in finite time. This normally takes the form of a *shock*, as the gradient of solution variables becomes discontinuous. However, solutions to hyperbolic conservation laws may also blowup in finite time in the solution variables themselves. One such example are *implosions* in fluid dynamics, where a flow directed towards the origin collapses into itself. Implosions occur in processes such as cavitation [Hun60], sonoluminescence [BHL02], gas cloud accretion of galaxies [Woo76], star formation [Hun69], and inertial confinement fusion (ICF) [Kid74]. There has also been great recent interest in the mathematics community on constructing implosions for gas dynamics, see [JT20, MRR22a, MRR22b, BCG25, SWW25, CGS25, CSV26].

This work considers the explicit construction, analysis, and computation of continuous implosion solutions to the isentropic, compressible Euler equations with radial symmetry. Our solutions are formed by modifying the implosion solution of [Kid74] with a continuous cutoff in the far field. Properties of the *cutoff implosion* solutions are derived. The cutoff implosion solutions are numerically computed using the Lagrangian leapfrog method introduced by [NR50] and adaptive mesh refinement in higher dimensions. The resulting numerical simulations corroborate our theoretical predictions.

This thesis is organized as follows. Chapter 2 introduces the compressible Euler equa-

tions in generality. Simplifying assumptions and their physical interpretation are discussed, resulting in the isentropic, compressible Euler equations with radial symmetry studied for the remainder of the thesis. Another perspective on the isentropic, compressible Euler equations - potential flow - is introduced and used to understand implosions. The *linear velocity solution*, also referred to as the *Kidder solution*, is introduced as well. The linear velocity solutions are a class of fluid mechanics solutions originally developed by [Sed59] and used by [Kid74] to construct an explicit imploding solution for compressible gas dynamics. A generalized version of the linear velocity solution for generic dimension and adiabatic constant is derived. The initial densities of these solutions are continuously cutoff and studied in Chapter 3 and 4.

Chapter 3 studies the 1D case, in which the cutoff suppresses the Kidder solution, preventing an implosion. A rarefaction emerges from the cutoff point and can be expressed analytically, thereby giving a complete closed form to the cutoff implosion solution up until shock formation. The subsequent shock problem and solution is derived. The cutoff implosion problem in 1D is numerically simulated. We find excellent agreement between the numerical and predicted solution. Additionally, the self-similar structure of the analytical solution is also shown in the computed solution.

On the other hand, the constant cutoff does not suppress the implosion of the Kidder solution in higher dimensions. Chapter 4 begins by deriving the region of influence originating from the cutoff point. The resulting ordinary differential equation (ODE) has a closed form solution and is employed to derive the region of influence along with the density and velocity at the inner ring of the region of influence. Predicting the cutoff implosion solution should approach a self-similar limit close to implosion time, a similarity variable is defined based on the inner radius of the region of influence is defined. The resulting ODE system for the self-similar profiles is derived in non-autonomous and autonomous form. Numerical solutions to the ODE systems are computed and the corresponding phase portraits are analyzed. After the implosion of the cutoff implosion solution has been established, questions about mass concentration and density blowup in $L^p_{\text{loc}}$ are raised and answered. The chapter concludes by displaying the results of numerical simulations of the cutoff implosion solution in higher

dimensions. The numerical results support the theoretical predictions made previously in the chapter.

The numerical method used in both 1D and higher dimension simulations is described in Chapter 5. The implementation of the Lagrangian leapfrog numerical scheme and adaptive mesh refinement (for higher dimension simulations) is written out. Chapter 6 discusses the uniqueness of the cutoff implosion solution by the method of Weak-Strong Uniqueness. In 1D, Weak-Strong Uniqueness is applied directly to conclude the cutoff implosion solution is the unique weak solution from the initial data. However, the method does not generalize to higher dimensions nicely. Instead, Weak-Strong Uniqueness is applied heuristically to suggest the uniqueness of the cutoff implosion solution. We finish with concluding remarks and potential future avenues of study in Chapter 7.

# CHAPTER 2

# Background on the Compressible Euler Equations

## 2.1 Compressible Euler Equations

We first state the partial differential equations (PDEs) of the compressible Euler equations in $\mathbb{R}^d$ in generality. Assume the fluid is compressible but inviscid and does not conduct heat. The conservation of mass is

$$\rho_t + \nabla \cdot (\rho \vec{v}) = 0. \tag{2.1}$$

where $\rho$ is the fluid density and $\vec{v}$ is the fluid velocity. The conservation of momentum for a smooth flow is

$$\rho(\vec{v}_t + \vec{v} \cdot \nabla \vec{v}) = -\nabla P \tag{2.2}$$

where $P$ is the pressure. The conservation of internal energy energy is

$$e_t + \vec{v} \cdot \nabla e = \frac{-P}{\rho} \nabla \cdot \vec{v} \tag{2.3}$$

where $e$ is the specific internal energy. The total energy $E$, is also conserved and given by

$$E = \frac{1}{2}\rho |\vec{v}|^2 + \rho e. \tag{2.4}$$

In order to fully describe the motion and thermodynamics of the compressible fluid, we

specify equation of state that describes how the pressure depends on the other state variables. In general, the pressure $P$ is a function of the density and specific internal energy.

A physically relevant quantity is the local speed of sound, defined by

$$c = \sqrt{\frac{\partial P}{\partial \rho}}. \tag{2.5}$$

## 2.2 Further Assumptions

We are interested in studying the compressible Euler equations under further assumptions and discuss each assumption and their physical interpretations in this section.

### 2.2.1 Irrotational

We assume the fluid is irrotational, that is, $\nabla \times \vec{v} = 0$. This implies the vorticity $\omega = \nabla \times \vec{v} = 0$ throughout the fluid and its evolution. Since the velocity field has no curl, we may define a scalar function $\phi$ such that $\nabla \phi = \vec{v}$. By integrating the conservation of momentum equation (2.2) in space, we obtain the equation for the potential:

$$\phi_t + \frac{1}{2}||\nabla \phi||^2 = -\int \frac{\nabla p}{\rho} \tag{2.6}$$

recalling $\nabla \phi \cdot \nabla \phi = ||\nabla \phi||^2$. This equation is also known as Bernoulli's equation for unsteady, compressible, potential flow.

Equation (2.6) may be interpreted as a Hamilton-Jacobi equation that describes the movement of the level sets of $\phi$ with velocity $\frac{1}{2}\nabla \phi$. The level sets move in the direction of their gradient. So, they move in the direction that locally increases the value of $\phi$ the most. As the level sets move around, their values change at a rate of the local density, described by right hand side of (2.6).

### 2.2.2 Isentropic

The entropy of a fluid in a state of thermodynamic equilibrium is given as

$$s_2 - s_1 = C_V \ln \frac{p_2}{\rho_2^\gamma} - C_V \ln \frac{p_1}{\rho_1^\gamma} \tag{2.7}$$

where $C_V$ and $C_p$ are the heat capacities of a fluid at constant volume and constant pressure respectively, and $\gamma = \frac{C_p}{C_V}$ is the specific heat capacity ratio or adiabatic index/exponent. The heat capacities $C_V$ and $C_P$ indicate how much heat is required to increase the temperature of a material held at constant volume and pressure respectively. The entropy of a fluid is physically defined as comparisons between two states denoted with subscripts 1 and 2. In practice we can take the reference state as the initial state and set $S_1 = C_V \ln \frac{p_1}{\rho_1^\gamma}$, defining the entropy as

$$s = C_V \ln \frac{p}{\rho^\gamma}. \tag{2.8}$$

For *smooth* flows, the entropy along characteristics is conserved and thus satisfies the equation

$$s_t + \vec{v} \cdot \nabla s = 0. \tag{2.9}$$

If the entropy is constant in the domain at the initial time, then the entropy remains constant throughout the domain for all later times as long as the flow remains smooth. In the applied mathematics literature, such a flow is called *isentropic*. A flow loses its smoothness when shocks occur, in which case the entropy is no longer conserved along characteristics. Instead, the entropy on a characteristic increases when the characteristic crosses the shock. For our study of potential flow, we consider smooth flows up until the time shocks emerge so our isentropic assumption is valid.

The speed of sound in an isentropic flow is

$$c^2 = \left.\frac{\partial p}{\partial \rho}\right|_s. \tag{2.10}$$

This allows us to rewrite the source term of Equation (2.6) as

$$\begin{aligned} -\int \frac{\nabla p}{\rho} &= -\int \frac{1}{\rho}\frac{\partial p}{\partial \rho}\nabla\rho \\ &= -\int \frac{c^2}{\rho}\nabla\rho. \end{aligned}$$

### 2.2.3 Vorticity and Crocco's Theorem

Although we assume in potential flow that the velocity has no initial vorticity, it is not clear vorticity cannot develop later in time. In the isentropic case, this cannot occur due to Crocco's theorem:

**Theorem 2.2.1** (Crocco's theorem [Cro37])**.** *For a smooth, compressible flow governed by the Euler equations, the state variables on a streamline satisfy*

$$\frac{\partial \vec{v}}{\partial t} + \nabla(\frac{\vec{v}\cdot\vec{v}}{2} + h) = \vec{v}\times\omega + T\nabla s \tag{2.11}$$

*where $h$ is the specific enthalpy, defined as $h = e + \frac{P}{\rho}$.*

Since the velocity satisfies the conservation of momentum (2.2), the development of vorticity is given by

$$\vec{v}\times\omega = -T\nabla s. \tag{2.12}$$

So, if the entropy is constant throughout the fluid initially, then for a smooth flow $\nabla s = 0$ for all future times as well, and so $\omega$ must remain 0.

### 2.2.4 Ideal Gas

Now, we define the equation of state that describes how the pressure depends on the state variables. We assume we are working with an ideal gas which has the equation of state

$$P = (\gamma - 1)\rho e. \tag{2.13}$$

The pressure may be written in terms of the state variables density and entropy instead; in which case, the equation of state is

$$P = \rho^{\gamma} e^{s/C_v}. \tag{2.14}$$

However, if the entropy is constant in the domain initially and the flow remains smooth, then $s$ is constant throughout space and time, and $e^{s/C_v}$ is also a constant. This yields the isentropic pressure relationship

$$P = C\rho^{\gamma} \tag{2.15}$$

where $C = e^{s/C_v} > 0$ is a constant. Thus, under these assumptions, we have successfully eliminated the dependence of Equations (2.2) and Equations (2.6) on thermodynamic variables as the pressure as depends only on density. We can further simplify the source term of Equation (2.6) now that we have the closed form expression for pressure in terms of density, obtaining

$$-\int \frac{\nabla p}{\rho} = -C\frac{\gamma}{\gamma-1}\rho^{\gamma-1}.$$

Thus, the full set of equations describing the compressible, inviscid, irrotational, isentropic Euler equations or *potential flow* with an ideal equation of state for pressure, is

$$\rho_t + \nabla \cdot (\rho \nabla \phi) = 0 \tag{2.16}$$

and

$$\phi_t + \frac{1}{2}|\nabla\phi|^2 = -C\frac{\gamma}{\gamma-1}\rho^{\gamma-1} \tag{2.17}$$

where equation (2.16) is obtained by writing (2.1) in terms of the potential and (2.17) is obtained by simplifying (2.6) with the above expression for pressure. Note assuming an isentropic flow along with an ideal gas allows us to fully close (2.16) and (2.17) without having to specify an equation tracking the energy evolution. We refer to the non-isentropic case as the *Full Euler* equations to differentiate from the *isentropic Euler* case considered in this work. For potential flow, the speed of sound reduces to

$$c = \sqrt{C\gamma}\rho^{\frac{\gamma-1}{2}}. \tag{2.18}$$

### 2.2.5 Radial Symmetry

Finally, we assume radial symmetry in the compressible Euler equations, which is a subset of irrotational flows. Equations (2.1) and (2.2) become

$$\frac{\partial \ln\rho}{\partial t} + v\frac{\partial \ln\rho}{\partial r} + \frac{\partial v}{\partial r} + \frac{nv}{r} = 0, \tag{2.19}$$

$$\frac{\partial v}{\partial t} + v\frac{\partial v}{\partial r} + C\gamma\rho^{\gamma-2}\frac{\partial \rho}{\partial r} = 0. \tag{2.20}$$

where the spatial index $n = d - 1$ where $d$ is the dimension. Important values of $n$ are 0 for planar geometry, 1 for cylindrical geometry, and 2 for spherical geometry. In this work, we consider imploding solutions to (2.19) and (2.20).

## 2.3 Background on Shocks and Implosions

We review the relevant background on finite time blowup for the compressible Euler equations - both Full and isentropic - in this subsection. First, we discuss classical results for shocks and general finite time blowup. Afterwards, the imploding solution of Guderley [Gud42] and subsequent work is summarized. Most relevant to this current work are the linear velocity solutions introduced by Sedov [Sed59] and applied in [Kid74].

### 2.3.1 Shocks

The majority of the literature around finite time blowup centers around shocks, and we mention here a few key results. In his seminal work, Lax [Lax64] used Riemann invariants to show shock formation for small initial data of $2 \times 2$ systems of hyperbolic conservation laws. Shock formation is described in more detail for the 1D isentropic Euler equations in [Leb92]. For large data, the authors of [CPZ17] extend the use of Riemann invariants for the isentropic Euler equations and attribute singularity formation to initial compression.

For higher dimensions, Sideris [Sid85] gave the first result on finite time blowup for the Full and isentropic Euler equations. Assuming far field initial conditions, Sideris studied the evolution of an energy to determine finite time blowup. However, this argument cannot reveal whether the blowup is a shock or an implosion. The author of [Yin04] proved this finite time singularity can be a shock under the additional assumption of spherical symmetry. For potential flow, [Yue17] builds on the work of [Sid85] by giving a blowup criteria which does not depend on the initial density. With the assumption of potential flow, Christodoulou and Miao [CM14] proved initial compression leads to shocks for potential flow with constant far field initial data. In a similar setting of constant far field initial density, Chen and Wang [CW22] show global existence of weak solutions to the isentropic Euler equations with spherical symmetry in higher dimensions by vanishing viscosity. They note the global existence is given in $L^p_{\text{loc}}$, which permits the existence of implosion solutions. Furthermore, they show these solutions cannot concentrate mass. If instead a vanishing far field density is considered, [Suz13] shows potential flow with $L^1$ density and energy must have singularity

formation in finite time.

In the case of 2D specifically, Buckmaster et al. [BSV22] construct smooth initial data to the isentropic Euler equations that form a shock driven by vorticity. The authors also show smooth solutions with azimuthal symmetry forms a pre-shock and cusp [BDS22].

### 2.3.2 Implosions - Guderley

While implosions are not as well-studied as shocks, there is still a significant amount of literature related to implosions, especially in recent years. The first study of implosions for compressible fluids is the work of Guderley [Gud42]. By casting the problem into a system of ODEs in the self-similar variables, Guderley uses the corresponding phase portrait to construct the imploding solution. The solution features a shock converging to the origin which drives blowup in velocity and pressure, although density remains bounded. Guderley's approach has formed the backbone for substantial subsequent work in imploding solutions. For recent and direct continuations to Guderley's work, Jang et al. [JLS25] give a rigorous construction of the Guderley solution while Cialdea et al. [CSV25] show the Guderley solution can arise from non-shocked initial data. In an attempt to generalize the Guderley solution for non-ideal gases, the authors of [BRB17] discuss the necessary form of the adiabatic bulk modulus to produce self-similar solutions to the Guderley problem.

Since the Guderley solution begins with shocked initial data, it remains unclear whether an implosion can arise from continuous or even smooth initial data. Many recent results have answered this question for the isentropic Euler equations with self-similar solutions. Jennsen and Tsikkou [JT20] construct self-similar, radially symmetric, and continuous imploding solutions with strictly positive pressure, in contrast to the vanishing pressure of the Guderley solutions. Their solution has unbounded energy, but they argue they can form a finite mass and energy variant of the solution with a finite speed of propagation argument.

Smoothness of imploding solutions was further developed in the celebrated work of Merle et al. [MRR22a]. In their work, they rigorously show the existence of smooth imploding self-similar solutions to the isentropic, radially symmetric Euler equations with careful phase

portrait analysis. These solutions are used to construct imploding solutions to the Navier-Stokes equations in [MRR22b]. Merle et al. show this could be done for almost every choice of heat capacity ratio $\gamma > 1$. However, one of the omitted $\gamma$ is $\gamma = \frac{5}{3}$ which has physical significance as it is the heat capacity ratio of a monatomic gas. Buckmaster et al. improve the result by expanding the range of permissible $\gamma$ to all $\gamma > 1$. They use a computer-assisted proof to handle the special case of $\gamma = \frac{5}{3}$ and rigorously handle error bounds with interval arithmetic. Shao et al. [SWW25] give a construction specifically designed to handle the degenerate case of $\gamma = \frac{5}{3}$ for the purpose of constructing smooth implosions for the Navier-Stokes equations.

Implosions in a non-radial symmetric setting is discussed in [CGS25] where the authors show the radially symmetric implosion profiles of Merle et al. are stable for certain non-radial perturbations. A different approach of generalizing the result of Merle et al. is to "lift" the radially symmetric imploding profile to the axisymmetric Euler equations in higher dimensions leading to vorticity blowup, done for 2D in [CCS24] and 3D in [Che25]. In the setting of the Full Euler equations with spherical symmetry, Chen et al. construct smooth self-similar implosions [CSV26]. These implosions are fully non-isentropic as the density reaches infinity in finite time while the pressure may remain finite. The shocked solution emerging from the implosion is considered in their follow-up work [CCS26].

Despite the recent developments on implosions for the isentropic Euler equations, some practical concerns remain. The imploding solutions presented in [MRR22a] and built upon in further work are not explicitly constructed. Moreover, attempts to understand these simulations computationally are stymied by the inherent instability of the solutions [Bia21]. Given the instability of these profiles, it is unclear how to interpret them physically and numerically.

### 2.3.3 Implosions - Kidder

Given these drawbacks, we instead turn to the class of self-similar imploding solutions inspired by the work of Sedov [Sed59] and popularized in the seminal work of Kidder [Kid74].

Sedov considered solutions to the Euler equations where the velocity is affine in the spatial variable. An example of an imploding solution to the Full Euler equations satisfying this principle with a Gaussian density profile can be found in [Hor69]. A characterization of imploding profiles with the ansatz of Sedov is described in [LW06]. A recent survey of these solutions is discussed in [Jen26].

Motivated by the application of ICF [Kid74], Kidder constructs an explicit self-similar imploding solution to the 3D, isentropic, radially symmetric Euler equations with $\gamma = \frac{5}{3}$ by considering homogeneous isentropic compression - compression where each volume element is compressed identically. We note the concept of homogeneous compression is expressed mathematically as the linear velocity ansatz attributed to Sedov. Kidder expands his solution to the compression of a hollow shell in [Kid76]. Both solutions have formed the cornerstone of self-similar imploding solutions in ICF modeling (see [AV04]). The Guderley and Kidder solutions can be considered under the same viewpoint, along with other classic self-similar solutions to the compressible Euler equations, by studying the underlying self-similar dynamical system as done in [VS82].

The downside of Kidder's solution, and more generally solutions with linear velocity, is the unboundedness of initial data or solution as the flow progresses. In the case of Kidder's solution, the initial density is shown to be radially unbounded. Moreover, the density approaches infinity almost everywhere in the domain. For solutions with linear velocity in general, the linear growth in velocity implies unbounded velocity in the far field. Both of these properties render the physical implementation of Kidder's solution impractical.

Despite concerns about unboundedness, the explicit form and apparent numerical stability of the Kidder solution are desirable enough to try to find workarounds. One attempt at ameliorating the nonphysical initial data is to continuously cutoff the initial density by a constant at some finite spatial point. The nonphysical, radially unbounded initial density is replaced with the milder condition of enforcing a constant density outside a finite ball. This setting is similar to that of [Sid85] and [CM14].

## 2.4 A Potential Flow Perspective on Implosions

We note in general implosions are difficult to come by in the isentropic Euler equations. The prototypical example of an implosion is the unbounded accumulation of mass at a point as exhibited via the imploding Gaussian solution for the full Euler equations demonstrated in [Hor69] and [Ram11]. However, for the isentropic Euler equations, local maxima in density are discouraged from imploding. We can understand this by studying the potential flow equations (2.16) and (2.17) in one dimension.

Suppose we have a stationary implosion at a local maximum for density located at $x^*$ in finite time. So, there exists a time $t^*$ and implosion time $T$ such that $\lim_{t\to T}\rho(x^*,t)=\infty$ with $u(x^*,t)=0$ and $\rho(x^*,t)$ is a local maximum for $\rho$ for all times $t^*\le t\le T$. Studying equation (2.16) at $x^*$ for times $t\ge t^*$ yields

$$\rho_t(x^*,t)=-\rho(x^*,t)\phi_{xx}(x^*,t), \tag{2.21}$$

with solution

$$\rho(x^*,t)=\rho(x^*,t^*)\exp\int_{t^*}^{t}-\phi_{xx}(x^*,s)ds. \tag{2.22}$$

Now, in potential flow, gas flows in the direction of maxima of the potential. So, $\phi$ also has a local maximum at $x^*$ and the Laplacian of $\phi$ at $x^*$ is negative. Thus, the density can only continue to grow as long as $\phi_{xx}$ remains negative. For the density to implode in finite time, $\phi_{xx}$ itself must blow up in finite time.

The dynamics of $\phi_{xx}$ are obtained by taking the Laplacian of (2.17). We have

$$\partial_t\phi_{xx}+\phi_{xx}^2+\phi_x\phi_{xxx}=-C\frac{\gamma}{\gamma-1}\partial_{xx}\rho^{\gamma-1}$$

which evaluated at $x^*$ is

$$\partial_t\phi_{xx}(x^*,t)=-\phi_{xx}^2(x^*,t)-C\frac{\gamma}{\gamma-1}\partial_{xx}(\rho(x^*,t)^{\gamma-1}). \tag{2.23}$$

Examining the terms of the right hand side of equation (2.23), the Laplacian of $(\rho(x^*,t)^{\gamma-1})$ remains negative since $x^*$ is a local maximum of $\rho$ and $\gamma>1$. In contrast, we know the term $-\phi_{xx}^2(x^*,t)$ causes finite time blowup left on its own. The growth of $\phi_{xx}(x^*,t)$ is

balanced by the competing factors of $-\phi_{xx}^2(x^*,t)$ and $-\partial_{xx}(\rho(x^*,t)^{\gamma-1})$ with the pressure term counterbalancing the imploding term.

For this reason, in practice it is difficult to observe these types of implosions. Consider the following initial data in 1D for equations (2.19) and (2.20):

$$\rho(x,0) = \epsilon \exp(-x^2), \quad v(x,0) = \arctan(-x) \tag{2.24}$$

where $\epsilon$ is a positive scalar. As $\epsilon \to 0$, equations (2.19) and (2.20) approach Burgers' equation. From numerical simulations, these solutions do not implode. For a short period of time, density starts to accumulate at the origin as desired, but after some critical time, the density starts to expand outwards from the origin and eventually collides with the density being directed towards the origin - forming a shock. Figure 2.1 shows the normalized density and velocity profiles for various choices of $\epsilon$ right before shock time. For any $\epsilon > 0$, two shocks form away at the origin representing the contact between gas expanding away from the origin and gas being compressed towards the origin. The shock position decreases as $\epsilon$ decreases. In general, as $\epsilon$ approaches 0, the solutions approach the solutions of Burgers' equation. Additionally, the velocity profile begins to resemble the solution for Burgers' equation while the density approaches a delta function.

With the Gaussian density and arctangent velocity profile, we tried to induce an implosion by accumulating gas at the origin. The density has a local maximum at this accumulation point. However, the gas fails to implode, and a shock forms, indicating the gas expands away from the origin. Physically, the pressure of the gas at the origin grows until it grows too large and expands outwards. An example of this for $\epsilon = 1$ can be seen in Figure 2.2. The non-implosion occurs regardless of how much mass we start with. This numerical experiment, as well as the preceding discussion, showcases how constructing a simple imploding solution is difficult and naive approaches will not work. As far as the authors are aware, the literature studying this effect is lacking although numerical simulations are straightforward to perform. The challenges of forming an implosion via accumulation of mass at a stationary point along with the reported numerical instabilities by Biasi for the smooth imploding solutions of Merle et al. and Buckmaster et al. encourage further investigation of imploding solutions, such as

the solution of Kidder. Kidder's solution avoids these pitfalls as the solution features an attractive global minimum in density rather than an attractive maximum.

Unfortunately, a major drawback to Kidder's solution is the solution is radially unbounded. Although it has an explicit form, the radial unboundedness makes it nonphysical. Since Kidder's imploding solution still has many desirable properties such as its explicit form and apparent numerical stability, we seek to modify the solution to make it more physically feasible while also preserving its desirable features. We propose continuously cutting off the initial data by a constant past some point in the domain. By doing so, we replace the nonphysical property of radial unboundedness with the milder physical requirement of enforcing constant density past a certain spatial point. Note this is the same setting studied in [Sid85] and [CM14]. The effect the constant cutoff has on the solution is governed by a finite speed of propagation. It is unclear how the cutoff will affect the imploding solution as it approaches implosion time and whether the implosion will still occur. This work seeks to answer such questions.

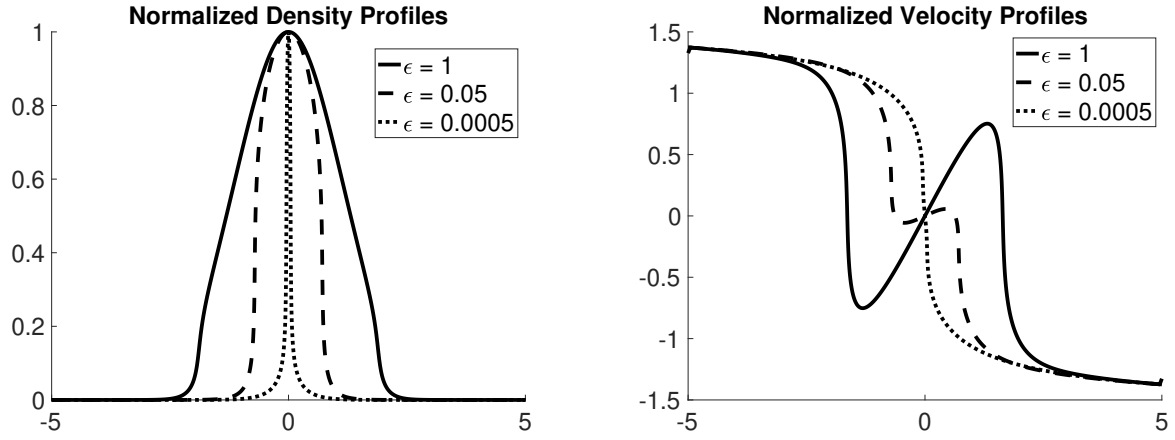


(a) Density

(b) Velocity

Figure 2.1: Normalized density and velocity for various choices of $\epsilon$ in initial data (2.24) at their respective shock times.

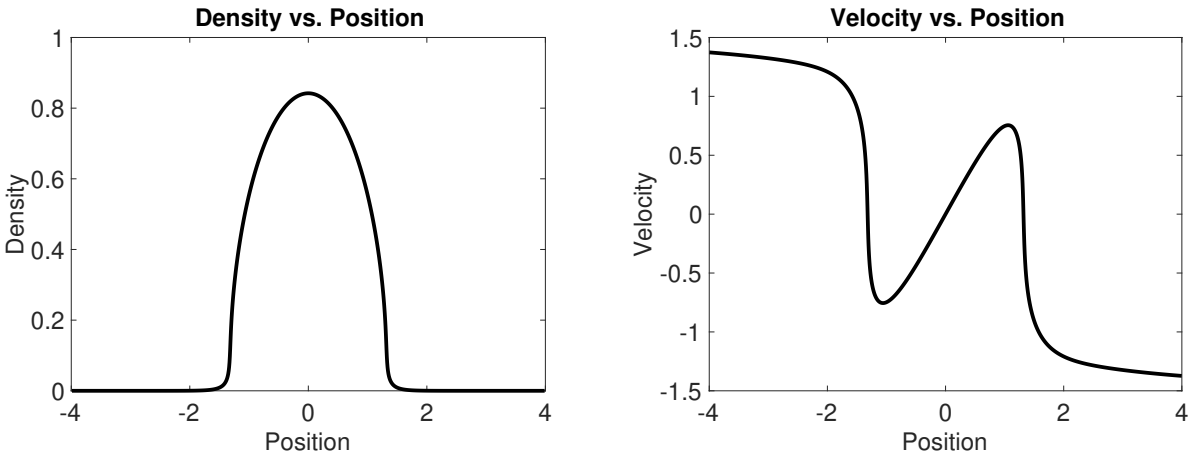


(a) Density (b) Velocity

Figure 2.2: Density and Velocity past the shock time for $\epsilon = 1$. After the shock occurs, the gas expands outwards into the compressing gas in the far field.

## 2.5 Construction of the Linear Velocity Solution

A part of this chapter is adapted from [LRB27]. Here we review the linear velocity solutions in [GRB20] and [Ram11] with the concept of linear velocity solutions originating from [Sed59]. In doing so, we obtain the homogeneous isentropic implosion solution introduced in [Kid74]. When deriving the linear velocity solutions, we will deviate from the derivation done in [GRB20] and [Ram11], giving a new derivation of this solution.

We introduce the *linear velocity ansatz*:

$$v(r,t) = r\frac{\dot{R}(t)}{R(t)} \tag{2.25}$$

where $R(t)$ is the *scale radius*, to be determined. This velocity is a homogeneous compression as introduced in [Kid74]. The scale radius represents the Lagrangian position of a particle [Sed59].

We assume that $\rho$ depends on the similarity variable $\xi = r/R(t)$. Conservation of mass (in all of space if $\rho$ is globally integrable or locally inside a ball of radius $MR(t)$ otherwise) implies that $\rho$ has the general form

$$\rho(\xi,t) = \frac{\mathcal{R}(\xi)}{R^{n+1}(t)} \tag{2.26}$$

where $\mathcal{R}(\xi)$ is an arbitrary function of $\xi$. Since we consider the isentropic case, the pressure is $C\rho^\gamma$. We substitute the ansatzes (2.25) and (2.26) into (2.20) to obtain

$$R(t)^{1-\eta}\ddot{R}(t) = -\frac{C\gamma}{\xi}\mathcal{R}'(\xi)\mathcal{R}(\xi)^{\gamma-2} \tag{2.27}$$

where $\eta = (n+1)(1-\gamma)$. By separation of variables, both sides of equation (2.27) evaluate to constants. The left hand side of equation (2.27) implies

$$\frac{d}{dt}\left(\ddot{R}R^{1-\eta}\right) = 0. \tag{2.28}$$

We select the initial conditions $R(0) = R_0$, $\dot{R}(0) = 0$, and $\ddot{R}(0) = \ddot{R}_0$ and justify them as follows. The first initial condition $R(0) = R_0$ simply states Lagrangian particles all must start at some position. The third initial condition $\ddot{R}(0) = \ddot{R}_0$ indicates whether the particles initially accelerate or decelerate. The second initial condition $\dot{R}(0) = 0$ determines whether the particles are at rest at time $t = 0$.

We are interested in the case when $\ddot{R}_0 < 0$, corresponding to the imploding case. Without loss of generality, we pick $R_0 = 1$ and $\ddot{R}_0 = -1$. With the selection of initial conditions for $R(t)$, both sides of equation (2.27) equate to $-1$. The right hand side of equation (2.27) simplifies to

$$\xi = C\gamma\mathcal{R}^{\gamma-2}\frac{d\mathcal{R}}{d\xi} \tag{2.29}$$

which has solution

$$\mathcal{R}(\xi) = \left(B\frac{\gamma-1}{\gamma}\left(\frac{1}{2}\xi^2 + \rho_0\right)\right)^{\frac{1}{\gamma-1}} \tag{2.30}$$

where $B = \frac{1}{C}$. With both $R(t)$ and $\mathcal{R}(\xi)$ defined, the density and pressure are

$$\rho(r,t) = \frac{\left(B\frac{\gamma-1}{\gamma}\left(\frac{1}{2}\frac{r^2}{R(t)^2} + \rho_0\right)\right)^{\frac{1}{\gamma-1}}}{R(t)^{n+1}} \tag{2.31}$$

and

$$P(r,t) = C\frac{\left(B\frac{\gamma-1}{\gamma}\left(\frac{1}{2}\frac{r^2}{R(t)^2} + \rho_0\right)\right)^{\frac{\gamma}{\gamma-1}}}{R(t)^{\gamma(n+1)}} \tag{2.32}$$

respectively. This is a generalization to arbitrary heat capacity ratio and dimension of the isentropic implosion solutions described in [GRB20] and [Ram11].

In the special case when $\eta = -2$, we can solve equation (2.28) analytically to obtain

$$R(t) = \left(1 - t^2\right)^{\frac{1}{2}} \tag{2.33}$$

leading to the velocity profile

$$v(r,t) = -\frac{rt}{1-t^2}. \tag{2.34}$$

Note the case of $\eta = -2$ represents a monatomic gas in various dimensions. One example is $n = 2$ and $\gamma = \frac{5}{3}$: a monatomic gas in three dimensions. The case of $\eta = -2$ also corresponds to Kidder's solution. Once $R(t)$ is known, the Lagrangian position of particles $X(t, x_0)$, where $x_0$ represents the initial location of particles, is given by

$$X(t, x_0) = x_0\sqrt{1-t^2}. \tag{2.35}$$

So, all particles arrive at the origin by time $t = 1$.

We can understand how the implosion of solutions (2.31) and (2.32) occur through the potential when $R(t)$ is given by (2.33). The potential $\phi(r,t)$ in this case is

$$\phi(r,t) = -\frac{r^2 t}{2(1-t^2)}. \tag{2.36}$$

When $t > 0$, the potential at the origin remains zero while at all other points in the domain, the potential decreases over time. This means the origin is the local (and also global) maximum of the potential. In contrast, the origin is the local (and also global) minimum of the density. From equation (2.17), the density will tend towards local maxima of the potential, which is located at the origin. However, the potential decreases in value everywhere in the domain except for the origin, which means the origin will always remain the global maximum of the potential. So, the flow will always be directed towards the origin up until implosion time. We emphasize how the origin remains attractive for all time because it continues to be the global minimum in density. This is in contrast to the scenario described for attractive local maxima where the pressure term discourages unbounded accumulation.

Regardless of $n$ and $\gamma$, these solutions have the property that $\rho(r,t)$ goes to $\infty$ as $r \to \infty$. This feature is physically undesirable. Although the initial velocity is zero, the initial density is radially unbounded. Phrased differently, the total initial energy of these solutions is radially unbounded because the initial potential energy is radially unbounded. This motivates

our investigation of "cutoff" solutions - solutions emanating from the Kidder solution initial data on some finite spatial interval $[0, r^*]$ and is continuously connected to a constant outside the interval.

For the remainder of this work, we will consider the imploding solution in the specific case of

$$\gamma = \frac{n+3}{n+1} \tag{2.37}$$

in order to ensure $\eta = -2$, leading to the convenient formula for $R(t)$ prescribed in equation (2.33). We also set the constants $\rho_0, B, C$ described previously as $\rho_0 = 0$ and $B = C = 1$. This gives initial data

$$\rho(r,0) = \left(\frac{1}{n+3}\right)^{(n+1)/2} r^{n+1}, \quad v(r,0) = 0, \tag{2.38}$$

with solution

$$\rho(r,t) = \left(\frac{1}{n+3}\right)^{(n+1)/2} \left(\frac{r}{1-t^2}\right)^{n+1}, \quad v(r,t) = -\frac{rt}{1-t^2}, \tag{2.39}$$

assuming $C = 1$ and the density at the origin vanishes. We refer to this initial data and corresponding solution as the *Kidder* initial data and solution. The Kidder solution achieves implosion at time $t = 1$ with all particles arriving at the origin simultaneously. However, the initially density, and subsequently total initial energy, is radially unbounded.

For $n > 0$, the Kidder solution begins subsonic and becomes supersonic everywhere except the origin before imploding. By comparing the velocity to the speed of sound using (2.39), the Kidder solution remains subsonic up until time

$$t^* = \left(\frac{1}{n+1}\right)^{1/2} \tag{2.40}$$

and remains supersonic afterwards. The time the solution becomes supersonic occurs is strictly less than 1 for all $n > 0$. For $n = 0$, the Kidder solution remains subsonic for all time up to $t = 1$.

# CHAPTER 3

# Cutoff Implosion in One Dimension

This chapter is adapted from [LRB27]. In this chapter, we construct the solution to the imploding initial data with a constant cutoff in one dimension described in the previous chapter and discuss some pertinent features of the solution.

## 3.1 Introduction of Cutoff Initial Data

In one dimension $\rho$ is symmetric and $v$ is anti-symmetric about the origin $x = 0$. As previously mentioned, we are interested in seeing whether the imploding behavior persists even when the initial data in $\rho$ is cut off in the far field. Continuously cutting off the initial data of (2.38) with a constant yields

$$\rho(x,0) = \begin{cases} \frac{\sqrt{3}}{3}x & \text{for } |x| \leq x^* \\ \frac{\sqrt{3}}{3}x^* & \text{for } |x| \geq x^* \end{cases}, \quad v(x,0) = 0 \tag{3.1}$$

where $x^*$ is a positive real number. We call this problem and the corresponding solution the *cutoff implosion* problem and solution. This initial density is equal to the Kidder initial density for $|x| \leq x^*$ and is a constant outside of this interval. As the solution evolves, new behavior emanates from the cutoff point $x^*$. We analyze this behavior in the following section.

## 3.2 Hyperbolic Conservation Law Theory

We first review the necessary hyperbolic conservation law theory as described in [Lax73], [Lev90], and [Eva22] to construct our cutoff implosion solution. We rewrite the one dimensional isentropic Euler equations ((2.19) and (2.20)) in conservation form as

$$\rho_t + (\rho v)_x = 0, \quad v_t + \frac{1}{2}(3\rho^2 + v^2)_x = 0 \tag{3.2}$$

defining the fluxes as

$$f(\rho, v) = v\rho, \quad g(\rho, v) = \frac{1}{2}\left(3\rho^2 + v^2\right). \tag{3.3}$$

We can also write the potential flow equations in matrix form:

$$\begin{bmatrix} \rho_t \\ v_t \end{bmatrix} + \begin{bmatrix} v & \rho \\ 3\rho & v \end{bmatrix} \begin{bmatrix} \rho_x \\ v_x \end{bmatrix} = 0. \tag{3.4}$$

Let $\vec{u} = \begin{bmatrix} \rho & v \end{bmatrix}^T$ and $A$ be the coefficient matrix in front of $\begin{bmatrix} \rho_x & v_x \end{bmatrix}^T$. The eigenvalues and corresponding normalized eigenvectors of $A$ are

$$\lambda = v \pm \sqrt{3}\rho, \quad \vec{r}_\pm = \frac{1}{2}\begin{bmatrix} 1 & \pm\sqrt{3} \end{bmatrix}^T. \tag{3.5}$$

The system is strictly hyperbolic as long as $\rho \neq 0$. Note $\sqrt{3}\rho$ is the sound speed from equation (2.18).

We verify that the system is genuinely nonlinear by determining whether

$$\nabla\lambda_\pm \cdot \vec{r}_\pm \neq 0, \tag{3.6}$$

which for the system in equation (3.4), evaluates to $\pm 2\sqrt{3}$. So the system is genuinely nonlinear. Knowledge of the eigenvalues and the system's genuine nonlinearity is key to construct a rarefaction solution, which we do in the following section.

## 3.3 Rarefaction Theory

We first give a brief heuristic for why we expect a rarefaction to emerge. The conservation of momentum equation (3.4) can be written as

$$v_t + vv_x = -3\rho\rho_x.$$

which is Burgers' equation with a source term. Although the velocity is initially zero, the source term on the right instantaneously initializes the velocity. But due to the non-differentiability of the cutoff, the source term is initially discontinuous with the source term being negative for all $x < x^*$ and zero for all $x > x^*$. This discontinuity in source term would lead to a discontinuity in velocity as well, causing a rarefaction to emerge from $x^*$. Another way of arriving at this conclusion is by considering the Lagrangian particle positions. For $x < x_0$, the initial data is the same as the Kidder problem initial data. The Lagrangian position of particles for the Kidder solution is given by equation (2.35). If all particles originating from $x < x_0$ follow this trajectory, they would all arrive at the origin at time $t = 1$. However, since the solution is stationary to the right of $x_0$, the Lagrangian position of those particles remain stationary. The contrasting characteristic behavior on different sides of $x^*$ leads to a gap in the characteristic diagram, indicating a rarefaction should fill in the empty space in the characteristic diagram. A sketch of this characteristic diagram is shown in Figure 3.1. We are thus motivated to look for rarefaction solutions to the original problem.

To construct a rarefaction solution, suppose the system admits the similarity variable $y = \frac{x}{t}$. The similarity variable may be shifted in space and time arbitrarily due to the time and position shift invariance of systems of hyperbolic conservation laws in 1D planar geometry. Also suppose on the rarefaction region $y_1 \leq y \leq y_2$ the solution is of the form $\vec{w}(y) = \begin{bmatrix} \rho(\frac{x}{t+a}) & v(\frac{x}{t+a}) \end{bmatrix}^T$ where $y_1, y_2$ is to be determined. The similarity solution $\vec{w}$ must satisfy the ODE

$$\vec{w}'(y) = \frac{r_\pm(y)}{\nabla \lambda_\pm(\vec{w}(y)) \cdot r_\pm(y)}. \tag{3.7}$$

The denominator of (3.7) will always be nonzero as long as genuine nonlinearity, condition (3.6), is satisfied.

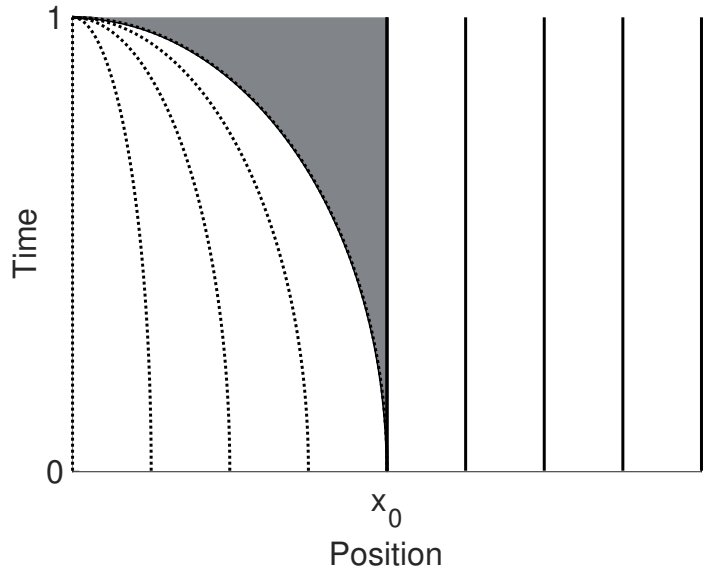


Figure 3.1: Predicted characteristics stemming from the cutoff implosion initial data. The characteristics left of the cutoff position $x_0$ (dashed lines) are expected to follow the Lagrangian position described in equation (2.35). The characteristics right of the cutoff position $x_0$ (solid lines) are expected to remain vertical since the initial velocity and density is constant in this region. A rarefaction is expected to emerge from $x_0$ to fill in the empty space of the characteristic diagram, indicated by the region shaded in gray.

## 3.4 Construction of the Cutoff Implosion Solution

We solve the ODE system in (3.7) with our eigenvalues and eigenvectors (3.5) to obtain

$$\begin{bmatrix} \rho'(y) \\ v'(y) \end{bmatrix} = \frac{1}{2} \begin{bmatrix} \pm\frac{\sqrt{3}}{3} \\ 1 \end{bmatrix},$$

which have the solutions

$$\rho(y) = \pm\frac{1}{2}\frac{\sqrt{3}}{3}y + \rho_0, \quad v(y) = \frac{1}{2}y + v_0. \tag{3.8}$$

with the sign dependent on whether we consider $\lambda_+$ or $\lambda_-$.

We now address admissibility. First, since we have genuine nonlinearity, $\lambda_\pm$ is monotone increasing along the integral curve. This means that two states $u_l$ and $u_r$ can always be

connected by a rarefaction wave given

$$\lambda_{\pm}(u_r) < \lambda_{\pm}(u_r). \tag{3.9}$$

From the previous discussion, we expect to see a rarefaction solution emerging from the cutoff position $x^*$. Arguing via finite speed of propagation for the strictly hyperbolic system, we posit for all times $t < \tilde{t}$ where $\tilde{t}$ is yet to be determined and may be infinite, there exists an interval $[0, \tilde{x}(t))$ for positive real valued function $\tilde{x}(t)$ such that the solution is the Kidder solution on this interval.

We wish to determine when the admissibility criteria (3.9) holds with left state $\vec{u}_l = \begin{bmatrix} \frac{\sqrt{3}}{3}\frac{x}{1-t^2} & -\frac{xt}{1-t^2} \end{bmatrix}^T$ (representing the Kidder solution) and right state $\vec{u}_r = \begin{bmatrix} \frac{\sqrt{3}}{3}x^* & 0 \end{bmatrix}^T$ (representing the constant state). By checking the values of $(x,t)$ such that $\lambda_+(\vec{u}_l) < \lambda_+(\vec{u}_r)$ holds with the choices of left and right state, we obtain the inequality

$$\frac{x}{t+1} < x^*.$$

The 2-eigenvalue $\lambda_+$ is used since this rarefaction corresponds to the 2-rarefaction. Applying the same methodology with the 1-rarefaction emerging from $-x^*$ yields equivalent results. From the above analysis, the upper bound of the rarefaction region is given by $x^*(1+t)$. More provocatively, this implies the similarity variable is $y = \frac{x}{t+1}$, which is a valid form for the similarity variable given the previous comments about the similarity variable permitting time shifts.

Continuing with the construction of the rarefaction analysis, the rarefaction solution must continuously agree with the right state at $y = x^*$. Applying that initial condition into equation (3.8) in the original coordinates $(x,t)$ yields

$$\rho(x,t) = \frac{1}{2}\frac{\sqrt{3}}{3}\frac{x}{t+1} + \frac{\sqrt{3}}{3}x^*, \quad v(x,t) = \frac{1}{2}\frac{x}{t+1} - \frac{1}{2}x^* \tag{3.10}$$

on the rarefaction region.

So far, we have determined the form of the rarefaction and the upper bound on the rarefaction region, but such analysis has not indicated the lower bound of the rarefaction region. To obtain this, we argue the rarefaction solution must connect continuously to the

Kidder solution at the previously defined position $\tilde{x}(t)$ for all times the implosion solution exists. Thus, we search for $\tilde{x}(t)$ such that the density and velocity match in the Kidder solution and in the rarefaction solution:

$$\frac{\sqrt{3}}{3}\frac{\tilde{x}(t)}{1-t^2} = \frac{1}{2}\frac{\sqrt{3}}{3}\left(\frac{\tilde{x}(t)}{1+t} + x^*\right) \quad \text{and} \quad -\frac{\tilde{x}(t)t}{1-t^2} = \frac{1}{2}\frac{\tilde{x}(t)}{1+t} - \frac{1}{2}x^*$$

to find $\tilde{x}(t) = x^*(t-1)$. We now have completed our description of the rarefaction and can explicitly state the solution of the cutoff implosion problem. The density is given by

$$\boxed{\rho(x,t) = \begin{cases} \frac{\sqrt{3}}{3}\frac{|x|}{1-t^2} & \text{if } |x| \le x^*(1-t) \\ \frac{1}{2}\frac{\sqrt{3}}{3}\left(\frac{|x|}{1+t} + x^*\right) & \text{if } x^*(1-t) \le |x| \le x^*(1+t) \\ \frac{\sqrt{3}}{3}x^* & \text{if } x^*(1+t) \le |x| \end{cases},} \tag{3.11}$$

and the velocity is given by

$$\boxed{v(x,t) = \begin{cases} -\frac{xt}{1-t^2} & \text{if } |x| \le x^*(1-t) \\ \frac{1}{2}\left(\frac{x}{1+t} - x^* \operatorname{sgn} x\right) & \text{if } x^*(1-t) \le |x| \le x^*(1+t) \\ 0 & \text{if } x^*(1+t) \le |x| \end{cases}.} \tag{3.12}$$

## 3.5 Analysis of the Cutoff Implosion Solution

We now discuss some of the salient features of our constructed cutoff implosion solution. The most pressing question is whether the cutoff implosion solution still implodes. We have determined the lower bound of the rarefaction region is $x^*(1-t)$. The rarefaction reaches the origin by time $t = 1$, which remarkably is also the original implosion time. On the other hand, the region where the Kidder solution exists on vanishes at time $t = 1$, regardless of where the cutoff is.

This does not necessarily imply the cutoff implosion solution does not implode. It may be true that as $t \to 1$, the density around the origin still grows without bound. We will show this cannot be the case via asymptotics. Let $t \to 1$ and set $t = 1 - \epsilon$ for small $\epsilon > 0$. We check the value of the density and velocity at the lower bound of the rarefaction region, so

at position $x = x^*(1-t) = \epsilon x^*$. For density, we find

$$\rho(\epsilon x^*, 1-\epsilon) = \frac{\sqrt{3}}{3}\frac{x^*}{2-\epsilon}$$

which approaches $\frac{1}{2}\frac{\sqrt{3}}{3}x^*$ as $\epsilon \to 0$, or equivalently $t \to 1$. For velocity, we find

$$v(\epsilon x^*, 1-\epsilon) = x^*\frac{\epsilon - 1}{2-\epsilon}$$

which approaches $\frac{-x^*}{2}$ as $\epsilon \to 0$. From our asymptotic analysis, we see the rarefaction suppresses the Kidder solution and the cutoff imploding solution does not implode. Again, this is true no matter where the original cutoff is, but we can increase the density near the origin as large as desired by increasing the cutoff position $x^*$.

We comment more on the rarefaction itself. The rarefaction variable $y = \frac{x}{t+1}$ is an unusual modification of the standard rarefaction $\frac{x}{t}$. Although unusual, the time shifted rarefaction variable occurs due to having a non constant left state. This setup is similar to the generalized Riemann problem, where both initial states are allowed to be non constant (see [Li94] for more details). In particular, the time shift of 1 in the rarefaction variable is notable as $t = 1$ is the original imploding time of the Kidder solution. We find it remarkable that the rarefaction variable encodes the original imploding time although the cutoff implosion solution no longer implodes.

The rarefaction region can be viewed as the region of influence originating from the cutoff position. We expect the left and right endpoints of the rarefaction region travels at speed $\lambda_-$ and $\lambda_+$ respectively, and we verify this. Since the solution is a rarefaction and connects continuously to the Kidder solution to the left and constant cutoff to the right, the density and velocity at the left and right endpoints of the rarefaction region are the density and velocity of the Kidder solution and constant cutoff respectively, which we know explicitly. Looking on the positive real axis, the motion of the left endpoint satisfies

$$\dot{x}_l = \lambda_-(\rho_l, v_l) = -\frac{x_l}{1-t}, \quad x_l(0) = x^* \tag{3.13}$$

and the right endpoint satisfies

$$\dot{x}_r = \lambda_+(\rho_r, v_r) = x^*, \quad x_r(0) = x^*. \tag{3.14}$$

We can solve ODEs (3.13) and (3.14) to obtain the positions for the left endpoint and right endpoint of the rarefaction region as

$$x_l(t) = x^*(1-t), \quad x_r(t) = x^*(1+t)$$

which are the rarefaction region endpoints obtained previously. This supports our intuition on how the region of influence of the cutoff point appears in the cutoff implosion solution.

We end by discussing the speed of sound in the cutoff implosion solution. Noticeably, the solution remains subsonic for all times up to $t = 1$. The speed of sound is obtained by substituting the density in equation (3.11) into the speed of sound formula of equation (2.18):

$$|c(x,t)| = \begin{cases} \frac{x}{1-t^2} & \text{if } 0 \le |x| \le x^*(1-t) \\ \frac{1}{2}\left(\frac{x}{1+t} + x^*\right) & \text{if } x^*(1-t) \le |x| \le x^*(1+t) \\ x^* & \text{if } x^*(1+t) \le |x| \end{cases}. \tag{3.15}$$

We compare the magnitude of the velocity to the local speed of sound on every region. Without loss of generality, we consider only the positive real axis. On the Kidder solution region,

$$\left| -\frac{xt}{1-t^2} \right| \le \frac{x}{1-t^2}$$

as long as $0 \le t < 1$, so the imploding solution is subsonic. On the rarefaction region,

$$v(x,t) = \frac{1}{2}\left(x^* - \frac{x}{1+t}\right) \le \frac{1}{2}\left(x^* + \frac{x}{1+t}\right) \le c(x,t).$$

Finally, in the constant region the flow is stationary. So, for all time $t < 1$, the flow is subsonic. Recall the Kidder solution becomes supersonic at some time before 1 for any higher dimension. In the following chapter, we will see the cutoff implosion solution still implodes, and we postulate whether an interpretation regarding the speed of sound can inform intuition on the different behaviors.

## 3.6 Continuation Past $t = 1$

As the cutoff implosion solution does not implode at $t = 1$, we can try to extend the solution past $t = 1$. The previously performed asymptotic analysis describes the behavior of

the density and velocity at the origin. At $t = 1$, the density at the origin is continuous but jumps up to $\frac{1}{2}\frac{\sqrt{3}}{3}x^*$ after being zero for all times beforehand. On the other hand, the velocity at the origin is discontinuous at $t = 1$ taking the value of $\frac{x^*}{2}$ from the left and $-\frac{x^*}{2}$ from the right. We can define the initial condition naturally arising from continuing the cutoff implosion solution past $t = 1$ as

$$\rho(x,1) = \begin{cases} \frac{1}{2}\frac{\sqrt{3}}{3}\left(\frac{|x|}{2} + x^*\right) & \text{if } 0 \le |x| \le 2x^* \\ \frac{\sqrt{3}}{3}x^* & \text{if } 2x^* \le |x| \end{cases} \tag{3.16}$$

and

$$v(x,1) = \begin{cases} \frac{1}{2}\left(\frac{x}{2} - x^* \operatorname{sgn} x\right) & \text{if } 0 < |x| < 2x^* \\ 0 & \text{if } 2x^* \le |x| \end{cases}. \tag{3.17}$$

To continue the solution for $t > 1$, we construct a solution to the generalized Riemann problem with initial data given by equations (3.16) and (3.17). Existence theory showing how the solution of the generalized Riemann problems takes the form of its associated Riemann problem is established in [Li94]. Asymptotic expansions in the similarity variable are considered in [LR88] and constructed explicitly for first order in the case of gas dynamics in [BLR89]. The authors of [BF84] considered generalized Riemann problems with linear initial data to construct higher order numerical schemes, and an extension for arbitrary polynomial initial data is discussed in [Tor09].

As seen in the velocity initial condition (3.17), the characteristics at the origin at time $t = 1$ collide, forming a shock. Due to the symmetry of the solution, we predict a double shock solution to form. If a shock forms and moves to the right from the origin, it must also form and move to the left from the origin, creating a double shock. The properties of these shocks, such as their position and speed, are reflected as well. To determine the double shock structure and intermediate state emanating from the origin, we treat the initial condition as a Riemann problem locally around the origin at time $t = 1$.

Turning to the theory of Riemann problems, a shock is admissible between two given states $\vec{u_l} = \begin{bmatrix} \rho_l(x,t) & v_l(x,t) \end{bmatrix}^T$ and $\vec{u_r} = \begin{bmatrix} \rho_r(x,t) & v_r(x,t) \end{bmatrix}^T$ if it satisfies the Rankine-

Hugoniot condition

$$\dot{s}(t) = \frac{f(\rho_r, v_r) - f(\rho_l, v_l)}{\rho_r - \rho_l} = \frac{g(\rho_r, v_r) - g(\rho_l, v_l)}{v_r - v_l} \tag{3.18}$$

with the fluxes $f, g$ as defined in equation (3.3), $s(t)$ denoting the shock position, $\dot{s}(t)$ denoting the shock speed, and the understanding that the left and right states vary in space and time. We note our choice of continuing to use the fluxes in equation (3.3) is for continuity and mathematical tractability of this work rather than physical accuracy. In general, we do not expect the Rankine-Hugoniot condition to be satisfied in general between any generic pair of left and right states. So, we search for an intermediate state $u^* = (\rho^*, v^*)$ such that the Rankine-Hugoniot condition is satisfied between $u_l$ and $u^*$,

$$\frac{f(\rho^*, v^*) - f(\rho_l, v_l)}{\rho^* - \rho_l} = \frac{g(\rho^*, v^*) - g(\rho_l, v_l)}{v^* - v_l}, \tag{3.19}$$

and $u^*$ and $u_r$,

$$\frac{f(\rho_r, v_r) - f(\rho^*, v^*)}{\rho_r - \rho^*} = \frac{g(\rho_r, v_r) - g(\rho^*, v^*)}{v_r - v^*}. \tag{3.20}$$

However, not all shock connections satisfying equations (3.19) and (3.20) are physically admissible, so we also enforce the entropy condition

$$\lambda_i(\vec{u}_l(s_i(t), t)) > \dot{s}_i > \lambda_i(\vec{u}_r(s_i(t), t)). \tag{3.21}$$

We may form a local Riemann problem by defining the left and right constant states to be $\vec{u_l}^0 = \lim_{x\to 0^-} \begin{bmatrix}\rho(x,1) & v(x,1)\end{bmatrix} = \begin{bmatrix}\frac{1}{2}\frac{\sqrt{3}}{3}x^* & \frac{1}{2}x^*\end{bmatrix}$ and the right constant to be $\vec{u_r}^0 = \lim_{x\to 0^+} \begin{bmatrix}\rho(x,1) & v(x,1)\end{bmatrix} = \begin{bmatrix}\frac{1}{2}\frac{\sqrt{3}}{3}x^* & -\frac{1}{2}x^*\end{bmatrix}$. The solution satisfying the entropy condition (3.21) has a double shock structure with intermediate state $u^{*,0} = \begin{bmatrix}\rho^{*,0} & v^{*,0}\end{bmatrix}^T = \begin{bmatrix}\frac{\sqrt{3}}{3}x^* & 0\end{bmatrix}^T$. The local Riemann solution acts as the leading order behavior of the solution to the generalized Riemann problem as described in [Li94], [LR88], [BF84], and [Tor09] and we refer to it as the *associated Riemann problem*.

Now for the generalized Riemann problem, the left and right states are no longer constant, and *a priori* neither is the intermediate state. Let $s(t)$ be the position of the shock on the positive axis with $-s(t)$ being the position of the shock on the negative axis. For the

continuation problem, the left state is

$$\vec{u_l}(-s(t),t) = \left[\frac{1}{2}\frac{\sqrt{3}}{3}\left(\frac{s(t)}{1+t}+x^*\right) \quad \frac{1}{2}\left(-\frac{s(t)}{1+t}+x^*\right)\right]^T \tag{3.22}$$

and the right state is

$$\vec{u_r}(s(t),t) = \left[\frac{1}{2}\frac{\sqrt{3}}{3}\left(\frac{s(t)}{1+t}+x^*\right) \quad \frac{1}{2}\left(\frac{s(t)}{1+t}-x^*\right)\right]^T. \tag{3.23}$$

The left and right states are understood to be the continuation of the rarefaction in equations (3.11) and (3.12). For brevity, we notate the right density and velocity as $\rho$ and $v$ and the left density and velocity as $\rho$ and $-v$ using the symmetry. Similarly, denote $\rho^* = \rho^*(s) = \rho^*(-s)$ and $v^* = v^*(s) = -v^*(-s)$. Applying the left and right states to equations (3.19) and (3.20) with the fluxes defined in equation (3.3) yield

$$\frac{-\rho^* v^* + \rho v}{\rho^* - \rho} = \frac{1}{2}\frac{3(\rho^*)^2 + (v^*)^2 - 3\rho^2 - v^2}{-v^* + v} \tag{3.24}$$

and

$$\frac{\rho v - \rho^* v^*}{\rho - \rho^*} = \frac{1}{2}\frac{3\rho^2 + v^2 - 3(\rho^*)^2 - (v^*)^2}{v - v^*} \tag{3.25}$$

where $\rho^*$ and $v^*$ are understood to be functions of $s$. Equations (3.24) and (3.25) represent the same value with opposite sign because each represents the shock speed to the left and right respectively. Without loss of generality, we solve the Rankine-Hugoniot condition (3.25) for $v^*$ yielding the polynomial

$$0 = (\rho + \rho^* *)(v^*)^2 - 2(\rho+\rho^*)v^* - 3(\rho^*)^3 + 3\rho(\rho^*)^2 + (v^2+3\rho^2)\rho^* - 3\rho^3 + v^2\rho \tag{3.26}$$

which has roots

$$v^* = v \pm \sqrt{3}(\rho^* - \rho) \tag{3.27}$$

using the fact $\rho = \rho^*$ is a root in $\rho$ of the constant term in $v^*$. To determine which of (3.27) is permissible, the entropy condition (3.21) is employed to check $\lambda_+(u^*) > \lambda_+(\vec{u}_r)$, finding $v^* = v + \sqrt{3}(\rho^* - \rho)$ is the entropy satisfying intermediate state.

In general, the intermediate state on the region between the shocks is not constant, although the constant intermediate state for the associated Riemann problem does satisfy constraint (3.27). We will now argue the constant state $u^{*,0}$ is also the intermediate state

for the generalized Riemann problem. First, we consider a power series expansion in time around $x = 0, t = 1$ for the solution $\vec{u}(x,t)$ as done in [Tor09] which takes the form

$$\vec{u}_{LR}(t) = u^{*,0} + \sum_{k=1}^{K} \partial_t^k \vec{u}(0,1^+) \frac{(t-1)^k}{k!} \tag{3.28}$$

for some time $t \geq 1$.

To compute $\partial_t^k \vec{u}(0,1^+)$, [BF84] and [Tor09] propose studying the evolution of the spatial derivatives and transforming them into $\partial_t^k \vec{u}(0,1^+)$. In our case, we can directly use the explicit form of the solution in equations (3.11) and (3.12) to obtain the time derivatives, computing $\partial_t^k \vec{u}(0,1^+)$ to be zero. The power series representation is subsequently

$$\vec{u}_{LR}(t) = u^{*,0},$$

implying at the origin the solution is the constant intermediate state of the associated Riemann problem for some time interval. Note following the procedure of [BF84] and [Tor09] yields the same result. By evaluating the PDEs (3.2) at $x = 0$ and using the facts $\rho_t(0,t) = v_t(0,t) = 0$ and $v^{*,0} = 0$ on this time interval, it can be shown $\rho_x(0,t) = v_x(0,t) = 0$. Performing the same procedure on PDEs (3.2) after taking further time derivatives shows $\partial_x^k \rho(0,t) = \partial_x^k v(0,t) = 0$ as well. If $\rho$ and $v$ are assumed to be analytic in space at $x = 0$ on this time interval, then $\rho$ and $v$ are constants on the intermediate region. Although analyticity is not guaranteed for solutions of hyperbolic conservation laws, we take the intermediate state for the generalized Riemann problem to be the constant $u^* = u^{*,0} = \begin{bmatrix} \frac{\sqrt{3}}{3} x^* & 0 \end{bmatrix}^T$ as an assumption to continue constructing the shock solution.

Thus, the solution takes the form

$$\rho(x,t) = \begin{cases} \frac{\sqrt{3}}{3} x^* & \text{if } |x| \leq s(t) \\ \frac{1}{2} \frac{\sqrt{3}}{3} \left( \frac{|x|}{1+t} + x^* \right) & \text{if } s(t) \leq |x| \leq x^*(1+t) \\ \frac{\sqrt{3}}{3} x^* & \text{if } x^*(1+t) \leq |x| \end{cases} \tag{3.29}$$

and

$$v(x,t) = \begin{cases} 0 & \text{if } |x| \leq s(t) \\ \frac{1}{2}(\frac{x}{1+t} - x^* \operatorname{sgn} x) & \text{if } s(t) \leq |x| \leq x^*(1+t) \\ 0 & \text{if } x^*(1+t) \leq |x| \end{cases} \tag{3.30}$$

All that is left is to determine the position and speed of the shock $s(t)$ emanating from the origin. We apply the Rankine-Hugoniot condition for the right moving shock with left state $\vec{u_l} = \begin{bmatrix} \frac{\sqrt{3}}{3}x^* & 0 \end{bmatrix}^T$ and $\vec{u_r} = \left[\frac{1}{2}\frac{\sqrt{3}}{3}\left(\frac{s(t)}{1+t} + x^*\right), \frac{1}{2}\left(\frac{s(t)}{1+t} - x^*\right)\right]^T$ to obtain

$$\dot{s}(t) = \frac{1}{2}\left(\frac{s}{1+t} + x^*\right) \tag{3.31}$$

which is an ODE in $s(t)$. The ODE of equation (3.31) is equipped with the initial condition $s(1) = 0$, signifying the shock originates at the origin at time $t = 1$ and has solution

$$s(t) = x^*\left((1+t) - (2(1+t))^{\frac{1}{2}}\right). \tag{3.32}$$

The shock cannot catch up to the rarefaction as the right endpoint position of the rarefaction region is given by $x^*(1+t)$. Thus, the solution to the cutoff implosion problem past $t = 1$ is given by equations (3.29) and (3.30) with shock position given by equation (3.32).

## 3.7 Numerical Results

We complement our analysis with numerical simulations of the potential flow equations in equations (3.2) with the cutoff implosion initial data in equation (3.1). Our goal is to verify the analytical solution by comparing it to a numerically computed solution. We also would like to determine whether various predicted features - such as the similarity variable $y$ - are also present in the numerical solution.

To perform the numerical simulation, we use a standard Lagrangian leapfrog scheme as introduced in [NR50] and further developed by [Noh87]. In this Lagrangian scheme, the spatial domain is interspersed with nodes, where the kinematic variables such as velocity and position are defined. In between the nodes are the fluid elements, where variables such as the density and pressure are defined. Lagrangian schemes are characterized by how they allow

the nodes themselves to move in time. The most prominent feature of the scheme presented in [NR50] and [Noh87] is the introduction of artificial viscosity in the pressure terms to better resolve shocks. However, since we do not expect or see shocks in our numerical simulations, we set artificial viscosity terms to zero in our calculations. More discussion of the numerical method is found in Chapter 5.

For the numerical simulations, we use a numerical domain of $[0, 5]$ with 1501 nodes and 1500 zones. Initially, the nodes are equally spaced, but their positions change over time via the dynamics of the Lagrangian numerical scheme. We use dynamic time stepping to ensure our time steps always meet a Courant–Friedrichs–Lewy (CFL) condition up to ending time $T = 0.999$ with Courant number $C = 0.1$. We set the leftmost node boundary condition as $v = 0$ at $x = 0$ and the rightmost node boundary condition as $v = 0$ at $x = 5$. This is justified as the velocity of the Kidder solution remains 0 at $x = 0$ up until the original implosion time. For the right boundary condition, as long as the density remains constant at $x = 5$, the velocity will also remain 0 as well. We select the cutoff position in our initial data to be $x^* = 2.5$.

The initial data we use for our numerical simulations as presented in equation (3.1) is shown in Figure 3.2. In our numerical simulations, we overlay the analytical solution for density and velocity found in equations (3.11) and (3.12) for comparison. We also overlay the local sound speed in the velocity plots. Figure 3.3 shows the evolution of the density at time snapshots of approximately $t = 0.25$, $t = 0.5$, $t = 0.75$, and $t = 1$. Figure 3.4 does the same for the velocity. In order to verify the proposed similarity variable of $y = \frac{x}{t+1}$, we plot the computed density and velocity against $y$ for various times in Figure 3.5. Similarly, we plot the computed density and velocity against a different similarity variable $\eta = \frac{x-2.5}{t}$ to determine the location of the rarefaction region in Figure 3.6.

To quantitatively compare the numerical results to the analytical solution, we also compute the $L^1$ error norm between the two solutions, given by (4.35).

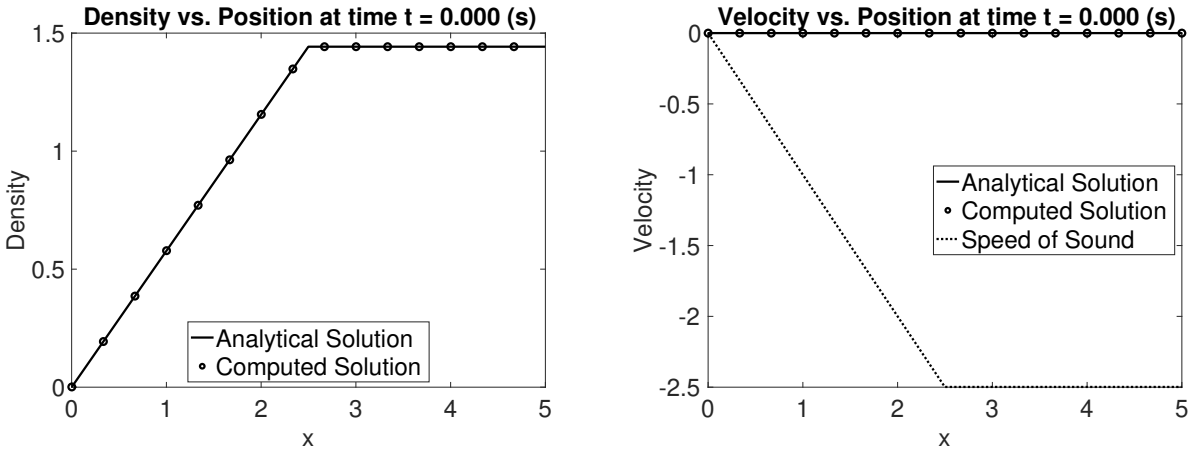


(a) Density

(b) Velocity

Figure 3.2: Initial data for the cutoff implosion problem.

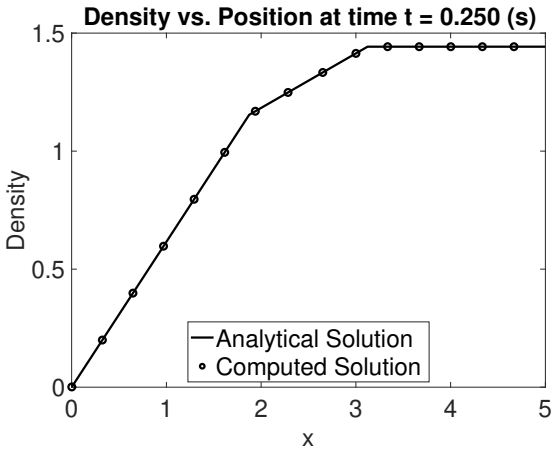


(a) $t \approx 0.25$

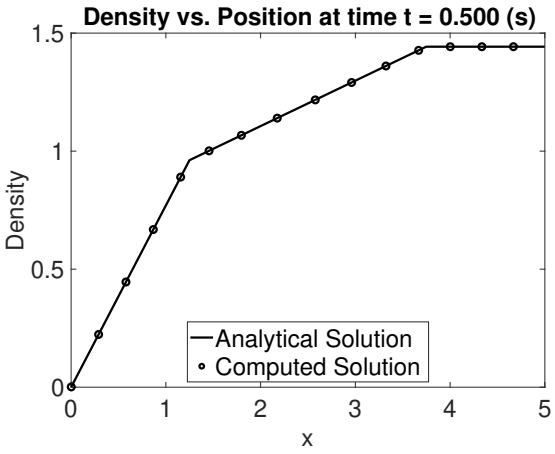


(b) $t \approx 0.5$

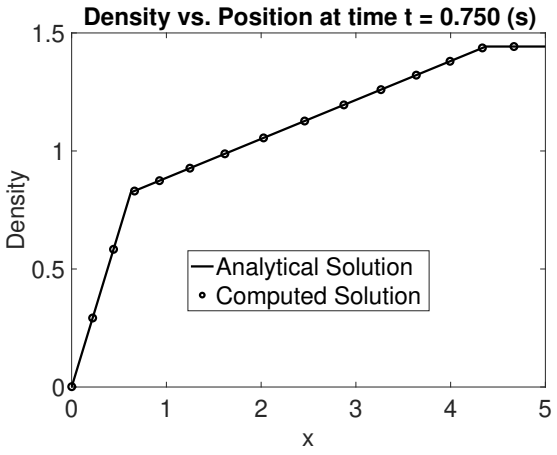


(c) $t \approx 0.75$

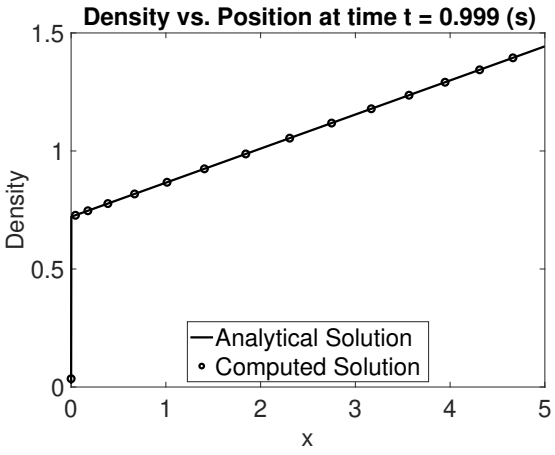


(d) $t \approx 1$

Figure 3.3: Analytical solution and selected representatives of the computed solution for density at approximate times $t = 0.25, 0.5, 0.75$ and $t = 1$.

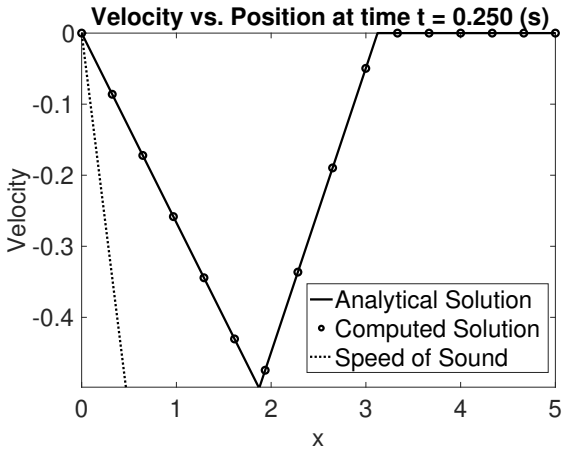


(a) $t \approx 0.25$

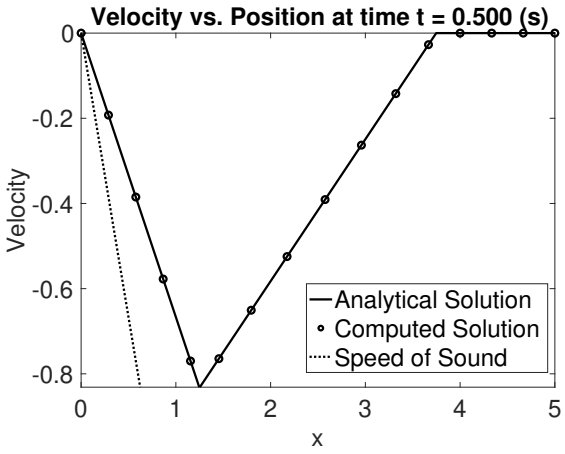


(b) $t \approx 0.5$

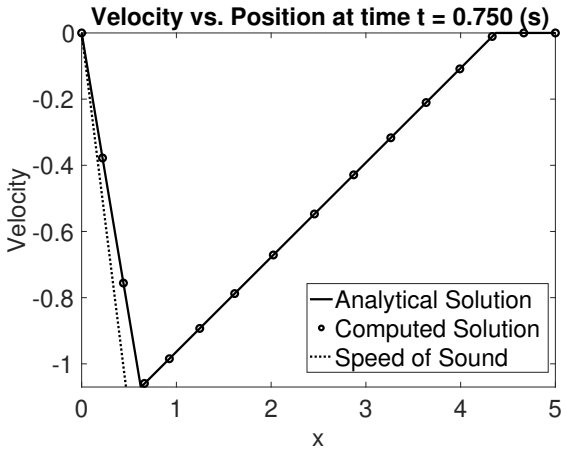


(c) $t \approx 0.75$

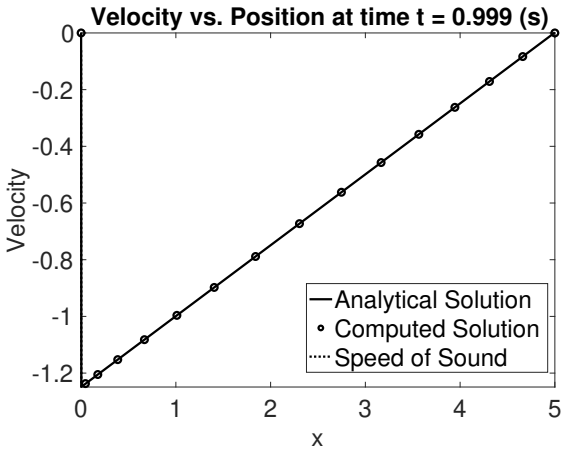


(d) $t \approx 1$

Figure 3.4: Analytical solution and selected representatives of the computed solution for velocity as well as the local speed of sound at approximate times $t = 0.25, 0.5, 0.75$ and $t = 1$.

## 3.8 Discussion

In this section, we will discuss the results of the numerical simulations shown in Figures 3.3, 3.4, and 3.5 and Table 3.1.

First, comparing the analytical solution in equations (3.11) and (3.12) to the computed

| $t$ | $\rho$ | $v$ |
|---|---|---|
| 0.25 | $2.28 \cdot 10^{-5}$ | $2.36 \cdot 10^{-5}$ |
| 0.50 | $3.37 \cdot 10^{-5}$ | $3.81 \cdot 10^{-5}$ |
| 0.75 | $4.01 \cdot 10^{-5}$ | $5.03 \cdot 10^{-5}$ |
| 0.99 | $4.08 \cdot 10^{-5}$ | $6.00 \cdot 10^{-5}$ |

Table 3.1: Calculated $L^1$ error between the analytical and computed solutions for density and velocity at various times.

density in Figure 3.3 and Figure 3.4, we find excellent visual agreement between the analytical and computed solutions. In particular, the computed solution captures the sharp corners corresponding to discontinuous gradient well. Diffusive numerical schemes such as Lax-Friedrichs will smoothen out such sharp edges. Sampled data points from the computed solution seem to align exactly with the analytical solution. This visual agreement is corroborated with the small computed $L^1$ error displayed in Table 3.1. Both the qualitative and quantitative agreement instills confidence that our proposed analytical solution is correct, coupled with the discussion about unique solutions in Chapter 6. We next determine various features we expect to see in the numerical simulation.

The computed density and velocity are split into three distinct regions. In the first region, the computed solution follows the Kidder solution. In the third region, the computed solution remains constant. In between, the computed solution connects the Kidder solution on the left to the constant solution on the right. This follows the predictions made by our derived analytical solution.

In our analytical solution, we posited the middle region is a rarefaction with similarity variable $y = \frac{x}{t+1}$. To verify this, we plot the computed solution at various times against this proposed similarity variable in Figure 3.5. We see the solutions all follow a similar structure. They originate at the origin and grow linearly until collapsing onto the same curve. This continues until a later value of $y$ in which the solution becomes constant.

We can explain this behavior in relation to the original structure of the computed solution. The first region represents the solutions obeying the Kidder solution. Plotted against the

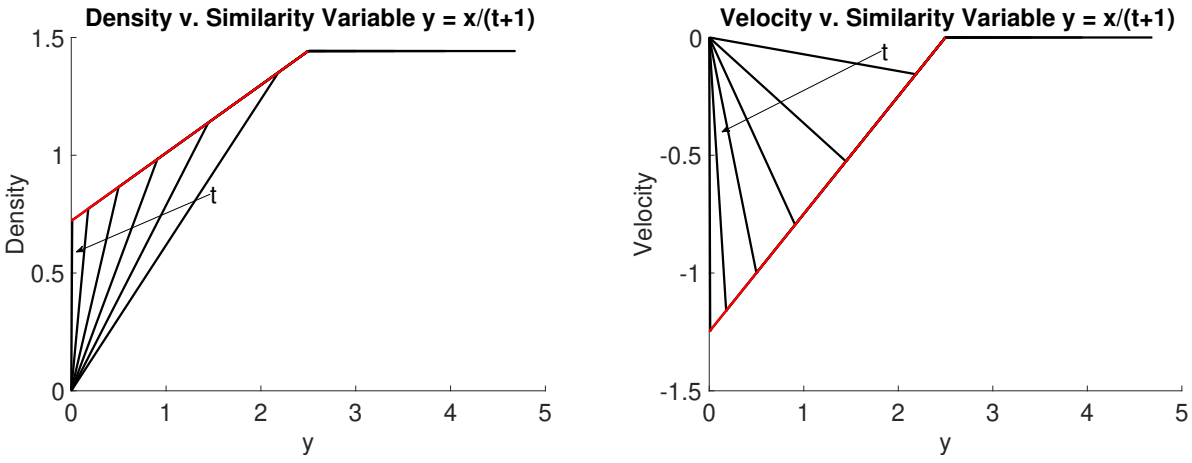


(a) Density

(b) Velocity

Figure 3.5: Computed density and velocity plotted as a function of the similarity variable $y = \frac{x}{t+1}$ at increasing times in the direction of the arrow, as predicted in the analytical expressions for the density and velocity in equations (3.11) and (3.12). The approximate times are $t = 0$, 0.20, 0.33, 0.46, 0.60, 0.73, 0.87 and 0.97. At each time snapshot, the solution collapses onto the same middle region as highlighted in red.

similarity variable, the solution follows different curves for different times. As the solution enters the rarefaction region, the solution collapses onto the same curve for every time instance. This verifies the solution is self-similar with our proposed similarity variable $y = \frac{x}{t+1}$. The third region simply indicates the solution becomes constant past a certain value.

Further verifying the rarefaction, we can check the endpoints of the rarefaction region by plotting the computed solution against a different similarity variable, $\eta = \frac{x-x^*}{t}$, where in our case $x^* = 2.5$. From observing the initial data, we may hypothesize the rarefaction variable should be $\eta$ as we expect a rarefaction to emerge from spatial point $x^*$ at time $t = 0$. As a stark difference from plotting the computed solutions against $y = \frac{x}{t+1}$, the solutions do not collapse onto the same curve in the rarefaction region, which supports the fact that the rarefaction similarity variable is $y$ and not $\eta$. In contrast, we do see the domain of the rarefaction is constant with respect to this variable. In particular, we see in Figure 3.6 the left endpoint of the rarefaction region corresponds to $\eta = -2.5 = -x^*$ and the right endpoint corresponds to $\eta = 2.5 = x^*$. This implies the left endpoint and right endpoint of

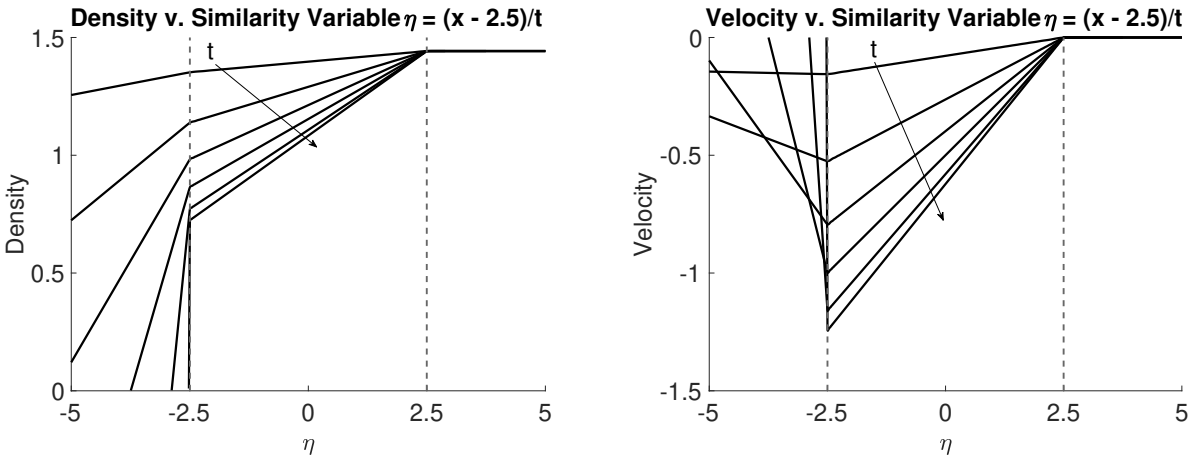


(a) Density

(b) Velocity

Figure 3.6: Density and Velocity plotted as a function of the similarity variable $\eta = \frac{x-2.5}{t}$ at increasing times in the direction of the arrow. The approximate times are $t = 0$, 0.20, 0.33, 0.46, 0.60, 0.73, 0.87 and 0.97. Note the solutions at various time snapshots does not collapse onto the same curve, indicating the solution is not self-similar in $\eta$. However, the left and right boundaries of the middle region are invariant with respect to $\eta$.

the rarefaction region are located at $x = x^*(1 - t)$ and $x = x^*(1 + t)$ as we predicted.

The last feature we discuss is the comparison between the computed velocity and the computed sound speed. Indeed, by substituting our computed density into the formula for the local sound speed in equation (2.18), we observe throughout the evolution of the velocity the flow remains subsonic for all of the computation time as seen in Figure 3.4.

# CHAPTER 4

# Cutoff Implosion in Higher Dimensions

In this chapter, we study the cutoff implosion problem in higher dimensions. By continuously cutting off the initial data of (2.38) at some point $r^*$, we obtain the *cutoff implosion* initial data

$$\rho(r,0) = \begin{cases} \left(\frac{1}{n+3}\right)^{(n+1)/2} r^{n+1} & \text{for } r \le r^* \\ \left(\frac{1}{n+3}\right)^{(n+1)/2} (r^*)^{n+1} & \text{for } r \ge r^* \end{cases}, \quad v(r,0) = 0. \tag{4.1}$$

## 4.1 Region of Influence of the Cutoff Position

Analysis in higher dimensions is complicated by the presence of the source term $\frac{n\rho v}{r}$ in (2.19). Because of the source term, we do not expect a traditional rarefaction to emerge from the cutoff point unlike in 1D. Asymptotic expansions, as presented in [LR88, BLR89], can be used to approximate the solution for small times. The rarefaction solution of the Riemann problem without the source term is used as the leading order term. As a result, the rarefaction solution can be used as an approximate solution for the equations with source term for small time, a feature leveraged by numerical methods based on the asymptotic expansions described in [BF84, Tor09]. Global asymptotic expansions exist when the source

term depends only on the state [LT91]. However, we are interested in the behavior of the solution for larger times and our source term depends on the spatial variable.

The interval the "rarefaction" solution is supported on is the region of influence stemming from the cutoff point $r^*$. In higher dimensions, this region is an annulus. The outer and inner radii of this annulus travel at the speed equivalent to the eigenvalues of the isentropic Euler equations, $\lambda_\pm = v \pm c$ respectively where $c$ is given by (2.5). As a nonlinear system, the eigenvalues are not constant but depend on the state at the boundary. Since the eigenvalues represent the speed of the radii, the inner radius $r_l$ and outer radius $r_r$ satisfy the ODEs

$$\dot{r_l} = \lambda_-(r_l), \quad \dot{r_r} = \lambda_+(r_r), \quad r_l(0) = r_r(0) = r^*. \tag{4.2}$$

We argue that due to the diverging structure of the characteristics from $r^*$, we should expect the solution to be continuous. This implies the solution should connect continuously to the Kidder solution at the inner radius and to the constant state at the outer radius. Both of these states are explicitly known. Note the speed of sound $c$ from (2.5) can be written in terms of $n$ given the assumed relationship between $\gamma$ and $n$ used to derive the Kidder solution:

$$c = \left(\frac{n+3}{n+1}\right)^{1/2} \rho^{1/(n+1)}. \tag{4.3}$$

The outer radius $r_r$ satisfies the ODE

$$\dot{r_r} = \frac{r^*}{\sqrt{n+1}}, \quad r_r(0) = r^*, \tag{4.4}$$

which has the solution

$$r_r(t) = r^* \left(\frac{t}{\sqrt{n+1}} + 1\right). \tag{4.5}$$

The inner radius $r_l(t)$ satisfies the more complicated ODE

$$\dot{r_l} = -r_l \left(\frac{t + (n+1)^{-\frac{1}{2}}}{1 - t^2}\right), \quad r_l(0) = r^*, \tag{4.6}$$

which has solution

$$r_l(t) = r^* \left((1-t)^{\frac{1+(n+1)^{-1/2}}{2}} (1+t)^{\frac{1-(n+1)^{-1/2}}{2}}\right). \tag{4.7}$$

Both formulas (4.7) and (4.5) reduce to the left and right endpoint formulas derived in [LRB27] when $n = 0$. The outer radius moves linearly, regardless of $n$. On the other hand, the inner radius always arrives at the origin at time $t = 1$, also regardless of $n$.

As $r_l(t)$ descends to the origin, every $v$ characteristic from $(0, r^*)$ will eventually be influenced by the $v - c$ characteristic stemming from $r^*$. Suppose a Lagrangian particle initially starts at $r_0 \in (0, r^*)$. By equating its Lagrangian position ascribed in (2.35) with the formula for the inner radius in (4.7), the two paths collide at time

$$t = \frac{1-\tau}{1+\tau}, \quad \tau = \left(\frac{r_0}{r^*}\right)^{2\sqrt{n+1}} \tag{4.8}$$

with $t \in (0, 1)$ since $\tau < 1$. So, every particle originating on $(0, r^*)$ is eventually affected by the left moving characteristic emanating from $r^*$.

We can track the density and velocity at the inner radius by evaluating the Kidder solution at $r_l(t)$. From the construction of $r_l(t)$, the cutoff implosion solution is the same as the Kidder solution on the interval $[0, r_l(t)]$. The density and velocity of the cutoff implosion solution evaluated at $r_l(t)$ is

$$\rho(r_l(t), t) = (n+3)^{-(n+1)/2} (r^*)^{n+1} (1-t)^{\frac{(n+1)^{1/2}-(n+1)}{2}} (1+t)^{\frac{-(n+1)^{1/2}-(n+1)}{2}} \tag{4.9}$$

and

$$v(r_l(t), t) = -r^* t (1-t)^{\frac{-1+(n+1)^{-1/2}}{2}} (1+t)^{\frac{-1-(n+1)^{-1/2}}{2}}. \tag{4.10}$$

Whether an implosion can occur is determined by the exponent of the $(1 - t)$ term. When $n > 0$, the exponent is negative implying the density at $r_l(t)$ goes to positive infinity and the velocity at $r_l(t)$ goes to negative infinity as $t$ approaches 1. Note $n = 0$ is a special case, as the $(1 - t)$ term drops out entirely leading to finite limits for the density and velocity instead. This behavior matches the limiting behavior observed in [LRB27]. So, implosion occurs in all dimensions higher than 1.

Note $\rho(r_l(t), t)$ is not a monotone increasing function in $t$ on $[0, 1)$ while $v(r_l(t), t)$ is a monotone decreasing function. Although $\rho(r_l(t), t)$ eventually goes to $\infty$ as $t \to 1$, there will be a time interval when the density decreases instead. In contrast, $v(r_l(t), t)$ will always decrease to $-\infty$. Since on the interval $[0, r_l(t)]$ the velocity is the same as the Kidder solution

and $v(r,t) = 0$ for $r \geq r_r(t)$, we expect $v(r_l(t),t)$ to be a global minima for velocity at any given time.

## 4.2 Self-Similar Blowup Limit

In our analysis thus far, we have concluded an implosion occurs by tracking the state of the inner radius $r_l(t)$. However, such analysis does not give insight on the structure of the solution in a neighborhood around $r_l(t)$. While to the left of $r_l(t)$ lies the Kidder solution, it is not clear how the solution to the right of $r_l(t)$ behaves. Given the blowup of the solution at $r_l(t)$, we search for *self-similar solutions of the first kind* that will serve as the asymptotic limit of the cutoff implosion solution. For self-similar solutions of the first kind, the similarity variable and exponents can be determined from dimensional analysis and invariant scalings of the problem. The self-similar solutions we will subsequently present are exact solutions in their similarity variables. However, we will observe that they also serve as asymptotic limits to the PDE solution close to implosion time.

This is in contrast to the 1D case, where there is an exact self-similar solution. We appeal to numerical simulations to justify why we do not expect a self-similar solution of the first kind be present in higher dimensions. Suppose to the contrary there exists an exact similarity solution with density $\tilde{\rho}$ with similarity variable $y$ on the interval $[r_l(t), r_r(t)]$ for $0 < t < 1$. Since $r_l(t)$ is monotone decreasing and $r_r(t)$ is monotone increasing, the interval $[r_l(t_1), r_r(t_1)]$ is contained in the interval $[r_l(t_2), r_r(t_2)]$ when $0 < t_1 < t_2 < 1$. If the exact similarity solution $\tilde{\rho}$ is continuous, then $\tilde{\rho}([r_l(t_1), r_r(t_1)]) \subset \tilde{\rho}([r_l(t_2), r_r(t_2)])$. However, in Figure 4.1 there exist values in the range of $\rho$ on $[r_l(t), r_r(t)]$ that appear in earlier times but not later times. In Subfigure 4.1a, the minimum of $\rho$ on $[r_l(t_1), r_r(t_1)]$ is less than 1. But, in Subfigure 4.1b, the minimum of $\rho$ on $[r_l(t_2), r_r(t_2)]$ is greater than 1. This contradicts the property that the image of $\tilde{\rho}$ on a subinterval should be contained in the image of $\tilde{\rho}$ on a larger interval. So, we do not seek self-similar solutions of the first kind to explain the solution on $[r_l(t), r_r(t)]$.

To derive the self-similar solution, we will first state the functional form in general and

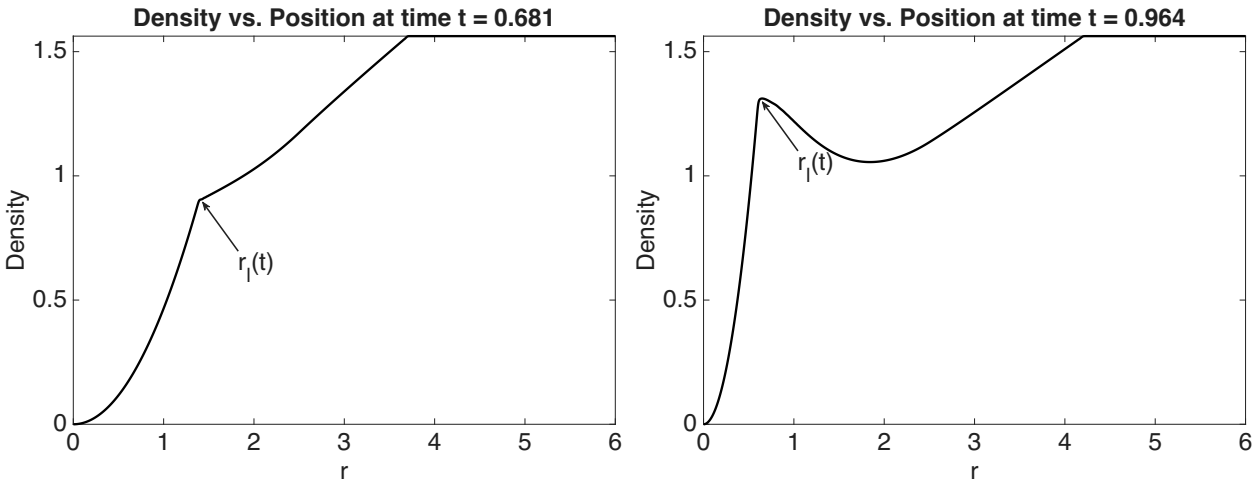


(a) Density at an earlier time $t_1$ where $\min_{r\in[r_l(t_1),r_r(t_1)]}\rho(r,t_1) < 1$.

(b) Density at a later time $t_2$ where $\min_{r\in[r_l(t_2),r_r(t_2)]}\rho(r,t_2) > 1$.

Figure 4.1: Snapshots of solutions to equations (2.19) and (2.20) from the cutoff implosion initial data (4.1) with parameters $n = 1$ and $r^* = 2.5$. The solution on the interval $[r_l(t), r_r(t)]$ cannot be an exact similarity solution since the image of the density on a subinterval must be contained in the image of any larger interval.

derive the corresponding system of ODEs. The system of ODEs can be further simplified using knowledge of the density and velocity at the inner radius derived in the previous section. Suppose we have a self-similar solution with similarity variable $y = \frac{r}{r_l(t)}$ and self-similar forms for the density and velocity

$$\rho(y,t) = \tau(t)\hat{\rho}(y), \quad v(y,t) = -\tau(t)^{\beta}\hat{v}(y) \tag{4.11}$$

where $\tau(t)$ is a function of time that goes to infinity as $t \to 1$ and $\beta$ is a to be determined exponent. The motivation behind considering the similarity variable $y$ is the time dependent length scale, $r_l(t)$, is derived from the left moving characteristic at $r^*$ at time $t = 0$ and acts as a principal length scale in the implosion. Additionally, $r_l(t)$ is asymptotically equivalent to the time scaling of the Kidder solution similarity variable close to implosion time.

The Kidder solution is invariant under this transformation, so it can be rewritten as

$$\begin{aligned} \rho(y,t) &= \tau(t)\hat{\rho}(y), \quad \hat{\rho}(y) = \hat{\rho}(1)y^{n+1}, \\ v(y,t) &= -\tau(t)^{\beta}\hat{v}(y), \quad \hat{v}(y) = \hat{v}(1)y, \\ \tau(t) &= \left(\frac{r_l}{1-t}\right)^{n+1}. \end{aligned} \tag{4.12}$$

Substituting the ansatzes in (4.11) into the potential flow equations (2.19) and (2.20) yields

$$\begin{cases} \tau_t\hat{\rho} - \tau\frac{y}{r_l}\dot{r}_l\hat{\rho}' - \frac{\tau^{\beta+1}}{r_l}\hat{\rho}'\hat{v} - \frac{\tau^{\beta+1}}{r_l}\hat{v}'\hat{\rho} - \frac{n\tau^{\beta+1}\hat{\rho}\hat{v}}{yr_l} & = 0, \\ -\beta\tau_t\tau^{\beta-1}\hat{v} + \tau^{\beta}\frac{y}{r_l}\dot{r}_l\hat{v}' + \frac{\tau^{2\beta}}{r_l}\hat{v}'\hat{v} + \gamma\frac{\tau^{\gamma-1}}{r_l}\hat{\rho}'\hat{\rho}^{\gamma-2} & = 0. \end{cases} \tag{4.13}$$

## 4.3 *A Priori* Reductions

To further simplify the ODE system in (4.13), we will use the knowledge of the implosion dynamics to explicitly determine the unknown terms. In doing so, we consider the implosion dynamics in the limit to implosion time and evaluate time-dependent, non $(1-t)$ terms at $t = 1$. This is justified since we wish to find the self-similar profile the solution to the PDE asymptotically approaches when $t$ is very close to $t = 1$. The resulting solution is a genuine self-similar solution with respect to the new variables and serves as an asymptotic limit.

### 4.3.1 Derivation of $\tau, \beta, \hat{\rho}(1), \hat{v}(1)$

From the definition of $y$, the spatial point $r = r_l(t)$ maps to $y = 1$. The exponent of $(1-t)$ in $r_l(t)$ can be expressed as $\frac{1}{s^*}$ where $s^* = \frac{2}{1+(n+1)^{-1/2}}$. Evaluating (4.12) at $y = 1$,

$$\tau(t)\hat{\rho}(1) = (1-t)^{\frac{(n+1)^{1/2}-(n+1)}{2}}(n+3)^{-\frac{n+1}{2}}k^{n+1},$$

where all of the non $(1-t)$ terms in (4.9) are evaluated at $t = 1$ and $k = r^*2^{\frac{-1-(n+1)^{-1/2}}{2}}$. A similar derivation in $v$ yields

$$-\tau(t)^{\beta}\hat{v}(1) = -(1-t)^{\frac{-1+(n+1)^{-1/2}}{2}}k.$$

Thus, $\tau(t)$ encodes the implosion dynamics and is

$$\tau(t) = (1-t)^{\frac{(n+1)^{1/2}-(n+1)}{2}} = r_l(t)^{-(n+1)(s^*-1)} \tag{4.14}$$

with $\beta = (n+1)^{-1}$. The initial condition at $y = 1$ for $\hat{\rho}$ and $\hat{v}$ is also identified as

$$\hat{\rho}(1) = (n+3)^{-(n+1)/2} k^{n+1}, \quad \hat{v}(1) = k. \tag{4.15}$$

### 4.3.2 Relation of $\dot{r}_l(t)$ to $\tau(t)$

Recall $r_l(t)$ satisfies the ODE (4.2). Substituting the ansatzes (4.11) into ODE (4.2), we obtain

$$\dot{r}_l(t) = -\tau^{\beta} \left( \hat{v}(1) + \left( \frac{n+3}{n+1} \right)^{\frac{1}{2}} \hat{\rho}(1)^{\frac{1}{n+1}} \right). \tag{4.16}$$

Equivalently, $\dot{r}_l(t) = -A\tau^{\beta}$, where $A$ is

$$A = k \left( 1 + (n+1)^{-\frac{1}{2}} \right) \tag{4.17}$$

after substituting in the initial conditions (4.15). Note $A$ is a positive constant.

### 4.3.3 Relation of $\tau_t(t)$ to $\tau^{\beta+1}(t)/r_l(t)$

By using the explicit forms of $\tau(t)$ and $r_l(t)$, we see $\tau(t)$ satisfies the ODE

$$\tau_t(t) = \lambda \frac{\tau^{\beta+1}(t)}{r_l(t)}, \tag{4.18}$$

where $\lambda$ is the constant

$$\lambda = k \left( (n+1) - (n+1)^{1/2} \right). \tag{4.19}$$

Note $\lambda$ is a positive constant.

## 4.4 Autonomous Transformation of the Self-Similar System

By using the *a priori* knowledge collected in the previous subsections, the ODE system (4.13) simplifies to

$$\begin{bmatrix} Ay - \hat{v} & -\hat{\rho} \\ \frac{n+3}{n+1} \hat{\rho}^{\frac{1-n}{1+n}} & \hat{v} - Ay \end{bmatrix} \begin{bmatrix} \hat{\rho}' \\ \hat{v}' \end{bmatrix} = \begin{bmatrix} \frac{n\hat{\rho}\hat{v}}{y} - \lambda\hat{\rho} \\ \beta\lambda\hat{v} \end{bmatrix}. \tag{4.20}$$

As done by Guderley [Gud42] (see [VS82, MRR22a, Sed59] for more details), consider the Emden transformation

$$\begin{aligned} \hat{\rho}(y) &= \left(\frac{n+1}{n+3}\right)^{\frac{(n+1)}{2}} y^{n+1}\sigma(x)^{n+1}, \\ \hat{v}(y) &= yw(x), \\ y &= e^x. \end{aligned} \tag{4.21}$$

In this change of variables, $\sigma$ is interpreted as the speed of sound. Under the Emden transformation, system (4.20) becomes

$$\begin{bmatrix} (A-w) & -\frac{1}{n+1}\sigma \\ (n+1)\sigma & (w-A) \end{bmatrix} \begin{bmatrix} \sigma' \\ w' \end{bmatrix} = \begin{bmatrix} -\frac{\lambda\sigma}{n+1} - A\sigma + 2w\sigma \\ \beta\lambda w + Aw - w^2 - (n+1)\sigma^2 \end{bmatrix}, \tag{4.22}$$

and can be formally written as

$$\begin{aligned} \begin{bmatrix} \sigma' \\ w' \end{bmatrix} = \left(\sigma^2 - (A-w)^2\right)^{-1} \begin{bmatrix} (w-A) & \frac{1}{n+1}\sigma \\ -(n+1)\sigma & (A-w) \end{bmatrix} \times \\ \begin{bmatrix} \frac{-\lambda\sigma}{n+1} - A\sigma + 2w\sigma \\ \beta\lambda w + Aw - w^2 - (n+1)\sigma^2 \end{bmatrix}. \end{aligned} \tag{4.23}$$

System (4.23) is recognized as the celebrated autonomous self-similar system featured in [Gud42] and [MRR22a] with our choice of parameters. The denominator $\Delta = (\sigma^2 - (A-w)^2)$ is the *sonic line* and is the determinant of the matrix $M(\sigma, w)$ of the left hand side of (4.22).

We seek solutions to system (4.23) moving forward from initial conditions

$$\sigma(0) = (n+1)^{-1/2}k, \quad w(0) = k, \quad P^* = \begin{bmatrix} \sigma(0) & w(0) \end{bmatrix}^T, \tag{4.24}$$

obtained by applying the Emden transformation to (4.15). We refer to $P^*$ as a *sonic point* as it is a fixed point lying on the sonic line. However, the initial condition (4.24) lies on the sonic line, implying singularity of system (4.23). Moreover, the Kidder solution, as written in the self-similar form (4.12), is mapped by the Emden transformation to the constant solution residing at (4.24). It is not obvious whether an additional solution to (4.23) exists. The following section presents an explanation on how additional solutions are constructed.

## 4.5 Non-Uniqueness of Solutions to the Self-Similar System

Denote $\vec{b}(\sigma, w)$ as the right hand side vector of (4.22) and take $M(\sigma, w)$ as the mass matrix defined earlier. Noting the anti-involutive structure of $M(\sigma, w)$ for any choice of $(\sigma, w)$ and the non-invertibility of $M(\sigma(0), w(0))$, we discuss the eigenvalues and eigenvectors of $M(\sigma(0), w(0))$.

**Lemma 4.5.1.** *Suppose a $2 \times 2$ real matrix $N$ has the entries*

$$N = \begin{bmatrix} a & b \\ c & -a \end{bmatrix}$$

*and $\det N = 0$. Then, $N$ has eigenvalue $\lambda = 0$ with only one associated eigenvector $\vec{v} = \begin{bmatrix} a & c \end{bmatrix}^T$.*

*Proof.* Suppose $N$ has $\det N = 0$, so $a^2 + bc = 0$. The eigenvalues $\lambda$ of $N$ satisfy the characteristic equation

$$\lambda^2 - a^2 - bc = 0,$$

but given $\det N = 0$, the only eigenvalue is $\lambda = 0$. Computing the eigenvectors for $\lambda = 0$ shows there is only one eigenvector, $\vec{v} = \begin{bmatrix} a & c \end{bmatrix}^T$. □

Since $M(\sigma(0), w(0))$ satisfies the conditions in Lemma 4.5.1, $M(\sigma(0), w(0))$ has only an eigenvalue at $\lambda = 0$ and only one corresponding eigenvector. When considering (4.22) as a matrix equation evaluated at (4.24), the vector on the right hand side $\vec{b}(\sigma(0), w(0))$ is the zero vector. Thus, valid initial slopes $\begin{bmatrix} \sigma'(0) & w'(0) \end{bmatrix}^T$ are rescaled eigenvectors of $M(\sigma(0), w(0))$, which take the form

$$\begin{bmatrix} \sigma'(0) \\ w'(0) \end{bmatrix} = \alpha \begin{bmatrix} A - w(0) \\ (n+1)\sigma(0) \end{bmatrix}, \tag{4.25}$$

where $\alpha$ is a scalar and the expression for the eigenvector is taken from Lemma 4.5.1.

We have thus established non-uniqueness of solutions to system (4.22) with initial condition (4.24) by also requiring an initial slope, which is not unique. For example, $\alpha = 0$ corresponds to the constant solution, which is also the Kidder solution in these variables.

We search for solutions with $\alpha < 0$ - solutions that decrease in magnitude with increasing $r$ in the original variables since we assume the density and velocity have extrema at $r_l(t)$ close to implosion time. Although condition (4.25) implies a one parameter family of solutions indexed by $\alpha$, in practice, we observe only one numerical solution for $\alpha$ sufficiently less than zero as the numerical ODE solver adapts its time stepping to the magnitude of $\alpha$.

## 4.6 Phase Portraits

We present phase portraits for the non-autonomous system and autonomous system in Figure 4.2 and Figure 4.3 respectively. The sonic line is also plotted in the phase portraits. In the non-autonomous system, the sonic line varies in $y$ and is plotted for various $y$. In the autonomous system, the sonic line is fixed. A region of the phase portrait is carved out by the sonic lines, denoted as the *sonic cone*. The nullclines are also plotted.

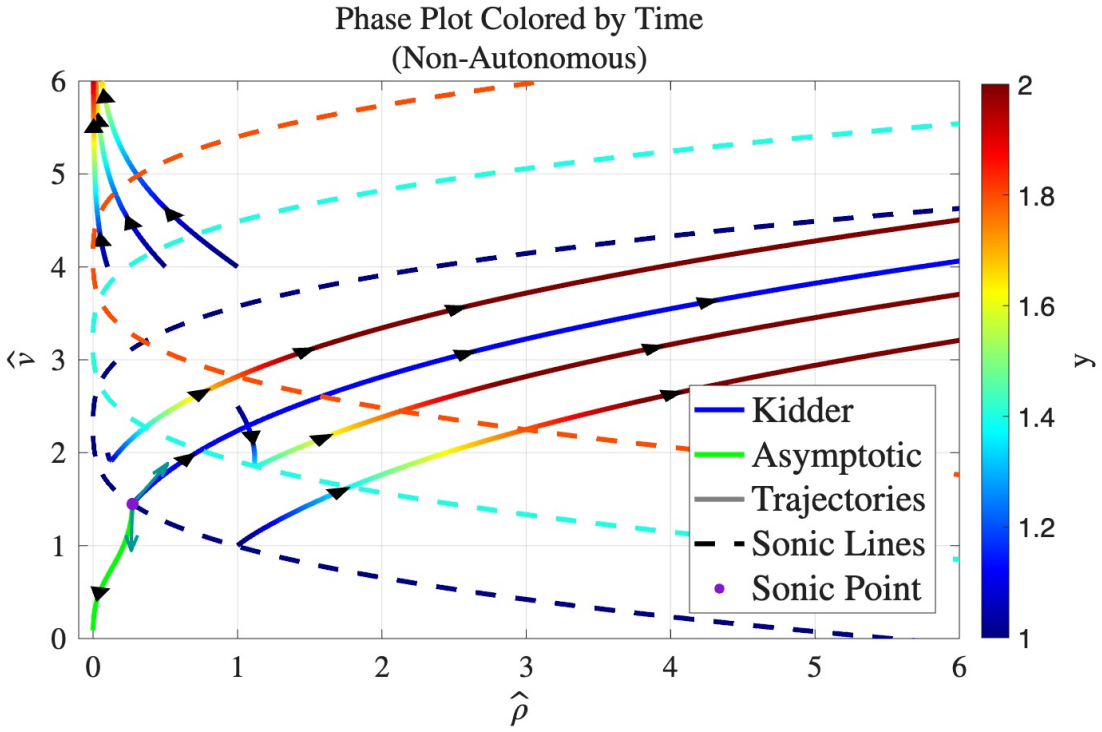


Figure 4.2: Phase portrait of non-autonomous system (4.20) for $n = 2$ and $r^* = 2.5$. The sonic line for various $y$ are displayed as dashed lines. Vectors indicating permissible initial slopes at the sonic point are drawn.

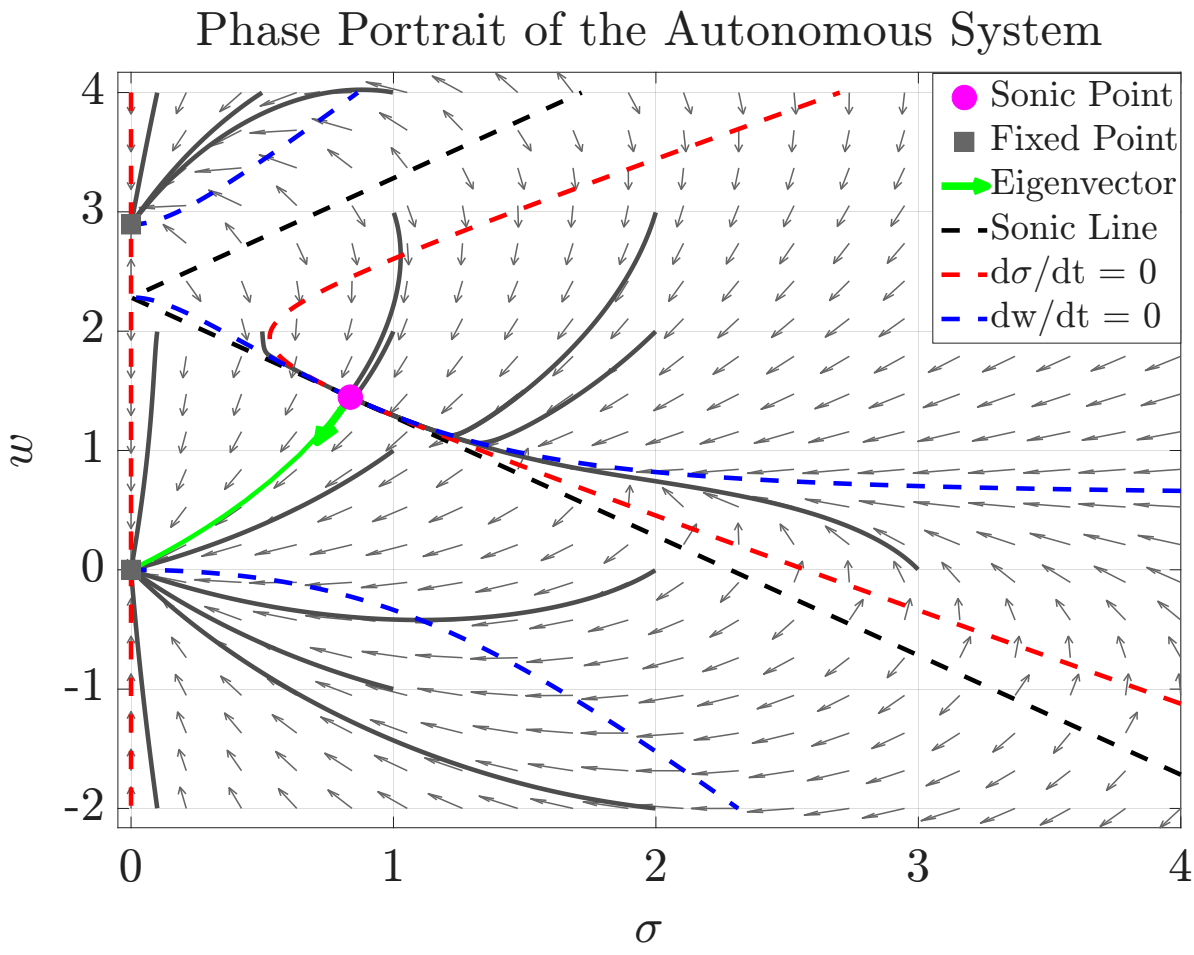


Figure 4.3: Phase portrait of autonomous system (4.22) for $n = 2$ and $r^* = 2.5$. The fixed points, nullclines, and sonic line are displayed. At the sonic point, the eigenvector (4.25) is shown indicating the only valid direction to leave the sonic point in the direction of the origin. The green curve represents the limiting self-similar profile to the right of $r_l(t)$ for the cutoff implosion solution near implosion time.

We first discuss features of the autonomous phase portrait of Subfigure 4.3. The fixed points are points such that $\sigma'$ and $w'$ are zero, which correlate with the $\sigma, w$ such that the right hand side of (4.22) is the zero vector. In the physically relevant regime of $\rho \geq 0$, there are three fixed points: the origin, $P^*$, and the point $P_1 = \begin{bmatrix} 0 & 2k \end{bmatrix}^T$. The origin and $P_1$ are both attractive fixed points which lie outside the sonic cone. On the other hand, $P^*$ lies on the sonic line itself. Trajectories starting inside the sonic cone cannot cross the sonic line, so they either must converge to $P^*$ or escape to infinity. From the phase portrait, we see

trajectories within the sonic cone approach $P^*$. Now for trajectories outside of the sonic cone near $P^*$, they move away from $P^*$ and converge to the attractive fixed point at the origin. We observe $P^*$ exhibits half-stability as it is attractive to trajectories in the sonic cone while it is repulsive to trajectories outside the sonic cone. Note both the origin and $P_1$ are true fixed points such that the only permissible slope passing through both fixed points are the zero vector, in contrast to $P^*$. Note despite both nullclines intersecting the sonic line at $\begin{bmatrix}0 & A\end{bmatrix}^T$ in Figure 4.3, this is not a fixed point. When system (4.22) is evaluated at $\begin{bmatrix}0 & A\end{bmatrix}^T$, the left hand side of (4.22) is the zero vector while the right hand side of (4.22) is $\begin{bmatrix}0 & \beta\lambda A\end{bmatrix}^T$, which is not the zero vector.

In the non-autonomous system, the sonic line is still a separatrix in the phase plane, but the sonic line varies with $y$. Trajectories beginning below the sonic line still approach the origin, like in the autonomous case. However, trajectories starting above the sonic line exhibit different behavior. Some approach infinity in $\hat{\rho}$ and $\hat{v}$ monotonically. The Kidder solution in non-autonomous coordinates does this. On the other hand, some trajectories begin to converge to the origin but deflects off the moving sonic line. After the deflection, the trajectory moves towards infinity. Another group of trajectories move towards $\hat{\rho} = 0, \hat{v} = \infty$, corresponding to the fixed point $P_1$ in autonomous coordinates.

The non-autonomous system (4.20) is shown to be the same as the one derived in [Gud42] and [MRR22a] up to rescaling in the specific case where $n$ and $\gamma$ are given by the relation $-2 = (n+1)(1-\gamma)$. Subsequently, the autonomous system given in (4.22) and (4.23) is a special case of the dynamical system [Gud42] and further explored by authors such as [VS82], [MRR22a], [SWW25]. Details on the equivalence is given in Appendix A.

The dynamical system in [Gud42] can be written in the form $w' = \frac{\Delta_1}{\Delta_2}$ and $\sigma' = \frac{\Delta_2}{\Delta}$ where $\Delta$ is the sonic line. Trajectories connecting endpoints on opposite sides of the sonic line must pass through the sonic line, but can only do so smoothly at *sonic points* where $\Delta = \Delta_1 = \Delta_2$. The only sonic points with non-vanishing density are $P_2$ and $P_3$. It is through sonic point $P_2$ which Merle. et al construct their smooth imploding profile [MRR22a]. They seek a solution that begins to the right of the sonic lines and terminates at the origin, which is to the left

of the sonic lines. Another important point is the fixed point that does not lie on the sonic line, $P_5$.

In the work of Merle et al. [MRR22a] and subsequent work such as Shao et al. [SWW25], they construct a sequence of smooth imploding solutions with blowup speeds $s_n < s^*$, where their similarity variable is defined as $y = r(T-t)^{1/s}$. Note the limiting value $s^*$ corresponds to the previously defined value of $s^*$ as the reciprocal $(1-t)$ exponent of $r_l(t)$ in (4.7). However, Merle et al. note their construction fails when $n = 2$ and $\gamma = \frac{5}{3}$ because as $s \to s^*$, the three points $P_2, P_3, P_5$ all coincide with each other. The work of Shao et al. specifically handles this degeneracy. For our system, the initial condition $P^*$ corresponds to this special coincidence. Solutions to (4.22) that arrive at the origin may be able to be viewed as the limiting profile to the sequence of smooth imploding solutions constructed in [SWW25].

## 4.7 Numerical Solutions of the ODE System

We directly compute numerical solutions of non-autonomous system (4.20) to determine the limiting self-similar profiles $\hat{\rho}$ and $\hat{v}$. Lemma 4.5.1 can be applied to (4.20) at initial condition (4.15) to show initial slopes belong to the affine space

$$V = \left\{ \begin{bmatrix} \mu \\ 0 \end{bmatrix} + \alpha \begin{bmatrix} n\hat{\rho}(1)\hat{v}(1) - \lambda\hat{\rho}(1) \\ \beta\lambda\hat{v}(1) \end{bmatrix}^T : \alpha \in \mathbb{R} \right\}, \tag{4.26}$$
$$\mu = k^{n+1}(n+3)^{-\frac{n+1}{2}} \left( (n+1) - (n+1)^{\frac{1}{2}} \right).$$

We use numerical method ODE23T in MATLAB to solve (4.20) at initial condition (4.15) and initial slope (4.26) with $\alpha = -3$ for $n = 1$ and $\alpha = -2$ for $n = 2$. The choice of $\alpha$ is determined heuristically to ensure the solutions decay to zero. We directly solve the system as an ODE with a mass matrix to avoid unnecessary matrix inversions and for ease of providing the initial slope. These solutions for 2D and 3D are shown in Figure 4.4. From the numerical solutions, we see $\hat{\rho}$ and $\hat{v}$ are monotone decreasing in $y$. Additionally, $\hat{v}$ (and equivalently $\sigma$) are positive for $y \geq 1$, which is behavior established for the profiles of [SWW25].

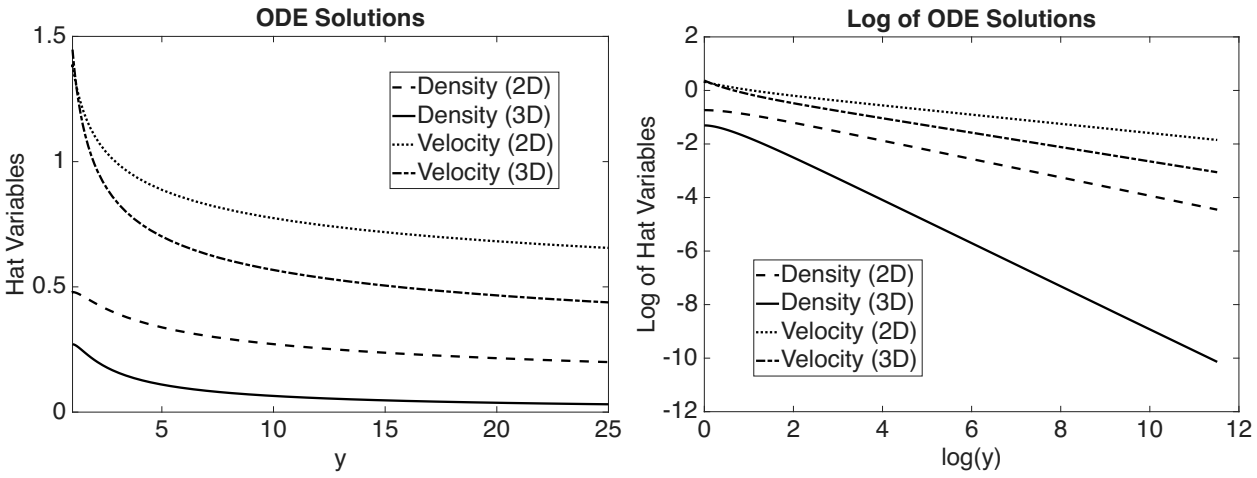


(a) Standard Variables

(b) Log-Log Scale

Figure 4.4: Solutions to ODE system (4.20) with initial condition (4.15) for 2D and 3D. The initial slope is chosen to be $\alpha = -3$ for $n = 1$ and $\alpha = -2$ for $n = 2$ in (4.26). The linear behavior of the numerical solutions in the log-log scale of Subfigure 4.4b indicate power law behavior of solutions in the far field. The computed slopes of the numerical solutions in log-log scale are displayed in Table 4.1.

## 4.8 Far Field Behavior of the Similarity Solution

From Subfigure 4.4b, we observe $\hat{\rho}$ and $\hat{v}$ appear linear in log-log scaling for large values of $y$, corresponding to the far field dynamics of $\hat{\rho}$ and $\hat{v}$. This implies a negative power law relationship between $y$ and $\hat{\rho}$ and $\hat{v}$ in this regime. By substituting an ansatz of the form $y^{-k_{\hat{\rho}}}$ and $y^{-k_{\hat{v}}}$ for the density and velocity respectively into (4.13), the terms originating from time derivatives dominate the terms originating from spatial derivatives and the source term. The exponents describing the far field power law behavior can be computed as

$$\hat{\rho}(y) \sim y^{-\lambda/A}, \quad \hat{v}(y) \sim y^{-\lambda/(\beta A)}, \quad -\frac{\lambda}{A} = (n+1)\frac{1-\sqrt{n+1}}{1+\sqrt{n+1}} = (n+1)(1-s^*). \tag{4.27}$$

The slopes of the numerical solutions of $\log(\hat{\rho})$ and $\log(\hat{v})$ for $y \geq 100$ are compared to the theoretical values in (4.27) in Table 4.1, showing excellent agreement between expected far field behavior and the numerical solution.

| Case | Numerical | Theoretical |
|---|---|---|
| Density (2D) | $-0.3431$ | $-0.3431$ |
| Density (3D) | $-0.8052$ | $-0.8038$ |
| Velocity (2D) | $-0.1717$ | $-0.1716$ |
| Velocity (3D) | $-0.2683$ | $-0.2679$ |

Table 4.1: Comparison between the slope of $\log y$ to numerically computed $\log \hat{\rho}$ and $\log \hat{v}$, shown in Subfigure 4.4b, to the theoretical power law scaling given in (4.27). The slope is numerically computed for $y \geq 100$.

## 4.9 Mass Concentration and $L^p_{\text{loc}}$ boundedness of the Similarity Solution

To better understand the physical properties of the proposed implosion, we want to determine whether the mass concentrates and forms a measure at implosion time. The result of [CW22] states that given initial data with a constant farfield density and finite initial energy with respect to the constant farfield, the solution will be bounded in $L^p_{\text{loc}}$ and mass concentration does not occur. The existence is given for $L^p_{\text{loc}}$ as the constant farfield density prevents existence in $L^p$ for all of space and to allow for implosions where a state variable approaches infinity. Because the result is stated in terms of finite relative energy, an exact $p$ is not stated but is implied to be at least $\gamma$ - stemming from the relative internal energy term. We show mass concentration does not occur for the cutoff implosion solution and give the maximal $p$ such that the density is bounded in $L^p_{\text{loc}}$ into the implosion time.

We study the $L^p$ mass on the interval $[0, R]$ where $R << r_r(t)$ as $t \to 1$. Given a radial density distribution, the $L^p$ norm or $L^p$ mass of $\rho$ on an interval $[a, b]$ is given by

$$\|\rho(r,t)\|_{L^p([a,b])} = \left( \int_a^b s(n) r^n \rho(r,t)^p dr \right)^{\frac{1}{p}}, \tag{4.28}$$

where $s(n)$ is a the surface area of the $n+1$-dimensional unit ball. To evaluate the $L^p$ norm on the interval $[0, R]$, the interval may be split into two sub-intervals: $[0, r_l(t)]$ and $[r_l(t), R]$.

On the interval $[0, r_l(t)]$, given the density is the Kidder solution, the $L^p$ norm is

$$\begin{aligned}\|\rho(r,t)\|_{L^p([0,r_l(t)])} = &\left( s(n) \left( \frac{1}{n+3} \right)^{(n+1)/2} \frac{1}{2n+2} (r^*)^{2n+2} \right)^{\frac{1}{p}} \\ &\times (1-t)^{\frac{(n+1)(p+1)}{2} + \frac{(n+1)^{1/2}(p+1)}{2} - (n+1)p} \\ &\times (1+t)^{\frac{(n+1)(p+1)}{2} - \frac{(n+1)^{1/2}(p+1)}{2} - (n+1)p}.\end{aligned} \tag{4.29}$$

To determine whether the $L^p$ norm blows up as $t \to 1$, the exponent of $(1-t)$ must be nonnegative, which occurs when

$$p \leq p_{\text{crit}} = \frac{(n+1)^{1/2} + 1}{(n+1)^{1/2} - 1} \tag{4.30}$$

when $n > 0$. Note $p_{\text{crit}}$ may be expressed as other quantities as well as $p_{\text{crit}} = (n+1)(A/\lambda) = ((n+1)(s^* - 1))^{-1}$. It is always true $1 \leq \gamma \leq p_{\text{crit}}$ for $n > 0$, establishing the bound of $\rho(r,t)$ in the $L^\gamma_{\text{loc}}$ norm. Note $\lim_{n\to\infty} p_{\text{crit}} = 1$, implying as the spatial dimension increases, the maximal $L^p$ existence of $\rho(r,t)$ decreases. However, for any finite $n$, the $L^1_{\text{loc}}$ norm is always finite.

The mass in the region $[0, r_l(t)]$ (corresponding to $p = 1$) is

$$\begin{aligned}\|\rho(r,t)\|_{L^1([0,r_l(t)])} = s(n) &\left( \frac{1}{n+3} \right)^{(n+1)/2} \frac{1}{2n+2} (r^*)^{2n+2} \times \\ &(1-t)^{(n+1)^{1/2}} (1+t)^{-(n+1)^{1/2}}.\end{aligned} \tag{4.31}$$

To evaluate the integral on the remaining sub-interval, we change variables to $y = \frac{r}{r_l(t)}$ and also write $\rho(r,t)$ in terms of the self-similar form (4.11). We further subdivide the interval to $[1, a]$ and $\left[a, \frac{R}{r_l(t)}\right]$, where $[1, a]$ represents the non-power law behavior of $\hat{\rho}(y)$ while $\hat{\rho}(y)$ is taken to be the power law described in (4.27) on $\left[a, \frac{R}{r_l(t)}\right]$, motivated by Subfigure 4.4b. The integral decomposes into

$$s(n) r_l(t)^{n+1} \tau(t)^p \int_1^a \hat{\rho}(y)^p y^n dy \tag{4.32}$$

and

$$s(n) r_l(t)^{n+1} \tau(t)^p \int_a^{\frac{R}{r_l(t)}} C y^{-\frac{p\lambda}{A}} y^n dy. \tag{4.33}$$

The integral of (4.32) is finite as we observe $\hat{\rho}$ is monotone decreasing and $\hat{\rho}(1)$ is finite. Blowup depends only on the $r_l(t)^{n+1}\tau(t)^p$ term. Recalling $r_l(t) \to 0$ and $\tau(t) \to \infty$ as $t \to 1$, we find blowup does not occur as long as $p \leq p_{\text{crit}}$ - the same condition for the Kidder solution. The integral of (4.33) evaluates to

$$\frac{s(n)}{n+1-p\frac{\lambda}{A}} \left(\tau(t) r_l(t)^{\frac{\lambda}{A}}\right)^p \left(R^{n+1-\frac{p\lambda}{A}} - a^{n+1-\frac{p\lambda}{A}}\right)$$

after substituting the power law given in (4.27). Potential blowup is independent of $p$, and recognizing that $\frac{A}{\lambda} = \frac{p_{\text{crit}}}{n+1}$, the time dependent term cancels out. Assuming $p < p_{\text{crit}}$, only the integral (4.33) contributes to the $L^p_{[0,R]}$ norm of $\rho$. Additionally, the power law dependence of $\|\rho(r,t)\|_{L^p([0,R])}$ on $R$ as $t \to 1$ is given by

$$R^{\frac{n+1}{p}-\frac{\lambda}{A}}. \tag{4.34}$$

From this calculation, we find the maximal $p$ such that $\rho(r,t)$ is bounded in $L^p_{\text{loc}}$ into the implosion, given by $p_{\text{crit}}$. Blowup of the $L^p$ norm depends only on the blowup of the $L^p$ norm of the Kidder solution on $[0, r_l(t)]$ and not the self-similar solution past $r_l(t)$. Since $p_{\text{crit}} > 1$, mass concentration cannot form around the origin as predicted by the result of [CW22].

## 4.10 Numerical Evidence of Self-Similar Blowup for the PDE

We support the analysis done in the previous sections with numerical simulations. Our goal is to verify the formulas for the inner and outer radii along with the imploding density and velocity at the inner radius. Once the simulation progresses close to implosion time, we determine whether the solution approaches a self-similar asymptotic limit. Additionally, we verify the numerical solution satisfies the predicted time-scaling behavior. Finally, the $L^p$ norm of density for various $p$ is computed from the numerical solutions.

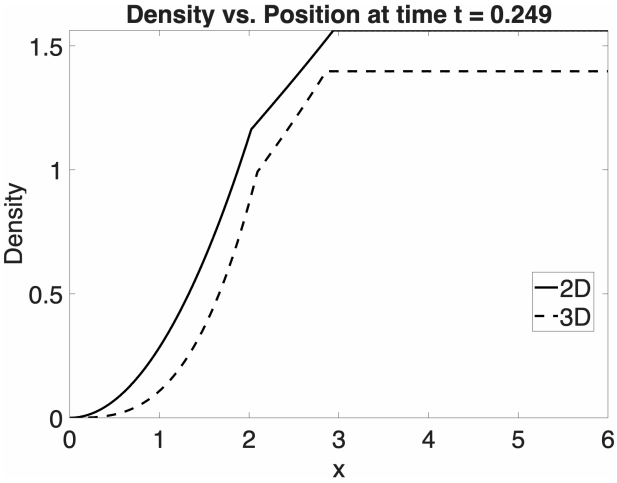


(a) $t \approx 0.25$

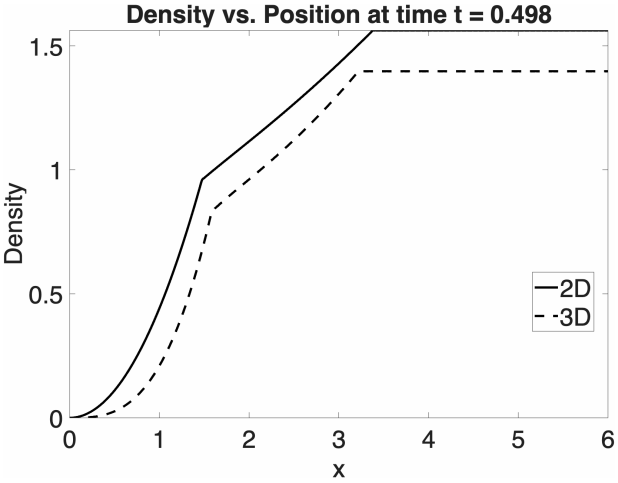


(b) $t \approx 0.5$

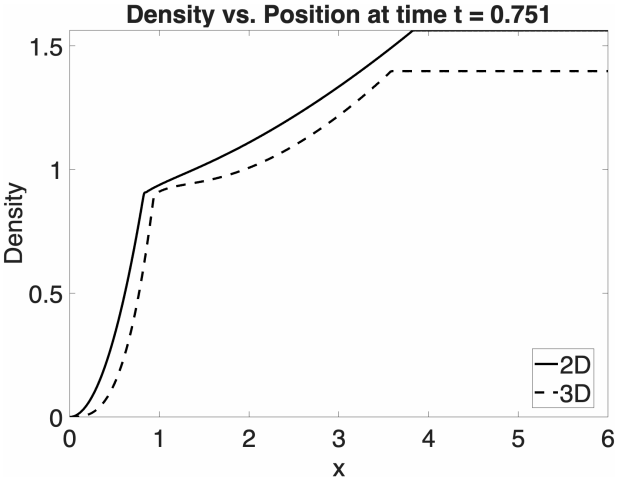


(c) $t \approx 0.75$

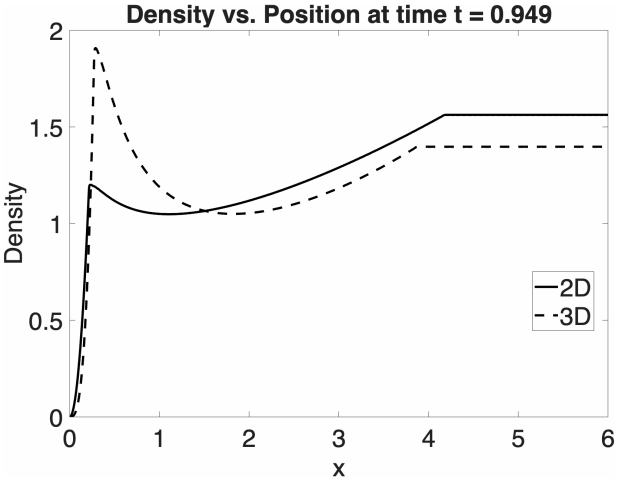


(d) $t \approx 0.95$

Figure 4.5: Computed density to the potential flow equations (2.19) and (2.20) with cutoff implosion initial data (4.1) and $r^* = 2.5$. Approximate times $t = 0.25$, 0.5, 0.75 and $t = 0.95$ in 2D (solid) and 3D (dashed) illustrating the evolution of the solution are displayed.

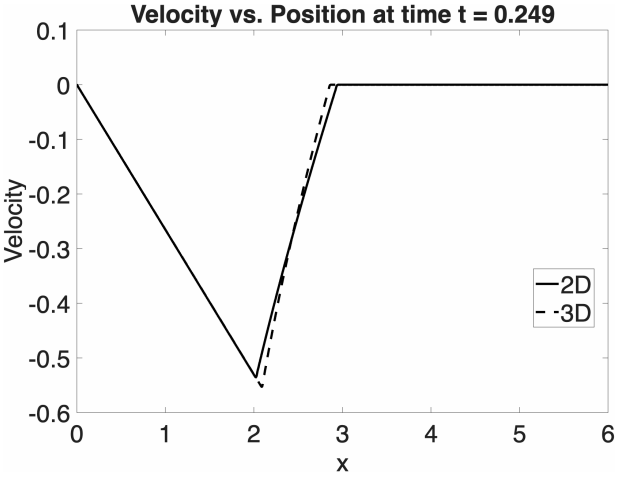


(a) $t \approx 0.25$

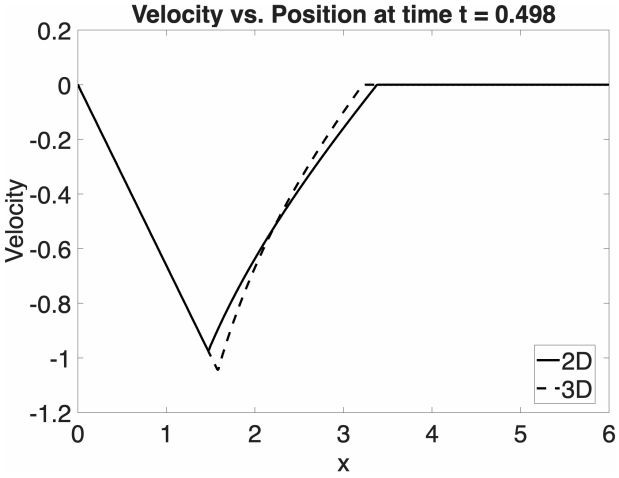


(b) $t \approx 0.5$

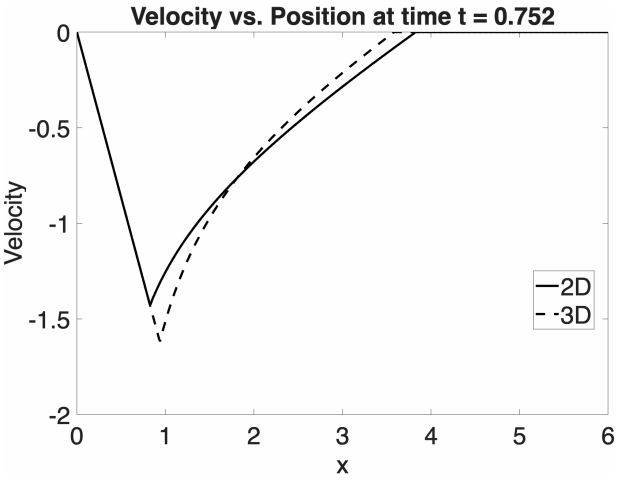


(c) $t \approx 0.75$

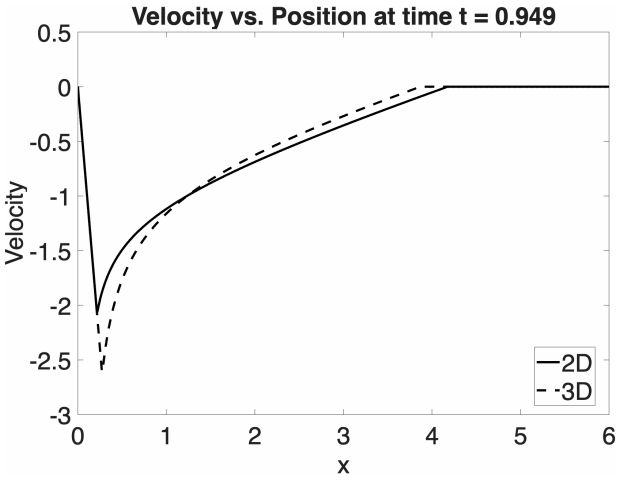


(d) $t \approx 0.95$

Figure 4.6: Computed velocity to the potential flow equations (2.19) and (2.20) with cutoff implosion initial data (4.1) and $r^* = 2.5$. Approximate times $t = 0.25$, 0.5, 0.75 and $t = 0.95$ in 2D (solid) and 3D (dashed) illustrating the evolution of the solution are displayed.

### 4.10.1 Lagrangian Leapfrog

The numerical simulation of the potential flow equations (2.19) and (2.20) is performed with a Lagrangian leapfrog scheme as introduced in [NR50] and further refined in [Noh87]. In this Lagrangian scheme, cells are defined on the intervals between nodes. The nodes are interspersed throughout the spatial domain and kinematic variables like position and

velocity are defined on these nodes. The numerical scheme tracks the evolution of the cells by advecting the nodes. Thermodynamic variables such as the density and pressure are defined to each cell. Historically, this scheme was introduced to better resolve shocks via artificial viscosity as elaborated in [NR50] and [Noh87]. We do not predict any shocks in our analysis, so we set the artificial viscosity to zero.

### 4.10.2 Adaptive Mesh Refinement

As the simulation approaches implosion time, we perform an adaptive mesh refinement near the implosion point $r_l(t)$ to capture the self-similar profile without losing resolution. Without adaptive mesh refinement, the interval $[0, r_l(t)]$ will shrink in time, and the number of cells within this region will decrease as well. We use a simple criteria and procedure: whenever $r_l(t)$ decreases by a set factor, we increase the amount of nodes in between the origin and $r_l(t)$.

Adaptive mesh refinement allows for high resolution of the implosion with only logarithmic scaling in the number of nodes. When adaptive mesh refinement occurs, only the interval the Kidder solution is supported on receives additional resolution. Although our goal is to resolve the structure to the right of $r_l(t)$, increasing resolution between the origin and $r_l(t)$ still accomplishes this because every particle originating in $(0, r^*)$ will eventually fall to the right of $r_l(t)$ at the time prescribed in (4.8).

By choosing to add nodes on the interval $(0, r_l(t))$ corresponding to the Kidder solution, we assign density and velocity values to all nodes on this interval such that they match the Kidder solution. We choose this to leverage the fact we have knowledge of the closed form solution on this region. Ultimately, the goal of the adaptive mesh refinement is to provide better resolution to understand the details of the numerical simulation to the right of $r_l(t)$. We do not directly alter this region of the solution with *a priori* knowledge, justifying the approach.

Adaptive mesh refinement begins after $\rho(r_l(t), t)$ starts to increase in time. Given $v(r_l(t), t)$ is expected to be a global minimum for velocity in space, we track $r_l(t)$ in the numerical

simulation as $r_l(t) = \arg\min_r v(r,t)$. It is vital to design a way of identifying $r_l(t)$ without using simulation time as the accumulated small errors in time steps become large deviations in time very close to implosion time. A detailed description of the implementation of the Lagrangian leapfrog numerical scheme and adaptive mesh refinement can be found in Chapter 5.

### 4.10.3 Simulation Parameters

We simulate the potential flow equations (2.19) and (2.20) with initial condition (4.1) for both $n = 1$ and $n = 2$, corresponding to cylindrical and spherical symmetric geometry respectively. The numerical domain is $[0, 5]$ with initially 3001 nodes and 3000 cells. Instead of halting the simulation at a set time, we end the simulation once the maximum density has achieved a set value: $10^5$ for $n = 1$ and $10^{10}$ for $n = 2$. The boundary condition of our simulations are $v = 0$ at $r = 0$ and $v = 0$ at $r = 5$, with the right boundary condition justified as the gas has constant density and zero velocity in this region left unperturbed. We select the cutoff position in the initial data to be $r^* = 2.5$. Adaptive mesh refinement begins when $\rho(r_l(t), t)$ starts to increase in time. Empirically, we find this to be around $t = 0.9$ and start adaptive mesh refinement after $t = 0.9$. Successive refinement occurs whenever $r_l(t)$ decreases by a factor of three, and the mesh is refined by splitting every cell in between $[0, r_l(t)]$ into two new cells.

Figures 4.5 and 4.6 show the evolution of the density and velocity respectively at various times up until $t = 0.95$ to give a general sense of how the solution evolves at times far from $t = 1$. The percent error between predicted values at $r_l(t)$ and computed values at times leading up to $t = 0.9$, before adaptive mesh refinement occurs, is displayed in Table 4.2. To better understand the solution behavior near $t = 1$, Figures 4.8 and 4.9 show the density and velocity profiles in the similarity variable $y$ near the blowup in 2D and 3D respectively. The time-scaling between $r_l(t)$ and extrema of the density and velocity is shown in Figure 4.10. The $L^p$ norm on $[0, r]$ for various choices of $p$ are displayed in Figures 4.11, 4.12, 4.14, and 4.13.

### 4.10.4 Early Time Dynamics

| Feature | Min | Max | Mean |
|---|---|---|---|
| $r_l(t)$ (2D) | $-0.24\%$ | $0.50\%$ | $0.08\%$ |
| $r_l(t)$ (3D) | $-0.24\%$ | $0.10\%$ | $-0.05\%$ |
| $\rho(r_l(t),t)$ (2D) | $-0.47\%$ | $0.05\%$ | $-0.13\%$ |
| $\rho(r_l(t),t)$ (3D) | $-0.89\%$ | $-0.16\%$ | $-0.41\%$ |
| $v(r_l(t),t)$ (2D) | $-0.46\%$ | $-0.06\%$ | $-0.28\%$ |
| $v(r_l(t),t)$ (3D) | $-0.62\%$ | $-0.06\%$ | $-0.35\%$ |
| $m(0,r_l(t))$ (2D) | $-0.94\%$ | $2.2\%$ | $0.39\%$ |
| $m(0,r_l(t))$ (3D) | $-1.40\%$ | $0.84\%$ | $-0.19\%$ |

Table 4.2: Percent error between the analytical and computed $r_l(t), \rho(r_l(t),t), v(r_l(t),t)$ and $m(0,r_l(t))$ from $t \in (0, 0.9]$. The percent error formula is $\%\ \text{Error}_x = 100 \times \frac{x_{\text{comp}} - x_{\text{pred}}}{x_{\text{pred}}}$ where $x_{\text{comp}}$ is the computed value and $x_{\text{pred}}$ is the predicted value. The minimum, maximum, and mean percent errors are displayed.

We compare our analytical expressions for $r_l(t)$ (4.7), $\rho(r_l(t),t)$ (4.9), $v(r_l(t),t)$ (4.10), and $\|\rho(r,t)\|_{L^1([0,r_l(t)])}$ (4.28) to numerical data on times far away from the implosion time. These comparisons are made before adaptive mesh refinement is done in order to verify our predictions before assumptions on the solution are made in the numerical scheme. The percent errors on all of these quantities, displayed in Table 4.2, are low and bounded in a 2.5% range. The notable outlier is the mass in the implosion region, which has a slightly higher percent error range than the other quantities. We interpret this as the result of the mass in the imploding region being a quantity that is computed from the directly simulated variables of $\rho$ and $r_l(t)$. The directly simulated variables $\rho, v$, and $r_l(t)$ all enjoy much lower percent error, being bounded by 1% error. The low percent error indicates the expressions for $r_l(t), \rho(r_l(t),t), v(r_l(t),t)$, and $m(0,r_l(t))$ are correct.

Additionally, we compute the percent $L^1$ error, in space between the Kidder solution and

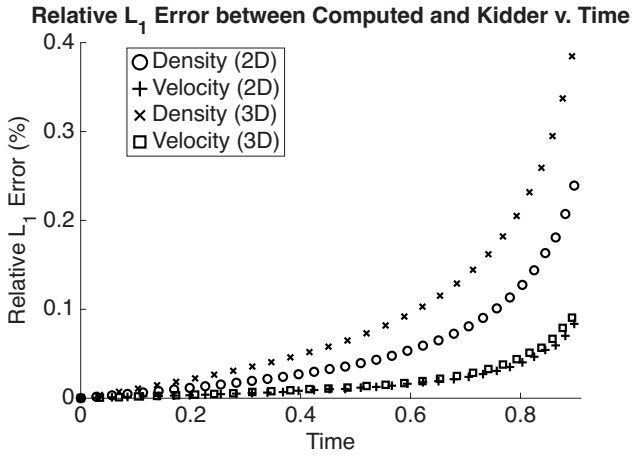


Figure 4.7: Percent $L^1$ error between the Kidder solution (2.39) computed by (4.35) and the computed solution, taken on the interval $[0, r_l(t)]$ for $0 < t \leq 0.9$.

the computed solution on the interval $[0, r_l(t)]$. The percent $L^1$ error is computed as

$$\% \text{ Error} = 100 \times \frac{\left\| y^A - y^C \right\|_1}{\left\| y^A \right\|_1} = 100 \times \frac{\frac{1}{V} \sum_{i=1}^{N} \left| y^A(x_i) - y_i^C \right| V_i}{\frac{1}{V} \sum_{i=1}^{N} \left| y_i^A \right| V_i}, \tag{4.35}$$

where the $A$ and $C$ superscripts represent the analytical and computed solutions respectively, $N$ is the number of nodes or volumes, $x_i$ is the location of the $i$th node or volume, $V_i$ is the cell volume, and $V$ is the sum of the cell volumes. In Figure 4.7, the $L_1$ error between the Kidder solution and computed solution is displayed for density and velocity in 2D and 3D. We observe from Figure 4.7 the $L_1$ error monotonically increases as time progresses. It is expected for errors to accumulate in time as the simulation progresses. Despite the increasing time, the percent $L_1$ errors are bounded by 0.5%. Both the low percent error of features presented in Table 4.2 and the low percent $L_1$ error between the Kidder solution and computed solution justify the hypothesis the solution remains the Kidder solution on the interval $[0, r_l(t)]$. As such, this justifies our adaptive mesh refinement as the simulation progresses to implosion time.

The adaptive mesh refinement allows the numerical scheme to simulate times close to $t = 1$ corresponding to large values of $\rho(r_l(t))$. In the close to implosion regime, we predict the solution should adhere to the dynamics of the ODE system in (4.20). By plotting the numerical data with respect to the similarity variable and normalizing the quantities, we see

in Figures 4.8 and 4.9 for 2D and 3D respectively. Note the plotted velocity is normalized by $\min_y v(y) < 0$ to be positive. In all of the comparison plots, the data coincides with each other on the interval $y = [0, 1]$ and in the log-log scale as the numerical solution is the Kidder solution on this interval. The displayed times are computed from the maximum density in the simulation and (4.9).

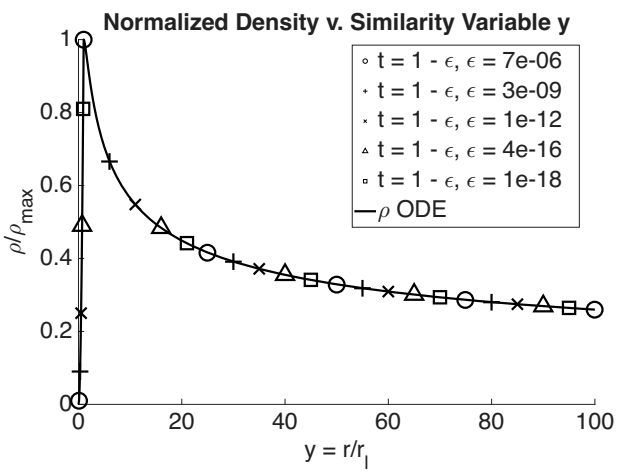


(a)

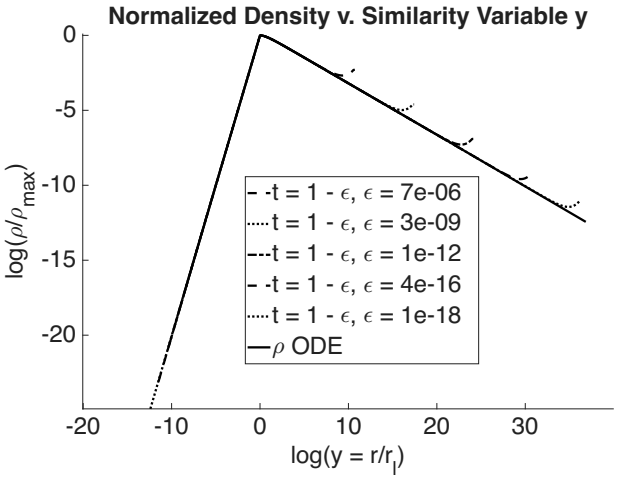


(b)

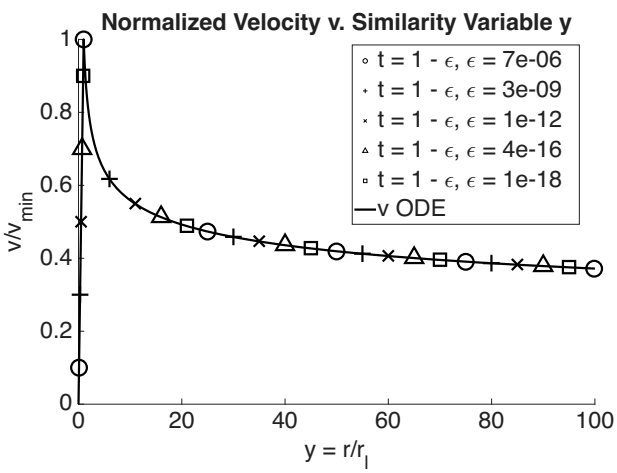


(c)

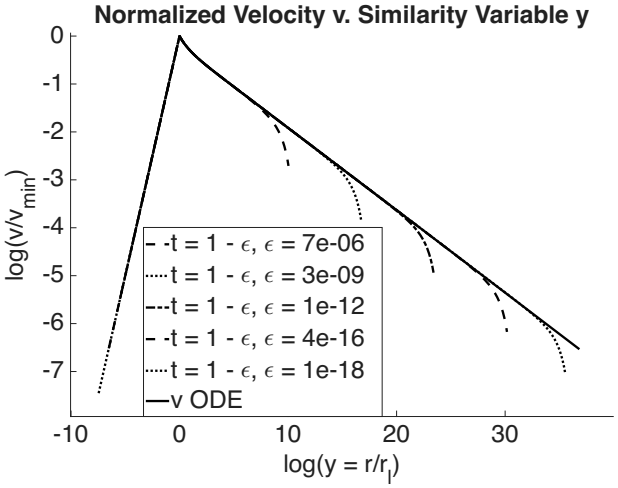


(d)

Figure 4.8: Blowup profiles in 2D with respect to the similarity variable $y = \frac{r}{r_l(t)}$ near $t = 1$ for density in subfigures 4.8a and for velocity in 4.8c and in a log-log scale in subfigures 4.8b for density and 4.8d for velocity. The profiles are compared to $\hat{\rho}$ and $\hat{v}$ solving ODE system (4.20). The selected times represent the solution at $\max \rho(r,t) = 10$, $10^2$, $10^3$, $10^4$, and $10^5$ respectively.

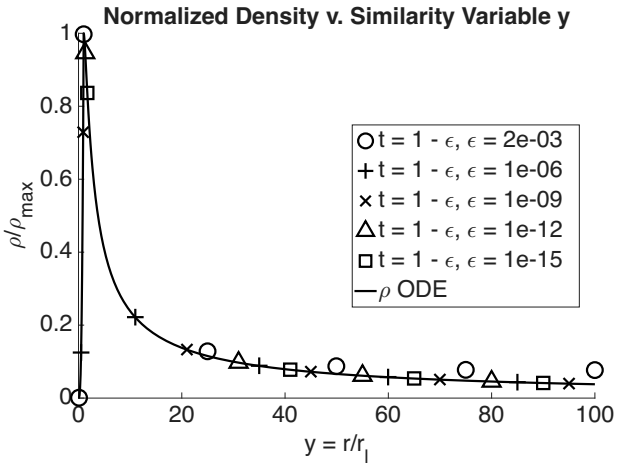


(a)

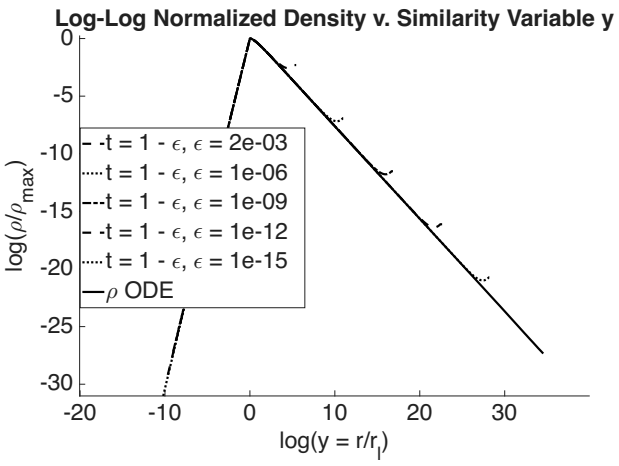


(b)

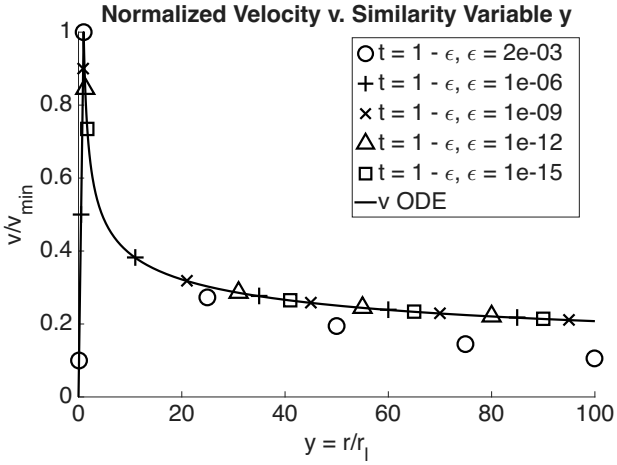


(c)

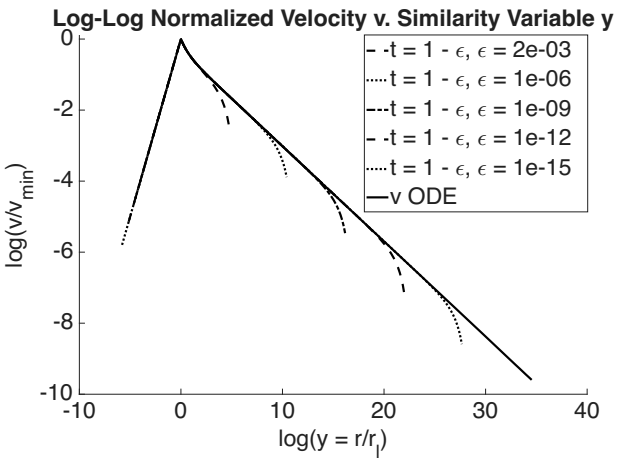


(d)

Figure 4.9: Blowup profiles in 3D with respect to the similarity variable $y = \frac{r}{r_l(t)}$ near $t = 1$ for density in subfigures 4.9a and for velocity in 4.9c and in a log-log scale in subfigures 4.9b and 4.9d. The profiles are compared to $\hat{\rho}$ and $\hat{v}$ solving ODE system (4.20). The selected times represent the solution at $\max \rho(r,t) = 10$ ,$10^3$, $10^5$, $10^7$, and $10^9$ respectively.

Subfigures 4.8a and 4.9a show how the data coincides with $\hat{\rho}$ when plotted against $y$ for density and similarly for $\hat{v}$ in 4.8c and 4.9c. The agreement is quantified in Table 4.3 where the percent $L^1$ error between computed and normalized density and velocity are compared to $\hat{\rho}$ and $\hat{v}$ which solve ODE system (4.20). The percent $L^1$ error is less than a percent for both density and velocity for all times. Furthermore, as time gets closer to implosion time, the

| $n$ | $\max \rho(r,t)$ | % Density Error | % Velocity Error |
|---|---|---|---|
| 1 | $10^1$ | 0.43% | 0.17% |
| 1 | $10^2$ | 0.35% | 0.11% |
| 1 | $10^3$ | 0.30% | 0.09% |
| 1 | $10^4$ | 0.27% | 0.07% |
| 1 | $10^5$ | 0.26% | 0.06% |
| 2 | $10^1$ | 0.98% | 0.31% |
| 2 | $10^3$ | 0.12% | 0.18% |
| 2 | $10^5$ | 0.08% | 0.13% |
| 2 | $10^7$ | 0.06% | 0.11% |
| 2 | $10^9$ | 0.05% | 0.12% |

Table 4.3: Percent $L^1$ error (4.35) between computed $\rho$ and $v$ near implosion time to self-similar profiles $\hat{\rho}$ and $\hat{v}$. The self-similar profiles $\hat{\rho}$ and $\hat{v}$ are solutions to (4.20) and are shown in Figure 4.4. Percent error is computed with respect to the similarity variable $y$. The interval of consideration is $r_l(t) \leq r \leq 5r_l(t)$ or equivalently $1 \leq y \leq 5$.

percent $L^1$ error decreases indicating convergence of numerical data to the $\hat{\rho}$ and $\hat{v}$ profiles. The higher percent $L^1$ errors in density and velocity in the case of $n = 2$, $\max \rho(r,t) = 10$ relative to the other errors indicate the solution is still far away from the asymptotic limit. Given the profiles $\hat{\rho}$ and $\hat{v}$ only explain the solution dynamics near $r_l(t)$, we do not expect the numerically computed solutions to adhere to $\hat{\rho}$ and $\hat{v}$ for all $y$ and especially for $y$ corresponding to $r = r_r(t)$. This also justifies the choice of interval to compute the percent $L^1$ error to be a small neighborhood around $r_l(t)$: $[r_l(t), 5r_l(t)]$.

The adherence and departure from $\hat{\rho}$ and $\hat{v}$ is further seen in the log-log plots for density in subfigures 4.8b and 4.9b and velocity in subfigures 4.8d and 4.9d. In the log-log plots, the data adheres to $\hat{\rho}$ and $\hat{v}$ up until some $y$, at which it peels off from the profile. The departure from the profile indicates the data entering the region sufficiently far away from $r = r_l(t)$. The accurate prediction $\hat{\rho}$ and $\hat{v}$ provide compared to numerical simulations close to the predicted implosion time gives numerical evidence that $\hat{\rho}$ and $\hat{v}$ are the asymptotic

limit of the solution up to implosion time.

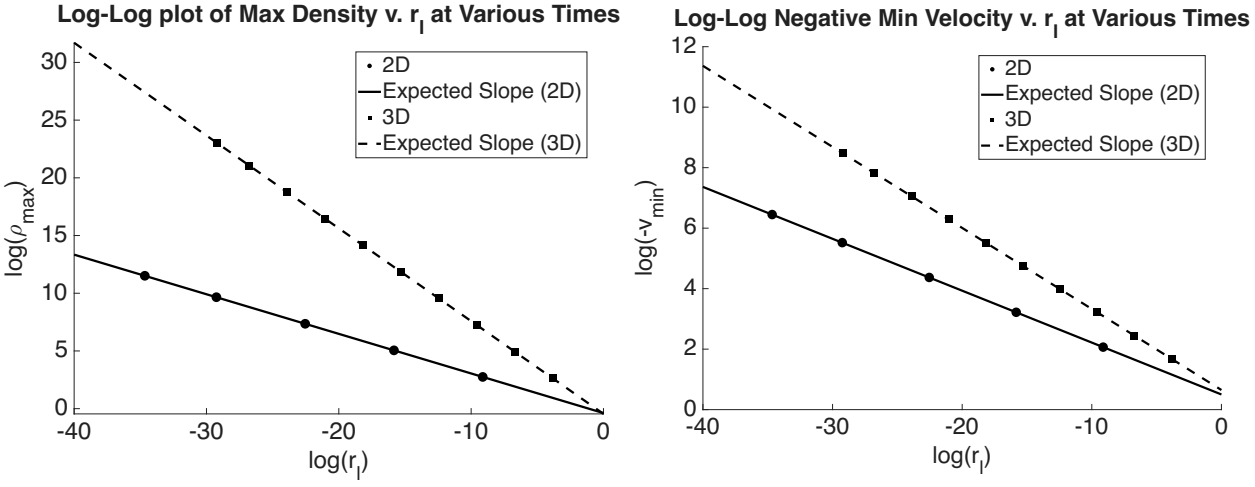


(a) Density

(b) Velocity

Figure 4.10: Log-log plots of maximum density and negative minimum velocity with respect to $r_l(t)$ at various times. The expected power law relationship (4.14) between $r_l$ and density and velocity is plotted and represented as a line. The data points fit exactly onto the line, verifying the expected power law relationship.

To verify whether the numerical simulation accurately captures the time-scaling behavior, we check whether the numerical simulation correctly evolves $\tau(t)$ near implosion time. We check this by determining the evolution of the maximum and negative minimum of density and velocity respectively against $r_l(t)$ using the relationship between $\tau(t)$ and $r_l(t)$ given in (4.14). The extrema values of the density and velocity serve as a representation of $\tau(t)$ from the data. We compute $r_l(t)$ from the data by $r_l(t) = \arg\min_r v(r,t)$. Log-log plots of the extrema versus $r_l(t)$ are given in Figure 4.10, with density in Subfigure 4.10a and velocity in Subfigure 4.10b. The expected power law behavior between $r_l(t)$ and $\tau(t)$ from (4.14) is also plotted. We see for both the density and velocity in 2D and 3D the extrema value match directly onto the theoretical power law, verifying the numerical simulation accurately captures the scaling dynamics between $r_l(t)$ and $\tau(t)$.

### 4.10.5 Blowup in $L^p$ Norms

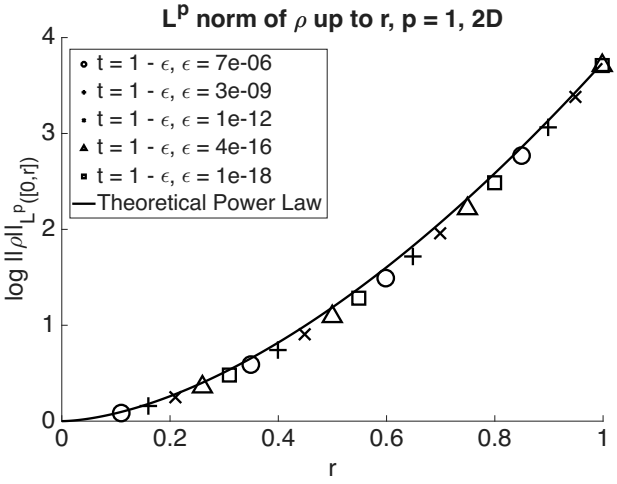


(a) Mass in 2D

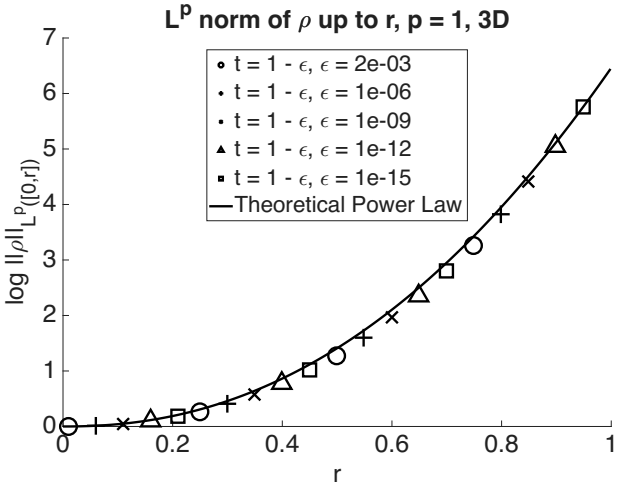


(b) Mass in 3D

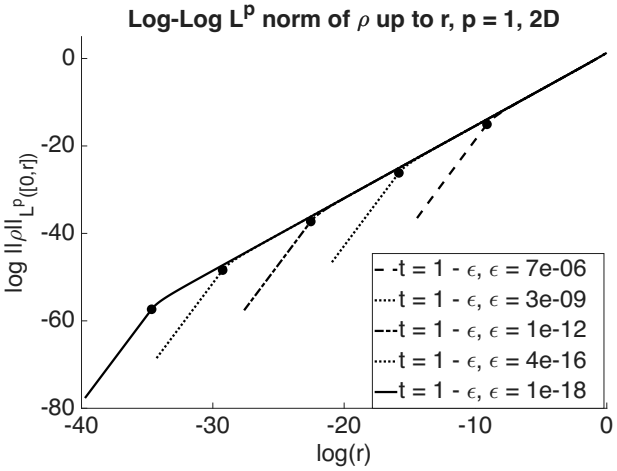


(c) Log Mass in 2D

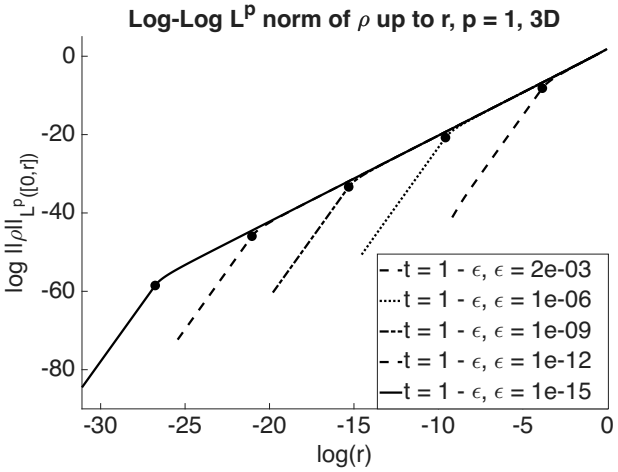


(d) Log Mass in 3D

Figure 4.11: The $L^1$ norm of $\rho$ on $[0, r]$ for 2D and 3D. Subfigures 4.11a and 4.11b show the radial dependence on mass while subfigures 4.11c and 4.11d are in log-log scale. The selected times are the same as in Figures 4.8 and 4.9. A power law curve is plotted in Subfigures 4.11a and 4.11b whose exponent is given by (4.34). The constant is fitted from the numerical data. Black dots are plotted in Subfigures 4.11c and 4.11d representing $r_l(t)$ at various times.

| Dimension | $p$ | Numerical | Theoretical |
|---|---|---|---|
| 2 | 1 | 1.6651 | 1.6569 |
| 2 | $\gamma$ | 0.6654 | 0.6569 |
| 3 | 1 | 2.2070 | 2.1962 |
| 3 | $\gamma$ | 1.0087 | 0.9962 |

Table 4.4: Comparison between the slope of numerically computed $\log \|\rho(r,t)\|_{L^p([0,r])}$ against $\log r$, shown in Subfigures 4.11c, 4.11d, 4.12a, and 4.12b for various $p < p_{\text{crit}}$, to the theoretical power law scaling given in (4.34). The slope is numerically computed for $2r_l(t) \leq r \leq 1$.

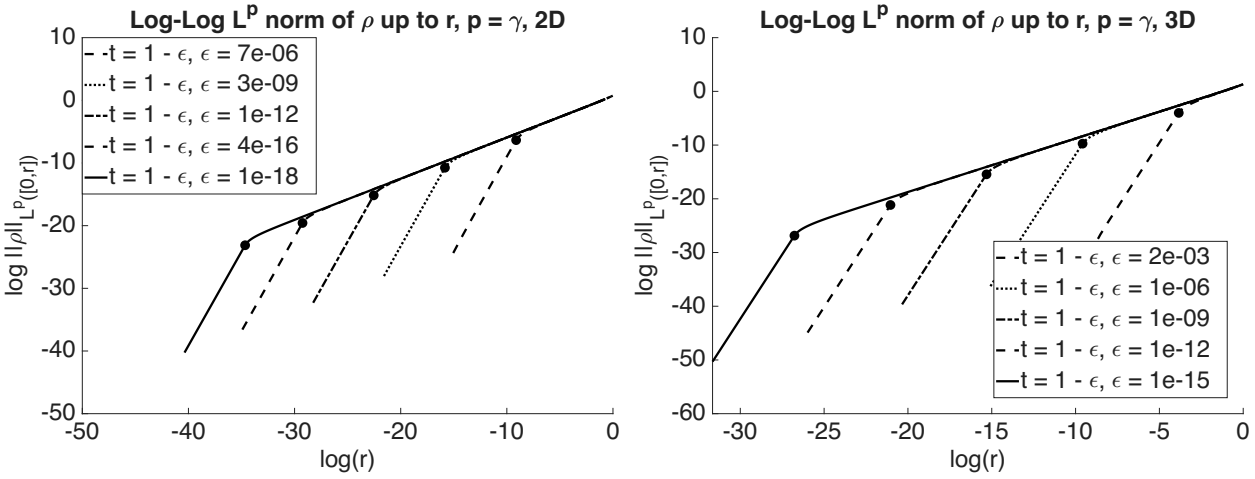


(a) 2D (b) 3D

Figure 4.12: The log-log plot of the $L^p$ norm of $\rho$ on $[0, r]$ in 2D (Subfigure 4.12a) and 3D (Subfigure 4.12b) for $p = \gamma$. Black dots represent $r_l(t)$ at various times.

We conclude by computing the $L^p$ norm of density over $[0, 1]$ for various choices of $p$ to investigate the theoretical work done in Subsection 4.9. The $L^1$ norm, or the mass, is shown in Figure 4.11. From Subfigures 4.11a and 4.11b, we observe no evidence of mass concentration as the mass seems to depend on $r$ as a power law, shown by the adherence of data points to a power law curve with exponent (4.34). This is further supported by the log-log plots of Subfigures 4.11c and 4.11d where the data collapses onto the same line past $r_l(t)$. Moreover, the slope of this line is approximately the exponent predicted in (4.34), displayed in Table 4.4. The black dots in Subfigures 4.11c and 4.11d indicate the location

of $r_l(t)$ for each instance of time. For each data curve, we find the logarithm of the mass collapses to the same line when $r > r_l(t)$. The derivation of (4.34) assumes the power law behavior of $\hat{\rho}(y)$ is valid when $y$ is sufficiently greater than 1 - or equivalently when $r$ is sufficiently greater than $r_l(t)$. On the intermediate region slightly greater than $r_l(t)$, $\hat{\rho}$ is not a power law which explains why the adherence of data to a common line occurs slightly past $r_l(t)$ and not exactly at $r_l(t)$.

Similar behavior is found in Figure 4.12, which shows the log-log plot of the $L^\gamma$ norm over $[0, r]$ for solutions to the cutoff implosion problem in 2D and 3D. We see the same adherence to a common curve as in Subfigures 4.11c and 4.11d, showing no blow up in $L^\gamma$, as implied by the global existence result in [CW22]. The slope of this common line is tabulated in Table 4.4 and matches the predicted value in (4.34).

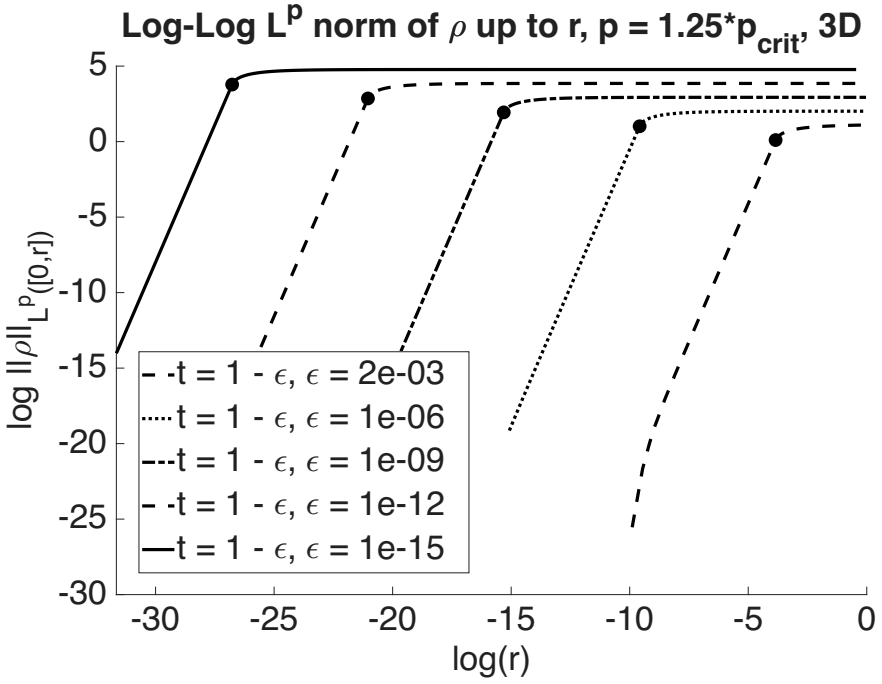


Figure 4.13: Log-log plot of $L^p$ norm of $\rho$ on $[0, r]$ in 3D for $p = 1.25p_{\text{crit}}$, given by (4.30). Black dots represent $r_l(t)$ at various times.

In contrast, an example of $L^p$ blowup is shown in Figure 4.13 where $p$ is set to $1.25p_{\text{crit}}$ and $p_{\text{crit}}$ is given by (4.30) for $n = 2$. The $L^p$ norm behaves drastically different when $p > p_{\text{crit}}$. The $L^p$ norm dramatically increases with time (note Figure 4.13 is in log-log scale) and does

not collapse to any common curve in log-log scale. Figure 4.14 shows an example of how the $L^p$ norm behaves when $p$ is exactly $p_{\text{crit}}$. The $L^p$ norm increases for very small $r$ and then tapers off for larger $r$ instead of collapsing onto a power law curve. As time progresses, the $L^p$ norm also increases at a given $r$, which could imply concentration formation. The growth of the $L^p$ norm in time is less dramatic than the $p = 1.25p_{\text{crit}}$ example however.

In the derivation of (4.30), we found $L^p$ blowup occurs only because of the Kidder solution and non-power law behavior of $\hat{\rho}$ near $r_l(t)$. We see from Subfigures 4.14c and 4.14d most of the growth is on the interval $[0, r_l(t)]$. In contrast, the $L^p$ norm does not grow much for $r$ much greater than $r_l(t)$ - supporting the observation the farfield power law behavior of $\hat{\rho}$ does not contribute to $L^p$ blowup.

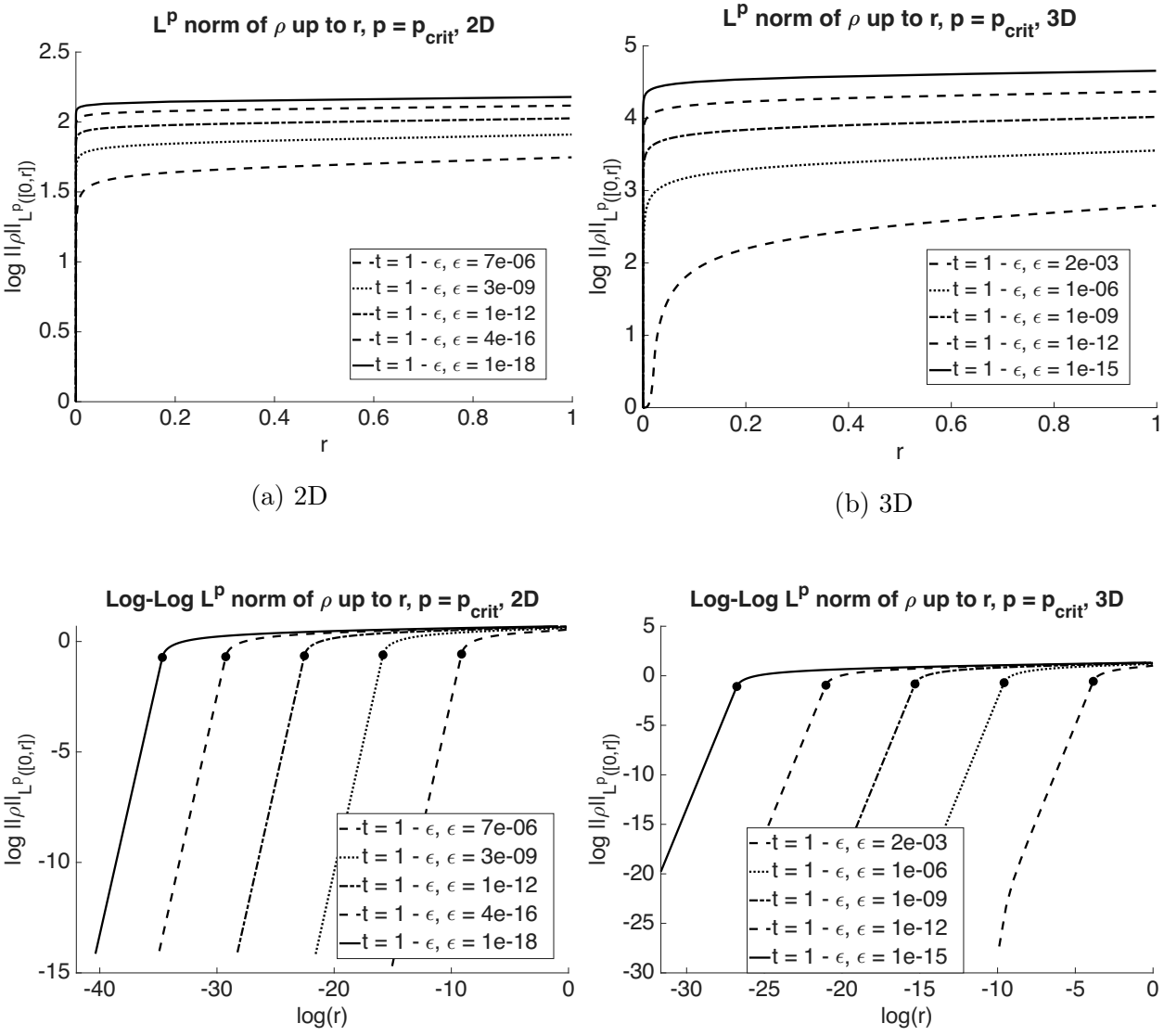


(a) 2D

(b) 3D

(c) Log-Log 2D

(d) Log-Log 3D

Figure 4.14: The $L^p$ norm of $\rho$ on $[0, r]$ in 2D (Subfigure 4.14a) and 3D (Subfigure 4.14b) for $p = p_{\text{crit}}$, given by (4.30). Subfigures 4.14c and 4.14d are in log-log scale. Black dots in subfigures 4.14c and 4.14d represent $r_l(t)$ at various times.

# CHAPTER 5

# Lagrangian Leapfrog and Adaptive Mesh Refinement

In this chapter, we describe the Lagrangian Leapfrog numerical method used to simulate the compressible Euler equations (2.19) and (2.20) in 1D and higher dimensions. Adaptive mesh refinement is used in higher dimensions.

It is critical to choose a suitable numerical scheme for computing finite time singularities at a small scale. We justify using the Lagrangian leapfrog scheme over other methods as this scheme is not diffusive. In general, Eulerian schemes introduce numerical diffusion which can be quantified by modified equation analysis. Numerical diffusion is a major drawback when solving a purely hyperbolic problem since it artificially dampens relative maxima and sharp interfaces. More discussion on the numerical diffusion of Eulerian methods in hydrodynamics can be found in the introduction of [RKG10].

On the other hand, the Lagrangian leapfrog method of [NR50] is dispersive, which means nonphysical oscillations appear in its numerical solution when trying to resolve shocks. Since shocks are not predicted to appear in the solution, we do not expect numerical solutions generated by the Lagrangian leapfrog scheme to suffer from nonphysical oscillations. Thus, we choose the non-diffusive scheme of [NR50] to best preserve the fine details of the solution near implosion time.

To begin, the initial data (4.1) is discretized. Nodes are assigned to the numerical domain of $[0, 2r^*]$ with $N+1$ nodes such that

$$0 = r_1^1 < r_2^1 < \cdots r_{N+1}^1 = 2r^*,$$

where $r_k^n$ is the position of the $k$th node at time $t^n$. The right boundary of the numerical domain is chosen to be $2r^*$ so $r_r(t)$ given in equation (4.5) does not reach the right boundary by $t = 1$. The initial velocity $v_k^{1/2}$ is also defined at each node. Note the velocity is defined on a staggered time grid from the other variables. In between each node lies a cell, in which the density at time $t^n$ between nodes $r_k^n$ and $r_{k+1}^n$ is defined as $\rho_{k+1/2}^n$. To assign the initial data, we associate the spatial point $r_{k+1/2}^n = \frac{r_k^n + r_{k+1}^n}{2}$ to each cell and take $\rho_{k+1/2}^1 = \rho\left(r_{k+1/2}^1, 0\right)$, where $\rho(r, 0)$ is defined in (4.1). After the initial density is assigned, the mass $m_{k+1/2}$ can be assigned to each cell and is set to be constant in time. The mass at each node for $k > 1$ is defined as $m_k = \frac{1}{2}\left(m_{k+1/2} + m_{k-1/2}\right)$. Initial geometric quantities, such as the surface area of spheres with radii prescribed the nodes and the volume of the cells, are computed. The initial time step is defined such that sound cannot cross a cell in a single cycle, which requires

$$\Delta t^n = \chi_C \min_{1 \le k \le N} \frac{r_{k+1}^n - r_k^n}{c_{k+1/2}^n}, \tag{5.1}$$

where $c_k^n$ is the speed of sound (2.5) and $\chi_C = 0.5$ is selected to be the Courant Number.

The Lagrangian leapfrog method begins by advancing the velocity of each node. The update is formed by discretizing the Lagrangian formulation of (2.20),

$$\rho \frac{Dv}{Dt} = -\nabla P, \tag{5.2}$$

where $\frac{D}{Dt} = \frac{d}{dt} + v\frac{d}{dr}$ is the material derivative. The discretization of (5.2) becomes

$$v_k^{n+1/2} = v_k^{n-1/2} - \Delta t^n \frac{A_k^n}{m_k}\left(P_{k+1/2}^n - P_{k-1/2}^n\right),$$

where $A_k^n$ is the surface area of the corresponding dimensional sphere with radius $r_k^n$ and $P_{k+1/2}^n$ is the pressure. In the isentropic case, pressure is related to density via (2.15) and is discretized as $P_{k+1/2}^n = \left(\rho_{k+1/2}^n\right)^\gamma$. Next, each node advects with the new velocity by

$$r_k^{n+1} = r_k^n + \Delta t^n u_k^{n+1/2}.$$

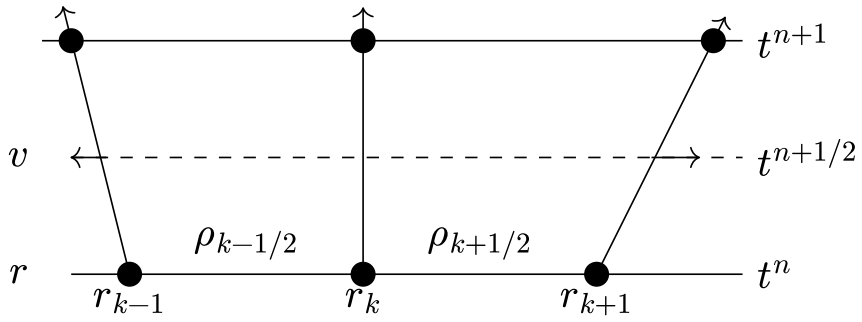


Figure 5.1: The stencil for the Lagrangian leapfrog method. At integer time levels, the position is defined at the nodes (filled circles) while the density is defined on the cells in between the nodes. The velocities are defined on nodes at fractional time levels and are represented as arrows. In Lagrangian numerical methods, the nodes move with the computed velocity.

Geometric quantities are recomputed using the new node positions. To compute the new density, we use the fact that the mass is assumed to be conserved for each cell and define

$$\rho_{k+1/2}^{n+1} = \frac{m_{k+1/2}}{V_{k+1/2}^{n+1}},$$

where $V_{k+1/2}^{n+1}$ is the volume of the annulus bounded by spheres with outer radius $r_{k+1}^{n+1}$ and inner radius $r_k^{n+1}$. Finally, the time step is recalculated by equation (5.1) at time index $n+1$. A stencil describing the location of variables in relation to the nodes and cells is shown in Figure 5.1.

Adaptive mesh refinement first occurs when $\rho(r_l(t), t)$ starts to become a relative maximum. Once this occurs, $r_l$ is identified numerically and saved as $r_l = r_i^{n+1/2}$, where $i = \arg\min_{1 \le k \le N+1} v_k^{n+1/2}$. At every subsequent timestep after the Lagrangian leapfrog steps are finished but before the next time step is computed, $r_l$ is calculated. If the current $r_l$ is a user set fraction of the previously saved $r_l$, then adaptive mesh refinement occurs and the new $r_l$ is saved. When adaptive mesh refinement occurs, all of the cells up to node $i$ are halved such that a new node is placed at the midpoint of every old node, given by

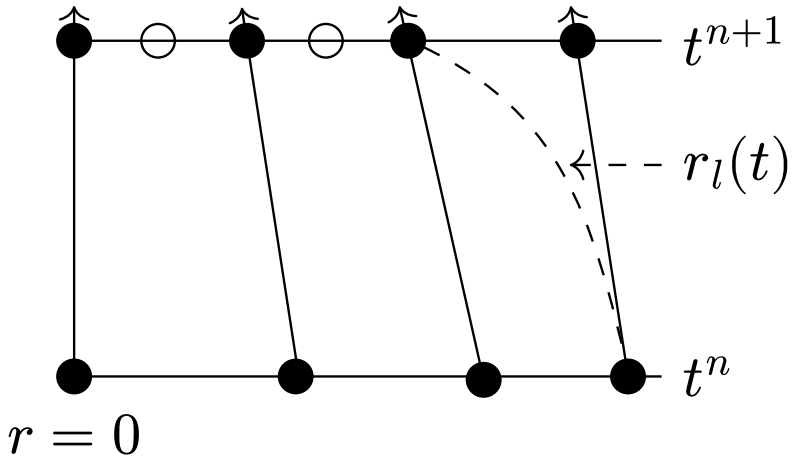


Figure 5.2: A schematic showing how adaptive mesh refinement is performed. Nodes - the filled circles - advect from time $t^n$ to $t^{n+1}$. The dashed line shows the movement of $r_l(t)$. When adaptive mesh refinement occurs, all of the cells in between 0 and $r_l(t)$ are split. A new node - indicated by the unfilled circles - is added as the midpoint of the old nodes.

$r_{2k}^{\text{new}} = \frac{1}{2}(r_k^{\text{old}} + r_{k+1}^{\text{old}})$ where "new" refers to the nodes after mesh refinement and "old" refers to the nodes before mesh refinement. Figure 5.2 shows an example of the mesh refinement process. Data is assigned to all of the new nodes by assuming the Kidder solution (2.39) applies at these nodes. The velocity on the new mesh is defined as

$$v_k^{\text{new}} = v_i^{\text{old}} r_k^{\text{new}}, \tag{5.3}$$

and then density on the new mesh is defined as

$$\rho_{k+1/2}^{\text{new}} = \rho_{i-1/2}^{\text{old}} \left( \frac{r_{k+1/2}^{\text{new}}}{r_{i-1/2}^{\text{old}}} \right)^{n+1}. \tag{5.4}$$

The reassignments in (5.3) and (5.4) are constructed directly from the data without using the time. This is done to avoid any propagation of errors associated with computing the time especially close to implosion time. After the new mesh is defined, the mass is recomputed on the new cells, along with geometric quantities.

# CHAPTER 6

# Uniqueness of the Cutoff Implosion Solution

We discuss uniqueness of the cutoff implosion solutions in this section by appealing to the Weak-Strong Uniqueness results introduced by [Daf79] and [DiP79] and exposited in [Daf16]. In 1D, we can directly apply Weak-Strong Uniqueness to show uniqueness of the cutoff implosion solution by selecting a special entropy and entropy flux pair. For higher dimensions, we cannot do so and instead give a heuristic argument for why the cutoff implosion solution should be the unique solution.

For a system of $m$ conservation laws in $\mathbb{R}^n$

$$\partial_t U + \sum_{\alpha=1}^{n} \partial_\alpha G_\alpha(u(x,t)) = 0, \tag{6.1}$$

where $x \in \mathbb{R}^n$ and $u(x,t) \in \mathbb{R}^m$, the functions $\Phi, \Psi$ are an *entropy* and *entropy flux* pair respectively if they map from $\mathbb{R}^m \to \mathbb{R}$, $\Phi$ is convex, and the pair satisfies the entropy inequality

$$\Phi(u)_t + \nabla \cdot \Psi(u) \leq 0. \tag{6.2}$$

Satisfying the entropy inequality is equivalent to satisfying $D\Psi_\alpha(u) = D\Phi(u)DG_\alpha(u)$ for $\alpha = 1, \cdots, m$. Inequality (6.2) is an equality when $u$ is a sufficiently smooth solution of (6.1).

The entropy inequality (6.2) also restricts which shock solutions are admissible, analogous to the second law of thermodynamics enforcing entropy to be non decreasing. The entropy stemming from hyperbolic conservation law theory is related to thermodynamic entropy as in many physical systems, the entropy of hyperbolic conservation law theory is taken to be the negative of thermodynamic entropy. For the isentropic Euler equations, the most commonly used entropy is the total energy $E = \frac{1}{2}\rho|\vec{v}|^2 + \frac{C}{\gamma-1}\rho^\gamma$ with entropy flux $E\vec{v} + C\rho^\gamma\vec{v}$. Note the total energy is not strictly convex as it loses convexity at vacuum, $\rho = 0$. However, in the specific case of $n = 0$, $\gamma = 3$, we employ the entropy $\Phi(\rho, v) = \frac{1}{2}v^2 + \frac{3}{2}\rho^2$ and corresponding entropy flux $\Psi(\rho, v) = \frac{1}{3}v^3 + 3\rho^2 v$ which is strictly convex everywhere.

Returning to Weak-Strong Uniqueness, the theorem of [Daf79] and [DiP79] is paraphrased as follows from [Daf16]:

**Theorem 6.0.1.** *Assume the system of conservation laws* (6.1) *is endowed with an entropy-entropy flux pair* $(\Phi, \Psi)$ *where* $D^2\Phi(U)$ *is positive definite on* $\mathcal{O}$*. Suppose* $\bar{U}$ *is a classical solution (locally Lipschitz continuous and solves* (6.1)*) of* (6.1) *on* $[0, T)$*, taking values in a convex compact subset* $\mathcal{D}$ *of* $\mathcal{O}$*, with initial data* $\bar{U}_0$*. Then,* $\bar{U}$ *is the unique admissible weak solution on* $[0, T)$ *of* (6.1) *with initial values* $\bar{U}_0$ *and values in* $\mathcal{D}$*.*

In the 1D case, by using the previously described entropy pair $(\Phi, \Psi)$ and given the constructed solution in equations (3.11) and (3.12) is bounded and locally Lipschitz on all of $\mathbb{R}$ for $t \in [0, 1)$, we conclude the constructed rarefaction solution is the unique weak solution on this time interval.

In higher dimensions, equations (2.19) and (2.20) can be written in the form of (6.1):

$$\begin{aligned} \rho_t + \nabla \cdot (\rho\vec{v}) &= 0, \\ (\rho\vec{v})_t + \nabla \cdot (\rho\vec{v} \otimes \vec{v} + C\rho^\gamma I) &= 0. \end{aligned} \tag{6.3}$$

Even if we assume our solution is piecewise differentiable and thus locally Lipschitz, we cannot directly apply the result due to the unboundedness of the solution as $t \to 1$ and the total energy not being strictly convex on the whole domain. In particular, the total energy loses strict convexity at the origin where the density remains zero for all $t < 1$. We

work around this issue by applying the result to a neighborhood around the cutoff point. Specifically, for any fixed time $T < 1$, on the shell $[a, b]$ where $0 < a < r^* < b$, the density is bounded from below by a constant depending on $T$ but strictly greater than zero. This avoids any issues with loss of strict convexity of the associated entropy, and we may directly apply the theorem thereby stating the constructed solution is the unique weak solution up to $T < 1$ on $[a, b]$. While this discussion is not a rigorous treatment of uniqueness, it does suggest our constructed solution to the cutoff implosion problem in higher dimensions is the unique solution stemming from the cutoff implosion initial data.

# CHAPTER 7

# Conclusion

In this thesis, we studied implosions to the isentropic, compressible Euler equations with radial symmetry. Our cutoff implosion initial data is formed by continuously cutting off the Kidder solution constructed in Chapter 2.5. The qualiative behavior of the cutoff implosion solution differs dramatically based on dimension. Chapter 3 studies the 1D case where the implosion is suprssed by a rarefaction growing from the cutoff position. A complete analytical solution can be found in 1D up until the time when the rarefaction arrives at the origin. On the other hand, Chapter 4 shows for any dimension higher than 1 the "rarefaction" emerging does not supress the implosion. A region of influence argument is applied to show this and we also show the implosion approaches a self-similar limit close to implosion time. The theoretical predictions of Chapters 3 and 4 are supported by numerical simulations done by the Lagrangian leapfrog numerical scheme. Adaptive mesh refinement is used for higher dimension simulations to provide high resolution into the blowup regime. Chapter 5 describes the numerical implementation of Lagrangian leapfrog and adaptive mesh refinement. Uniqueness of the cutoff implosion solutions is addressed in Chapter 6, rigorously for 1D and heuristically for higher dimensions.

In 1D, we discover that the effect of the cutoff leads to a growing rarefaction wave that emerges from the cutoff position and eventually dominates the imploding part of the solution. This is an interesting phenomenon on its own. The rarefaction similarity variable arising

in the cutoff implosion solution is nonstandard. Our rarefaction variable also encodes the original implosion time within itself. In the derivation of the rarefaction, this arises as a byproduct of taking the left state to be the time varying Kidder solution. The emergence of the unusual rarefaction variable in a fairly simple problem is interesting and warrants further exploration. We began the investigation by hypothesizing whether the finite speed of propagation of the cutoff will reach the origin and disturb the Kidder solution. However, regardless of where the cutoff is positioned, the Kidder solution vanishes.

In higher dimensions, implosion still occurs and we showed the bifurcation between implosion and non-implosion of the cutoff implosion solution is sharp in dimension. The bifurcation indicates a feature inherit in the geometry of higher dimensions causes the implosion. Although non-integer dimension is physically uninterpretable, the radially symmetric, compressible Euler equations formally admits non-integer $n$ in (2.19). The sharp difference in behavior from 1D to any higher dimension indicates the cause may be focusing at the origin in higher dimensions. We comment we see no restrictions on how large $n$ can be from our analysis. Exploratory numerical investigation shows the predictions made in this paper holds for non-integer $n$ and large $n$. It may be interesting to consider the ramifications of this work in the limit as $n$ approaches infinity.

The motivation behind continuously cutting off the Kidder initial data is to determine whether it is necessary to have unbounded density in the farfield and still maintain implosion. In the Kidder solution, all Lagrangian particles arrive at the origin at implosion time regardless of their initial position. These farfield behaviors render the Kidder solution difficult to directly apply for physical implementation. The analysis done in higher dimensions shows the farfield can be replaced with a much milder farfield condition of constant density. This reveals the mechanics of the Kidder implosion does not rely on an infinite stream of fluid to the origin from the whole domain and can be achieved with a finite amount of fluid on a finite region.

We show close to implosion time the solution asymptotically approaches a self-similar profile. We emphasize these numerically found solutions which are asymptotic limits to the cutoff implosion solution are *exact* self-similar solutions for $y \geq 1$. To complete the

description of the self-similar profiles, one must understand the profiles for $0 \leq y \leq 1$, corresponding to radial coordinates near $r = 0$. Recall in [SWW25] the authors construct smooth self-similar solutions for a sequence of blowup exponents $s_n \to s^*$, where $s^*$ is exactly the blowup exponent considered in this work. A complete description of the self-similar profile could provide insight since it may act as the limiting profile to the sequence of smooth self-similar solutions of [SWW25]. Additionally, one may use the full self-similar profile as initial data for hydrodynamic simulations.

Numerical simulations support the predictions made in this work. The fact the cutoff implosion solution and its landmark features can be accurately computed in both 1D and higher dimensions may make it a candidate to be a numerical test problem. Aditionally, the fact the cutoff implosion problem can be numerically computed promising indicator of the numerical stability of the cutoff implosion solution. In contrast, the solution of [MRR22a] is numerically unstable as shown by [Bia21]. One of the marked differences between the cutoff implosion solution and the implosions of [BCG25, JT20, MRR22a] is the implosion point in the cutoff implosion solution is non-stationary. A heuristic explanation given in terms of potential flow in Chapter 2 argues why stationary implosions may struggle with instability. Given the cutoff implosion solution seems to enjoy numerical stability properties, searching for imploding solutions where the implosion occurs at a traveling point may be a fruitful strategy.

One example of further numerical investigation is to generalize the cutoff imploding solution to arbitrary $\gamma$. A generalized version of the Kidder solution for arbitrary $\gamma$ and $n$ can be found in [Ram11]. However, their functional forms are given by the inverse of the incomplete beta function. We predict many of the arguments relying on derivations involving explicit forms done in this work may not be possible, encouraging the use of numerical simulation for exploration.

After the left characteristic wave emerging from the cutoff reaches the origin, it is natural to ask whether it is possible to continue the solution. For 1D, this takes the form of a double shock structure. For the higher dimension case, this corresponds physically to an *explosion* and works such as [Gud42] and [CCS26] consider such explosions originating from implosions.

The explosion solutions have shocks emerging from the origin. Mathematically, the result of [CW22] guarantees the global existence of weak solutions to the cutoff implosion initial data. Studying the explosion that emerges from the implosion considered in this work could give greater insight into the physical interpretation of the solution.

Another direction is to consider smoother cutoffs, after it has been established the Kidder implosion does not require unbounded initial data in the far field. The solution presented in this work is a weak solution in the sense it is not continuously differentiable. A smoother way of connecting the Kidder solution to a constant or bounded density in the far field could possibly incur implosion as well. We give explicit constructions of differentiably connected initial data in the $n = 1$ case. Consider the "reflected parabola" initial data

$$\rho(r,0) = \begin{cases} \frac{1}{4}r^2 & \text{if } 0 \le r \le 2 \\ -\frac{1}{4}(r-4)^2 + 2 & \text{if } 2 \le r \le 4 \\ 2 & \text{if } 4 \le r \end{cases} \tag{7.1}$$

or the "hyperbolic tangent" initial data

$$\rho(r,0) = \begin{cases} \frac{1}{4}r^2 & \text{if } 0 \le r \le 2 \\ \tanh(r-2) + 1 & \text{if } 2 \le r \end{cases} \tag{7.2}$$

starting from rest. Both examples are $C^1$ but not $C^2$. The reflected parabola initial data connects to a constant for $r \ge 4$, while the hyperbolic tangent initial data is instead bounded. Numerical simulations using these initial densities are displayed in Figure 7.1, giving numerical evidence for possible implosions using the smoother initial conditions.

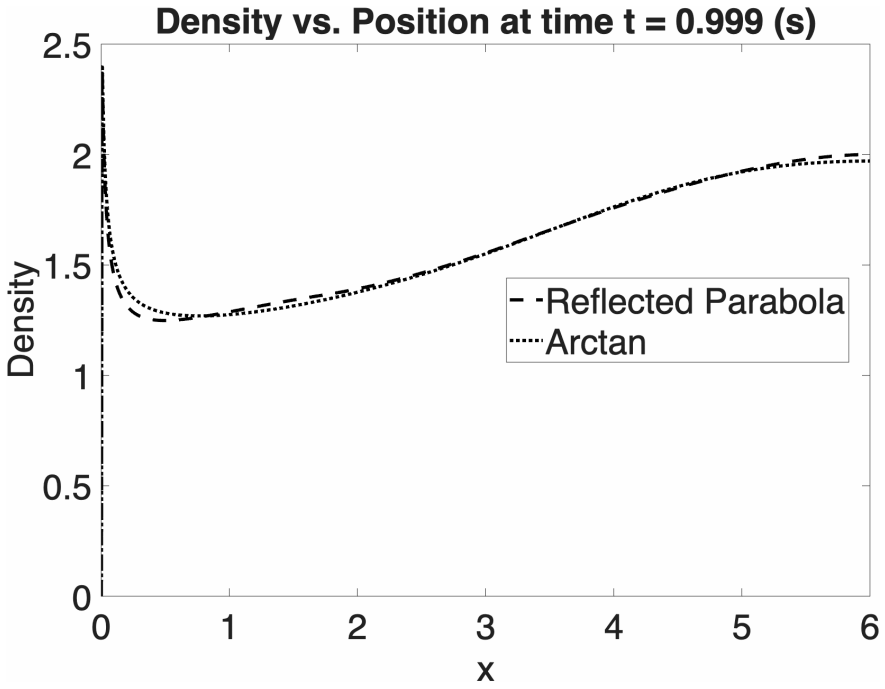


Figure 7.1: Numerical simulations of Isentropic Euler using the initial density (7.1) (dashed) and (7.2) (dotted) suggest possible implosion as $t$ approaches 1.

# APPENDIX A

# Equivalence of Self Similar Systems

In this appendix, we show the non-autonomous system (4.20) is the same as the non-autonomous system instantiated in [Gud42] and elaborated in [MRR22a] by comparing system (4.20) to the notation and derivation presented in [Bia21].

First, rescale system (4.20) by dividing the top equation by $A^{n+2}$ and the bottom equation by $A^2$ where $A$ is defined in (4.17). We also rescale $\hat{\rho}$ and $\hat{v}$ by setting $\hat{\rho} = \frac{\hat{\rho}}{A^{n+1}}$ and $\hat{v} = -\frac{\hat{v}}{A}$ (the negative rescaling is to match the definition of the self-similar ansatz for velocity in [MRR22a]). In doing so, the initial conditions for $\hat{\rho}$ and $\hat{v}$ in (4.15) no longer depend on $r^*$. After the rescaling, system (4.20) becomes

$$\begin{aligned} \frac{\lambda}{A}\hat{\rho} + y\hat{\rho}' + (\hat{\rho}\hat{v})' + \frac{n\hat{\rho}\hat{v}}{y} = 0, \\ \frac{\beta\lambda}{A}\hat{v} + y\hat{v}' + \hat{v}\hat{v}' + \gamma\hat{\rho}^{\gamma-2}\hat{\rho}' = 0. \end{aligned} \tag{A.1}$$

Note we have defined pressure with constant $C = 1$ while $C = \frac{\gamma-1}{\gamma}$ in [MRR22a].

Let $s^*$ denote the inverse of the $(1-t)$ exponent in $r_l(t)$, so

$$s^* = \frac{2}{1 + (n+1)^{-1/2}}. \tag{A.2}$$

The exponent $s^*$ is denoted as $r$ in [MRR22a] and [Bia21]. Note the value of (A.2) is the upper bound of the blowup exponents in [MRR22a] and [SWW25]. Recall $\beta = \frac{1}{n+1}$ which is equal to $\frac{1}{\ell} = \frac{\gamma-1}{2}$. The final step to show equivalence between the systems is to show the

coefficients $\frac{\lambda}{A}$ and $\frac{\beta\lambda}{A}$ in front of $\hat{\rho}$ in the top equation and $\hat{v}$ in the bottom equation of (A.1) are $\ell(s^*-1)$ and $s^*-1$ respectively. Recalling the value of $\frac{\lambda}{A}$ from (4.27), we compute $s^*-1$ and see

$$s^*-1=-\frac{1-\sqrt{n+1}}{1+\sqrt{n+1}}$$

confirming $\frac{\lambda}{A}=\ell(s^*-1)$ and $\frac{\beta\lambda}{A}=s^*-1$. Thus, we have established the equivalence of the non-autonomous systems and presented here and in the literature. The autonomous systems are subsequently equivalent by applying the same Emden transform to both.

# References


[AV04] Stefano Atzeni and Jürgen Meyer-ter Vehn. "Inertial confinement by spherical implosion." In *The Physics of Inertial Fusion: Beam Plasma Interaction, Hydrodynamics, Hot Dense Matter*, pp. 47–74. Oxford University Press, 2004.

[BCG25] Tristan Buckmaster, Gonzalo Cao-Labora, and Javier Gómez-Serrano. "Smooth imploding solutions for 3D compressible fluids." *Forum of Mathematics, Pi*, **13**:e6, 2025.

[BDS22] Tristan Buckmaster, Theodore D. Drivas, Steve Shkoller, and Vlad Vicol. "Simultaneous Development of Shocks and Cusps for 2D Euler with Azimuthal Symmetry from Smooth Data." *Annals of PDE*, **8**(2):26, November 2022.

[BF84] Matania Ben-Artzi and Joseph Falcovitz. "A second-order Godunov-type scheme for compressible fluid dynamics." *Journal of Computational Physics*, **55**(1):1–32, 1984.

[BHL02] Michael P. Brenner, Sascha Hilgenfeldt, and Detlef Lohse. "Single-bubble sonoluminescence." *Reviews of Modern Physics*, **74**(2):425–484, 2002.

[Bia21] Anxo Biasi. "Self-similar solutions to the compressible Euler equations and their instabilities." *Communications in Nonlinear Science and Numerical Simulation*, **103**:106014, 2021.

[BLR89] A. Bourgeade, Ph. Le Floch, and P. A. Raviart. "An asymptotic expansion for the solution of the generalized Riemann problem. Part 2 : application to the equations of gas dynamics." *Annales de l'Institut Henri Poincaré C, Analyse non linéaire*, **6**(6):437–480, 1989.

[BRB17] Z M Boyd, S D Ramsey, and R S Baty. "On the Existence of Self-Similar Converging Shocks in Non-Ideal Materials." *The Quarterly Journal of Mechanics and Applied Mathematics*, **70**(4):401–417, 2017.

[BSV22] Tristan Buckmaster, Steve Shkoller, and Vlad Vicol. "Formation of Shocks for 2D Isentropic Compressible Euler." *Communications on Pure and Applied Mathematics*, **75**(9):2069–2120, 2022.

[CCS24] Jiajie Chen, Giorgio Cialdea, Steve Shkoller, and Vlad Vicol. "Vorticity blowup in 2D compressible Euler equations." *arXiv preprint arXiv:2407.06455*, 2024.

[CCS26] Jiajie Chen, Giorgio Cialdea, Steve Shkoller, and Vlad Vicol. "A new class of Euler explosions." preprint, arXiv:2606.18152, 2026.

[CGS25] Gonzalo Cao-Labora, Javier Gómez-Serrano, Jia Shi, and Gigliola Staffilani. "Non-radial implosion for compressible Euler and Navier-Stokes in $\mathbb{T}^3$ and $\mathbb{R}^3$." *Cambridge Journal of Mathematics*, **13**(4):753–885, 2025.

[Che25] Jiajie Chen. "Vorticity Blowup in Compressible Euler Equations in $\mathbb{R}^d, d \geq 3$." *Annals of PDE*, **11**(2):21, 2025.

[CM14] Demetrios Christodoulou and Shuang Miao. *Compressible flow and Euler's equations*. Surveys of Modern Mathematics. International Press of Boston; Beijing, Somerville, Massachusetts, 2014.

[CPZ17] Geng Chen, Ronghua Pan, and Shengguo Zhu. "Singularity Formation for the Compressible Euler Equations." *SIAM Journal on Mathematical Analysis*, **49**(4):2591–2614, 2017.

[Cro37] L. Crocco. "Eine neue Stromfunktion für die Erforschung der Bewegung der Gase mit Rotation." *ZAMM - Journal of Applied Mathematics and Mechanics / Zeitschrift für Angewandte Mathematik und Mechanik*, **17**(1):1–7, 1937.

[CSV25] Giorgio Cialdea, Steve Shkoller, and Vlad Vicol. "Classical Euler flows generate the strong Guderley imploding shock wave." *arXiv preprint arXiv:2510.19688*, 2025.

[CSV26] Jiajie Chen, Steve Shkoller, and Vlad Vicol. "Smooth and stable Euler implosions." preprint, arXiv:2605.00808, 2026.

[CW22] Gui-Qiang G. Chen and Yong Wang. "Global Solutions of the Compressible Euler Equations with Large Initial Data of Spherical Symmetry and Positive Far-Field Density." *Archive for Rational Mechanics and Analysis*, **243**(3):1699–1771, 2022.

[Daf79] C. M. Dafermos. "The second law of thermodynamics and stability." *Archive for Rational Mechanics and Analysis*, **70**(2):167–179, 1979.

[Daf16] Constantine M. Dafermos. *Hyperbolic conservation laws in continuum physics*. Grundlehren der mathematischen Wissenschaften. Springer, Berlin, Germany, 4th edition, 2016.

[DiP79] Ronald DiPerna. "Uniqueness of Solutions to Hyperbolic Conservation Laws." *Indiana Univ. Math. J.*, **28**(1):137–188, 1979.

[Eva22] Lawrence C. Evans. *Partial differential equations*. Graduate Studies in Mathematics. American Mathematical Society, Providence, Rhode Island, second edition, 2022.

[GRB20] Jesse F. Giron, Scott D. Ramsey, and Roy S. Baty. "Nemchinov–Dyson solutions of the two-dimensional axisymmetric inviscid compressible flow equations." *Physics of Fluids*, **32**(12):127116, 2020.

[Gud42] K.G. Guderley. "Starke kugelige und zylindrische Verdichtungsstösse in der Nähe des Kugelmittelpunktes bzw. der Zylinderachse." *Luftfahrtforschung*, **19**:302–312, 1942.

[Hor69] Heinrich Hora. "Some Results of the Self-Similarity Model." In *Proceedings of the First Workshop, held at Rensselaer Polytechnic Institute, Hartford Graduate Center, East Windsor Hill, Connecticut, June 9–13, 1969*, Laser Interaction and Related Plasma Phenomena, pp. 365–382. Springer US, 1969.

[Hun60] C. Hunter. "On the collapse of an empty cavity in water." *Journal of Fluid Mechanics*, **8**(2):241–263, 1960.

[Hun69] James H. Hunter, Jr. "The Collapse of Interstellar Gas Clouds and the Formation of Stars." *Monthly Notices of the Royal Astronomical Society*, **142**(4):473–498, 1969.

[Jen26] Helge Kristian Jenssen. "Cumulative Euler flows." preprint, arXiv:2604.22073, 2026.

[JLS25] Juhi Jang, Jiaqi Liu, and Matthew Schrecker. "On Self-Similar Converging Shock Waves." *Archive for Rational Mechanics and Analysis*, **249**(3):24, 2025.

[JT20] Helge Kristian Jenssen and Charis Tsikkou. "Amplitude Blowup in Radial Isentropic Euler Flow." *SIAM Journal on Applied Mathematics*, **80**(6):2472–2495, 2020. doi: 10.1137/20M1340241.

[Kid74] R. E. Kidder. "Theory of homogeneous isentropic compression and its application to laser fusion." *Nuclear Fusion*, **14**(1):53, 1974.

[Kid76] R. E. Kidder. "Energy gain of laser-compressed pellets: a simple model calculation." *Nuclear Fusion*, **16**(3):405, 1976.

[Lax64] Peter D. Lax. "Development of Singularities of Solutions of Nonlinear Hyperbolic Partial Differential Equations." *Journal of Mathematical Physics*, **5**(5):611–613, 1964.

[Lax73] Peter D. Lax. *Hyperbolic Systems of Conservation Laws and the Mathematical Theory of Shock Waves*. CBMS-NSF Regional Conference Series in Applied Mathematics. Society for Industrial and Applied Mathematics, 1973.

[Leb92] Marie-Pierre Lebaud. *Description de la formation d'un choc dans le p-systeme. Approximation de valeurs propres par des elements finis isoparametriques*. Thesis, Université de Rennes I, 1992. Thèse de doctorat Mathématiques et applications Rennes 1 1992 1992REN10094.

[Lev90] Randall Leveque. *Numerical Methods for Conservation Laws*. Springer Basel AG, Basel, 1990.

[Li94] Ta-tsien Li. "The Generalized Riemann Problem for Quasilinear Hyperbolic Systems of Conservation Laws." In Chaohao Gu, Xiaxi Ding, and Chung-Chun Yang, editors, *Partial Differential Equations in China*, pp. 80–103. Springer Netherlands, Dordrecht, 1994.

[LR88] Ph Le Floch and P. A. Raviart. "An asymptotic expansion for the solution of the generalized Riemann problem Part I: General theory." *Annales de l'Institut Henri Poincaré C, Analyse non linéaire*, **5**(2):179–207, 1988.

[LRB27] Jack Luong, Scott D. Ramsey, Andrea L. Bertozzi, and Roy Baty. "Self-similar imploding solutions of the 1D compressible Euler equations with a far field cutoff." *Discrete and Continuous Dynamical Systems*, **58**(0):197–221, 2027.

[LT91] Philippe Le Floch and Li Tatsien. "A global asymptotic expansion for the solution to the generalized Riemann problem." *Asymptotic Analysis*, **3**(4):321–340, 1991.

[LW06] Tianhong Li and Dehua Wang. "Blowup phenomena of solutions to the Euler equations for compressible fluid flow." *Journal of Differential Equations*, **221**(1):91–101, 2006.

[MRR22a] Frank Merle, Pierre Raphaël, Igor Rodnianski, and Jeremie Szeftel. "On the implosion of a compressible fluid I: Smooth self-similar inviscid profiles." *Annals of Mathematics*, **196**(2):567–778, 2022.

[MRR22b] Frank Merle, Pierre Raphaël, Igor Rodnianski, and Jeremie Szeftel. "On the implosion of a compressible fluid II: Singularity formation." *Annals of Mathematics*, **196**(2):779–889, 2022.

[Noh87] W. F. Noh. "Errors for calculations of strong shocks using an artificial viscosity and an artificial heat flux." *Journal of Computational Physics*, **72**(1):78–120, 1987.

[NR50] J. von Neumann and R. D. Richtmyer. "A Method for the Numerical Calculation of Hydrodynamic Shocks." *Journal of Applied Physics*, **21**(3):232–237, 1950.

[Ram11] Scott D. Ramsey. "The linear velocity profile class of hydrodynamics verification test problems." Full Paper LA-UR-11-02766, Los Alamos National Laboratory, 2011.

[RKG10] Brant E. Robertson, Andrey V. Kravtsov, Nickolay Y. Gnedin, Tom Abel, and Douglas H. Rudd. "Computational Eulerian hydrodynamics and Galilean invariance." *Monthly Notices of the Royal Astronomical Society*, **401**(4):2463–2476, 02 2010.

[Sed59] L. I. Sedov. "Chapter IV - One-Dimensional Unsteady Motion of a Gas." In L. I. Sedov, editor, *Similarity and Dimensional Methods in Mechanics*, pp. 146–304. Academic Press, 1959.

[Sid85] Thomas C. Sideris. "Formation of singularities in three-dimensional compressible fluids." *Communications in Mathematical Physics*, **101**(4):475–485, 1985.

[Suz13] Takashi Suzuki. "Irrotational Blowup of the Solution to Compressible Euler Equation." *Journal of Mathematical Fluid Mechanics*, **15**(3):617–633, September 2013.

[SWW25] Feng Shao, Dongyi Wei, Shumao Wang, and Zhifei Zhang. "Blow-up of the 3-D compressible Navier-Stokes equations for monatomic gases." preprint, arXiv:2501.15701, 2025.

[Tor09] Eleuterio F. Toro. "The Generalized Riemann Problem." In *Riemann Solvers and Numerical Methods for Fluid Dynamics: A Practical Introduction*, pp. 625–653. Springer Berlin Heidelberg, Berlin, Heidelberg, 2009.

[VS82] J. Meyer-ter Vehn and C. Schalk. "Selfsimilar Spherical Compression Waves in Gas Dynamics." *Zeitschrift für Naturforschung A*, **37**(8):954–970, 1982.

[Woo76] P. R. Woodward. "Shock-driven implosion of interstellar gas clouds and star formation." *The Astrophysical Journal*, **207**:484, 1976.

[Yin04] Huicheng Yin. "Formation and construction of a shock wave for 3-D compressible Euler equations with the spherical initial data." *Nagoya Mathematical Journal*, **175**:125–164, 2004.

[Yue17] Manwai Yuen. "Blowup for irrotational $C^1$ solutions of the compressible Euler equations in $R^N$." *Nonlinear Analysis*, pp. 132–141, July 2017.